

## ABSTRACT

ZADROZNY, LEAH. Macromolecular Microstructure and Lipid Deposition in Healthy and Diseased Thoracic Aortas in a Mouse Model of Atherosclerosis. (Under the direction of John M. Cullen).

Atherosclerosis is a disease in which plaques form within the vessel wall resulting in hardening of the arteries accounting for more than half of the annual mortality in the United States. These plaques consist of fatty substances, cholesterol, cellular waste products, calcium and fibrin. They form within the tunics intima and media of large and medium sized elastic and muscular arteries. Several risk factors have been associated with disease initiation and progression, including hypertension, hypercholesterolemia and cigarette smoking. The pathogenesis is a complex process considered to be multifactorial. Much research has been completed regarding late stage disease; however, little has been done regarding the three-dimensional (3D) macromolecular structural characteristics of early stage disease development. This is considered to be the time frame prior to formation of the fatty streak presently regarded to be the earliest visibly detectable lesion.

In this dissertation, I have characterized lipid deposition and its association with elastin and collagen in both developing and young adult thoracic aortas of SR-BI KO/ApoER61<sup>h/h</sup> mice, a recently described mouse model of diet inducible atherosclerosis. First, I addressed the currently utilized mouse vascular preparations and then developed a novel, *in situ* preparation of the thoracic aorta that more closely mimics several key physiological properties. Second, I evaluated the 3D macromolecular structural development and lipid deposition of this *in situ* preparation of the SR-BI KO/ApoER61<sup>h/h</sup> mouse thoracic aorta from birth to 60 days old in preparation for modeling atherosclerosis. Finally, I examined early lesion development in SR-BI KO/ApoER61<sup>h/h</sup> mouse through modifying this *in situ* preparation in order to visualize the thoracic intercostal arterial ostia

(ICAO) within the descending thoracic aorta. *In situ* imaging was completed using nonlinear optical microscopy (NLOM) on a multimodal platform including two-photon excitation fluorescence (TPEF), second harmonic generation (SHG), Sum frequency generation (SFG), and Coherent anti-Stokes Raman scattering (CARS).

Through evaluation of the current techniques in vascular preparation for microscopic analysis, my research has provided a novel, reproducible, *in situ* dissection of the mouse thoracic aorta. When coupled with NLOM, this preparation has provided valuable insight in healthy arterial morphology in the developing mouse aorta indicative of the extracellular matrix status that can further be applied to diseased arteries. Modification of this *in situ* preparation provided additional insight regarding atherosclerotic lesion initiation and progression within, surrounding, and downstream of the thoracic intercostal arterial ostia.

© Copyright 2015 Leah Zadrozny

All Rights Reserved

Macromolecular Microstructure and Lipid Deposition in Healthy and Diseased  
Thoracic Aortas in a Mouse Model of Atherosclerosis

by  
Leah Zadrozny

A dissertation submitted to the Graduate Faculty  
of North Carolina State University  
in partial fulfillment of the  
requirements for the degree of  
Doctor of Philosophy

Comparative Biomedical  
Sciences

Raleigh, North Carolina

2015

APPROVED BY:

---

Dr. John Cullen  
Committee Chair

---

Dr. Robert Balaban

---

Dr. Mark Simpson

---

Dr. Edward Neufeld

**DEDICATION**

I dedicate this dissertation to myself, my fabulous pup Phoebe, and all of my friends and family that gave me the support to never give up.

## BIOGRAPHY

Leah Zadrozny was born in the heart of Hartford, Connecticut and relocated to Wilbraham, Massachusetts, the home of Friendly's, during her teen years. A convoluted path commencing at graduation from Minnechaug Regional Highschool included a brief stay at the University of Connecticut, followed by a summer in Martha's Vineyard and then several years in the snowy green mountains of Vermont until she returned to the University of Vermont to complete her undergraduate studies in animal science. As luck may have it, Leah ended up in one of the best veterinary schools in the US, at North Carolina State University where she not only enjoyed working with the critters on the teaching farm, but also the critters at the local sports bar that contributed to her college fund. And as if that wasn't enough, from veterinary school, she continued on her relentless educational path of pursuing a pathology residency combined with a Ph.D. through the Graduate Scholars in Molecular Pathology Program at the National Heart Lung and Blood Institute in Bethesda, Maryland. Here she has happily remained, under the direction of Dr. Robert Balaban and Dr. R. Mark Simpson, to complete her studies in vascular pathology while becoming intimately associated with the SR-BI KO/ApoER61<sup>h/h</sup> atherogenic mouse model, the clunky microdissection scope, and the magical multiphoton microscope.

## ACKNOWLEDGMENTS

I would like to sincerely thank my entire committee for your time, support and efforts throughout the course of my Ph.D. Thank you to Dr. Mark Simpson for your professional and emotional support. You have been extremely supportive in offering your assistance in every aspect during my stay at the NIH. To Dr. Robert Balaban, I thank you for your guidance, support, and insights into shaping the overall design of my research. To Dr. Ed Neufeld, I thank you for taking me on as a mentee and introducing me into the Laboratory of Cardiac Energetics as well as offering advice throughout my time at NHLBI. And to Dr. John Cullen, thank you for being a friend as well as my major professor throughout this entire process. Your support has been nothing short of amazing.

## TABLE OF CONTENTS

<b>LIST OF VCDNGU'</b> .....	vii
<b>LIST OF HK WTGU</b> .....	viii
<b>LIST OF ABBREVIATIONS AND ACRONYMS</b> .....	xiv
<b>CHAPTER 1: Introduction, Background and Specific Aims</b> .....	1
Atherosclerosis and the key players within the vascular extracellular matrix .....	2
Animal models of atherosclerosis .....	5
Hypothesis and specific aims .....	9
Development of the <i>in situ</i> mouse thoracic aorta preparation .....	10
References .....	17
<b>CHAPTER 2: Study of the Development of the Mouse Thoracic Aorta Three-Dimensional Macromolecular Structure Using Two-photon Microscopy</b> .....	21
Abstract .....	22
Introduction .....	22
Material and Methods.....	23
Results .....	25
Discussion .....	33
References .....	34
<b>CHAPTER 3: Early Three-dimensional Atherosclerotic Lesion Development in Scavenger Receptor Class B Type I-Deficient, Hypomorphic Apolipoprotein ER61 Mice and the Association with Endothelial and Smooth Muscle Cell Damage</b> .....	40
Abstract .....	41
Introduction .....	42

Material and Methods.....	45
Results .....	48
Discussion .....	51
References .....	63
CHAPTER 4: Discussion and Conclusions.....	67
References .....	73

**LIST OF TABLES**

**Table 1:** Average proximal thoracic aortic wall thickness in SR-BI KO/ApoER61<sup>h/h</sup> transgenic mice fed normal chow

**Table 2:** Average distance between undulating peaks in the internal elastic lamina in SR-BI KO/ApoER61<sup>h/h</sup> transgenic mice fed normal chow

## LIST OF FIGURES

### Chapter 1

**Figure 1.1:** Multiphoton *ex vivo* images (*en face*) acquired from the thoracic aorta with bilateral intercostal ostia from 2, 5 day-old C57BL/6T mice fed NC. Images depict 1 $\mu$ m slices captured from variably thick z-series within the tunica media. Colocalized SHG (collagen)/TPEF (elastin) signals are acquired by 2 separate detection channels of the microscope where SHG and TPEF are represented in green and red respectively. (A) White arrows represent collagen enhancement artifact produced by incomplete transection of the intercostal arteries. (B-1) Similar artifact depicted towards the luminal surface, and adventitial surface (B-2). (Images obtained with a Leica, 20x0.7 NA immersion objective lens).

**Figure 1.2:** *Ex vivo* (A) and *in situ* (B-1, B-2) multiphoton images acquired from the thoracic aorta of 5 day-old C57BL/6T (A) and SR-BI<sup>-/-</sup>/ApoE61<sup>h/h</sup> (B) mice fed NC. (A) White arrows represent bilateral intercostal ostia. (B-2) Full-thickness cross section of the proximal thoracic aorta. Black arrow indicates the direction of laser penetration from the ventral to dorsal aortic surface. Note how the dorsally located intercostal ostia are not captured microscopically. (Images in A and B obtained with Leica, 20x0.7 NA and 20x1.0 NA immersion objective lenses respectively).

**Figure 1.3:** *In situ* (A) and *ex vivo* (B) multiphoton images acquired from a proximal intercostal ostia of 2, 2 month-old SR-BI<sup>-/-</sup>/ApoE61<sup>h/h</sup> mice fed NC. Black arrows indicate the direction of laser penetration from the luminal to adventitial surface (A) Note the oval shaped, ostial distortion created by cutting a window through the ventral aortic surface to image the dorsal aortic surface with associated intercostal ostia. (B) Note the increased undulating effect the *ex vivo* aortic preparation has on the vessel wall. (Images obtained with a Leica, 20x1.0 NA immersion objective lens).

### Chapter 2:

**Figure 2.1:** *In situ* dissection of the mouse thoracic aorta in dorsal recumbency. The heart (H), kidneys (K), and three regions of interest—the proximal (PTA), mid (MTA) and distal (DTA) thoracic aorta—are labeled. Multiphoton images are all depicted with the head and tail ends of the mice at the top and bottom of each image, respectively. Full-thickness z-stacks were obtained from the luminal to the adventitial surfaces of the ventral thoracic aorta. Scale, 1 mm.

**Figure 2.2:** Multiphoton images from the proximal, mid and distal thoracic aorta (PTA, MTA and DTA) of 1 day old (do), 30do and 60do SR-BI<sup>-/-</sup>/ApoE61<sup>h/h</sup> mice. Images depict 1- $\mu$ m-thick optical slices captured from full-thickness z-stacks within the tunica media. Sections are representative of the thoracic aortic regions of interest, as shown in the *in situ* mouse preparation in Figure 1, with

the head and tail ends of the mice at the top and bottom of each image, respectively. Collagen (green), elastin (red) and lipid (blue) signals are merged after post-image processing by Independent Component Analysis (ICA). Scale, 50  $\mu\text{m}$ .

**Figure 2.3:** Multiphoton, in situ images acquired from the proximal ventral (anterior) thoracic aortas (VTAs) of representative SR-BI<sup>-/-</sup>/ApoE61<sup>h/h</sup> mice aged 1–60 days old (do). Images depict 1- $\mu\text{m}$ -thick optical slices captured from full-thickness z-stacks within the tunica media of the proximal VTA. For each individual orthogonal panel, the center, top and right sections depict en-face (xy), cross/transverse (xz) and sagittal (yz) sections, respectively. Collagen second harmonic generation (SHG) is green, elastin auto-fluorescence is red and Nile Red (NR) lipid droplet fluorescence is blue. Independent component analysis (ICA) was applied to all z-stacks for post-image processing to eliminate signal overlap and background noise. For raw images, and full thickness movies, please refer to the Supplemental Materials section. L, lumen; TA, tunica adventitia. Scale, 50  $\mu\text{m}$ .

**Figure 2.3 video1:** AVI video clips were produced from a full-thickness z-stack (ranging from ~150–200- $\mu\text{m}$ -thick tissue image acquisitions) obtained within the ventral (anterior) surface of the proximal thoracic aorta of a representative SR-BI<sup>-/-</sup>/ApoE61<sup>h/h</sup> mouse aged 60 days old (do). En-face projections coupled with cross sections are provided. Collagen second harmonic generation (SHG) is green, elastin auto-fluorescence is red and Nile Red (NR) lipid droplet fluorescence is blue. Image acquisition was optimized during all experiments to fill the digitizer. ICA was applied during post-image processing and the elastin fluorescence signal was optimized across all age groups for comparison purposes. Additional movies are provided in the Supplemental Materials.

**Figure 2.4 video2:** An AVI video clip produced from a maximum projection, three-dimensional (3D) rendering from a z-stack of the proximal ventral (anterior) thoracic aorta (VTA) of a representative SR-BI<sup>-/-</sup>/ApoE61<sup>h/h</sup> mouse aged 60 days old (do) is provided. For color scheme and post-image processing information, see Fig3video1. Additional 3D renderings are provided in the Supplemental Materials.

**Figure 2.4:** Three-dimensional, multiphoton, maximum projection renderings (approximate size 512×512×150-200  $\mu\text{m}$ ) from z-stacks of the proximal ventral (anterior) thoracic aortas (VTAs) SR-BI<sup>-/-</sup>/ApoE61<sup>h/h</sup> mice aged 1, 30 and 60 days old (do). Collagen second harmonic generation (SHG) is green, elastin auto-fluorescence is red and Nile Red (NR) lipid droplet fluorescence is blue. Independent component analysis (ICA) was applied to all z-stacks for post-image processing. For a more detailed view, please refer to the movies in the Supplemental Materials. Scale bar, 50  $\mu\text{m}$ .

**Figure 2.5:** Bar graphs showing the average thoracic aortic wall thickness. (A) Average

ventral (anterior) thoracic aortic (VTA) full thickness (FT) (total bar height) significantly increased with age ( $*p < 0.05$  for mice aged 20 days old (do), 30do and 60do when compared to 1do mice) with no significant change in 10do mice as compared with 20do mice. Values are mean  $\pm$  SEM. (B) Ratios of the wall thickness of the tunica adventitia and tunica media to full VTA thickness. The greatest significance is exhibited when 1do mice are compared to 10do mice ( $p = 0.032$ ), and minimal significance when 1do mice are compared to 30do mice ( $p = 0.048$ ) and 10do mice are compared to 20do mice ( $p = 0.047$ ). This indicates that the thickness of the individual tunics within the thoracic aorta increases proportionally with age.

**Figure 2.6:** Histological features of representative proximal thoracic aortas (PTAs) from SR-BI<sup>-/-</sup>/ApoE61h/h mice aged 1–60 days old (do). PTAs were stained with picosirius red (B, E, H, K, and N) for collagen (red fibrils), and Movat's pentachrome (C, F, I, L and O) for collagen (yellow), elastin (black/red), and glycosaminoglycans (green/blue), for which minimal staining is appreciated. Note the frequent undulation present at 1do (A–C), which dissipates by 10do and is absent in mice aged 20do and older. An intercostal ostium (K, black arrow) with collagenous ridges protruding into the luminal surface can be appreciated within the TA. All images are oriented with luminal surfaces at the top and external adventitial surfaces at the bottom of the photomicrographs. Scale, 20  $\mu$ m.

**Figure 2.7:** Transverse, osmicated electron micrographs showing the deposition of lipid within the distal thoracic aortic wall of SR-BI<sup>-/-</sup>/ApoE61<sup>h/h</sup> mice aged 1-60 days old (do). Variably sized, intracellular lipid can be observed within endothelial cells (C, E, G-I) and within smooth muscle cells (B, C, H-I) directly beneath the internal elastic lamina (IEL) across all age groups, (yellow asterisks). At 1do, lipid is being engulfed by endothelial cells (A, red asterisks). Within an intercostal ostial ridge, lipid droplets are pictured accumulating within a smooth muscle cell (F, yellow arrow). At 60do, an accumulation of intraendothelial, clustered and variably sized lipid droplets admixed with calcified/mineralized debris (black amorphous material) is indicative of early atherosclerotic lesion formation (J). Scale, 500 nm (A–E and G–J) and 2  $\mu$ m (F).

Supplemental image 1: Depicted is the same image panel represented in Figure 3 prior to post image analysis by ICA used for comparison. Note the background signal present in the lipid channel is greater before ICA processing resulting in less signal to noise in unprocessed images. L = lumen; TA = tunica adventitia. Scale bar, 50 $\mu$ m. 279x361mm (300 x 300 DPI)

Supplemental image 2: Distribution of proteoglycans decorin (A, C, E, G, and I) and biglycan (B, D, F, H, and J) within the extracellular matrix of proximal thoracic aortas (PTAs) from SR-BI<sup>-/-</sup>/ApoE61<sup>h/h</sup> mice aged 1-60do. Notice the prominent positive immunoreactivity (brown chromogen) in the tunica adventitia (TA) and subendothelium (E) for both decorin and biglycan across all age groups. Decorin staining within the tunica media (TM) appears to decrease with age while

remaining similar for biglycan. Intercostal anterior ostia (black arrows, C and G-J) exhibit strong immunoreactivity for both decorin and biglycan within the subendothelium. All images are oriented with luminal surfaces at the top and external adventitial surfaces

### Chapter 3

**Figure 3.1:** Multimodal nonlinear optical microscopy three-dimensional (3D) *in situ* images from the thoracic aorta with bilateral intercostal ostia from a 2 month old C57BL/6T control mouse fed NC. Elastin (green), collagen (blue), permeabilized (damaged) Sytox blue positive cells (cyan) and lipid (red) signals are merged after post-image processing. The dim red background signal exhibited above the luminal surface (white asterisk) and within the intercostal ostia (white asterisk) should be discerned from the bright red, punctate to clustered lipid droplets as observed in Figures 2-8. (A) *En face* image. Note the presence of damaged cells circumferentially surrounding the ostia (white arrows) in the absence of lipid deposition. (B) Representative cross section with minimal positive Sytox blue staining transmurally. (Images were obtained with a Leica 25x1.0 NA water immersion objective lens.

**Figure 3.2:** Multimodal nonlinear optical microscopy three-dimensional (3D) *in situ* images from the thoracic aorta with bilateral intercostal ostia from a 2 month old SR-BI KO/ApoER61<sup>h/h</sup> control mouse fed NC (day 0). Elastin (green), collagen (blue), permeabilized (damaged) Sytox blue positive cells (cyan) and lipid (red) signals are merged after post-image processing. (A) *En face* image. Note the extensive cluster of damaged spindleoid cells indicative of smooth muscle cell morphology downstream to the left intercostal ostium in the absence of lipid deposition. Similar to the C57BL/6T control mouse in Figure 1, Sytox blue positive cells surround the left intercostal ostium (plump endothelial cells, white arrow) but with the addition of lipid droplets on the ostial ridge. Moderate numbers of individualized lipid droplets are also appreciated multifocally on the luminal surface (A, black arrows) (B) Representative cross section showing transmurally damaged smooth muscle cells and endothelial cells between and within intercostal ostia respectively. (Images were obtained with a Leica 25x1.0 NA water immersion objective lens.

**Figure 3.3:** Multimodal nonlinear optical microscopy three-dimensional (3D) *in situ* images from the thoracic aorta with bilateral intercostal ostia from a 2 month old SR-BI KO/ApoER61<sup>h/h</sup> mouse fed HFHC for 1 day. Elastin (green), collagen (blue), permeabilized (damaged) Sytox blue positive cells (cyan) and lipid (red) signals are merged after post-image processing. (A) *En face* image. Bilateral intercostal ostia exhibit extensive, extra- and intracellular (foam cells, white arrow) circumferential lipid deposition colocalized with Sytox blue positive. Downstream, transmurally Sytox blue positive spindleoid cells (smooth muscle cells) are also present. (B and C) Representative cross sections of the left and right intercostal ostia respectively showing mural

lipid deposition colocalized with Sytox blue positive cells. (Images were obtained with a Leica 25x1.0 NA water immersion objective lens.

**Figure 3.4:** Multimodal nonlinear optical microscopy three-dimensional (3D) *in situ* images from the thoracic aorta with bilateral intercostal ostia from a 2 month old SR-BI KO/ApoER61<sup>h/h</sup> mouse fed HFHC for 3 days. Elastin (green), collagen (blue), permeabilized (damaged) Sytox blue positive cells (cyan) and lipid (red) signals are merged after post-image processing. (A) *En face* image appears similar to mice fed HFHC for 3 days (Figure 3) less the cluster of positive Sytox blue smooth muscle cells distal to and between this pair of intercostal ostia. (B and C) Representative cross sections of the left and right intercostal ostia respectively showing mural lipid deposition colocalized with Sytox blue positive cells. (Images were obtained with a Leica 25x1.0 NA water immersion objective lens.

**Figure 3.5:** Multimodal nonlinear optical microscopy three-dimensional (3D) *in situ* images from the thoracic aorta with the left intercostal ostium from a 2 month old SR-BI KO/ApoER61<sup>h/h</sup> mouse fed HFHC for 5 days. Elastin (green), collagen (blue), permeabilized (damaged) Sytox blue positive cells (cyan) and lipid (red) signals are merged after post-image processing. (A) *En face* image, and (B and C) cross sections exhibiting lipid and damaged cells surrounding the left intercostal ostium with an extensive cluster of transmurally damaged smooth muscle cells (C) downstream of the ostium. (Images were obtained with a Leica 25x1.0 NA water immersion objective lens.

**Figure 3.6:** Multimodal nonlinear optical microscopy three-dimensional (3D) *in situ* images from the thoracic aorta with the right intercostal ostium from a 2.5 month old SR-BI KO/ApoER61<sup>h/h</sup> mouse fed HFHC for 14 days. Elastin (green), collagen (blue), permeabilized (damaged) Sytox blue positive cells (cyan) and lipid (red) signals are merged after post-image processing. (A) *En face* image with increased lipid and foam cell deposition within and surrounding the intercostal osritum with the similarly located downstream cluster of damaged smooth muscle cells and increased damaged endothelial cells surrounding the ostium. (B) Representative cross section with an extensive cluster of transmurally damaged smooth muscle cells (C) downstream of the ostium. (Images were obtained with a Leica 25x1.0 NA water immersion objective lens.

**Figure 3.7:** Multimodal nonlinear optical microscopy three-dimensional (3D) *in situ* images from the thoracic aorta with the left intercostal ostium from a 3 month old SR-BI KO/ApoER61<sup>h/h</sup> mouse fed HFHC for 21 days. Elastin (green), collagen (blue), permeabilized (damaged) Sytox blue positive cells (cyan) and lipid (red) signals are merged after post-image processing. (A) *En face* image with increased lipid and foam cell deposition on and surrounding the left intercostal osritum with the downstream cluster of damaged smooth muscle cells now colocalized with foam cell (white arrow) accumulation on the

endothelium. (B) Representative cross section with an extensive cluster of transmurally damaged smooth muscle cells. (Images were obtained with a Leica 25x1.0 NA water immersion objective lens.

**Figure 3.8:** Additional high resolution, three-dimensional (3D) *in situ* images from the thoracic aorta with the left (A and C) and right (B and D) intercostal ostia from a 3 month old SR-BI KO/ApoER61<sup>h/h</sup> mouse fed HFHC for 21 days. Elastin (green), collagen (blue), permeabilized (damaged) Sytox blue positive cells (cyan) and lipid (red) signals are merged after post-image processing. (A) Note the lipid beginning to form a plaque that variably occludes the ostial opening (white arrow). (Images were obtained with a Leica 25x1.0 NA water immersion objective lens.

**LIST OF ABBREVIATIONS AND ACRONYMS**

2D: Two-dimensional

3D: Three-dimensional

ApoE: ApoLipoproteinE

CAD: Coronary artery disease

CARS: Coherent anti-Stokes Raman scattering

CHD: Coronary heart disease

CSPG: Chondroitin sulfate proteoglycan

DTA: Distal thoracic aorta

dKO: Double knock out

DSPG: Dermatan sulfate proteoglycan

EC: Endothelial cell

ECM: Extracellular matrix

FH: Familial hyperlipidemia

Fs: Femtosecond

GAG: Glycosaminoglycan

HDL: High-density lipoprotein

HFHC: High-fat, high-cholesterol

HSPG: Heparin sulfate proteoglycan

HyD: Hybrid detector

ICA: Independent component analysis

ICAM-1: Intracellular adhesion molecule-1

ICAO: Intercostal arterial ostia

IEL: Internal elastic lamina

IHC: Immunohistochemistry

KSPG: Keratin sulfate proteoglycan

LDL: Low-density lipoprotein

LDLR: Low-density lipoprotein receptor

LP: Lipoprotein

MRI: Magnetic resonance imaging

MTA: Mid-thoracic aorta

NA: Numerical aperture

NC: Normal chow

NHLBI: National Heart Lung and Blood Institute

NIH: National Institutes of Health

NLOM: Nonlinear optical microscopy

NR: Nile red

PBS: Phosphate buffered saline

PMT: Photomultiplier tube

PTA: Proximal thoracic aorta

PTC: Plasma total cholesterol

PG: Proteoglycan

SFG: Sum frequency generation

SHG: Second harmonic generation

SMC: Smooth muscle cell

SR-B1: Scavenger receptor-B1

SR-BI KO/ApoER61<sup>h/h</sup>: Scavenger receptor class B Type I-deficient, hypomorphic apolipoprotein ER61 mice

TA: Thoracic aorta

TEM: Transmission electron microscopy

TPEF: Two-photon excitation fluorescence

WT: Wild type

VCAM-1: Vascular cell adhesion molecule

VTA: Ventral thoracic aorta

CHAPTER 1

Introduction, Background and Specific Aims

## Atherosclerosis and the key players within the vascular extracellular matrix

Atherosclerosis is a disease of the arterial wall of large elastic arteries (e.g., the aorta, carotid and subclavian arteries), and the large and medium sized muscular arteries (e.g., coronary arteries and the main distributing branches extending from the aorta). This arteriopathy has been implicated in 75% of cardiovascular disease-related deaths in the United States (Roger VL et al., 2011). Vascular lesions can be initiated as early as *in utero* as regions of intimal thickenings and intracellular lipid accumulation often referred to as fatty streaks. The most pronounced thickenings develop in regions near branch vessel ostia, at the aortic and carotid bifurcations, and within the descending aorta (Thubrickar and Robicsek, 1995). Advanced disease is characterized by the conversion of fatty streaks into atheromas or atherosclerotic plaques resulting in vascular remodeling, acute and chronic luminal obstruction, plaque rupture, thrombosis, and diminished oxygen supply to major organs (Rosenfeld et al., 1993). Spontaneous regression of early lesions often occurs. However, intermediate and advanced stages experienced later in life are considered both progressive and multifactorial dependent upon several associated risk factors including genetic predisposition, age, hypertension, dyslipidemia, diabetes, cigarette smoking and obesity (Mitchell et al., 2010, McVeigh et al., 1997, Heagerty et al., 1993, Lehmann et al., 1992).

Although mechanical factors such as pressure-induced vascular wall stress and blood flow disturbances are important in lesion development, the extracellular matrix

(ECM), including collagen, elastin and proteoglycans (PGs) within the arterial wall, largely contribute to the pathologic vascular remodeling observed with atherosclerosis (Ross, 1993). Collagen comprises a substantial component of the total protein found in fibrous plaques and advanced lesions. An intact internal elastic lamina (IEL) composed of condensed, amorphous bundles of elastin fibers serves as a barrier to macromolecules including LDL. However, elastin has high amino acid content, thus an increased affinity for nonpolar molecules such as lipid. Any disruption in this barrier can therefore contribute to the accumulation of lipid within the vessel wall (Camejo 1982). Furthermore, subendothelial low-density lipoprotein (LDL) retention by PGs is currently thought to serve as an initiating step in atherosclerosis (Nakashima et al., 2007, Tabas et al., 2007, Boren et al., 1998, Williams and Tabas, 1995).

PGs are macromolecules composed of a mucopolysaccharide protein core covalently linked to variable numbers of negatively charged, linear repeating disaccharide sugar side chains referred to as glycosaminoglycans (GAGs). GAG side chains can be classified according to the type of hexosamine, hexose or hexuronic acid unit they contain as well as their glycosidic linkage to serine residues within the protein core (Wight, 1998). It is the negatively charged sulfates and carboxylates on the GAG side chains that form electrostatic bonds to the positively charged basic amino acids, lysine and arginine on LDL (Flood et al., 2004).

The four main families of GAGs bound to PGs consist of chondroitin sulfate (CSPGs), dermatan sulfate (DSPGs), heparin sulfate (HSPGs) and keratan sulfate (KSPGs). Of these, DS-, CS- and HSPGs are variably distributed throughout the vascular

wall and are considered to be atherogenic due to their ability to entrap lipoproteins (Williams, 2001). Moreover, decorin, biglycan and versican are considered the major CSPGs and DSPGs of the arterial wall (Williams, 2001), all of which have been identified as enriched PGs in human atherosclerotic lesions through biochemical and immunohistochemical analysis (Merrilees et al., 2001, O'Brien et al., 1998). Of these three PGs, both decorin and biglycan are considered to be members of the small leucine-rich repeat (SLRP) PG family whose role in the pathogenesis of both native and graft vessel atherosclerosis has been increasingly recognized (Yamakawa et al., 2000). In addition to lipid retention, PGs promote intimal expansion and induce the growth and accumulation of smooth muscle cells (SMC) further contributing to the early stages of disease (Merrilees et al., 2001). Previous *in vitro* analysis provides evidence that decorin links LDL with collagen type I suggesting a potential role for decorin-mediated subintimal LDL retention and progression of atherosclerotic disease (Pentikainen et al., 1997). Through the utilization of a series of microtiter well binding assays involving LDL, decorin and collagen type I, this group was able to show that the ability of LDL to bind to collagen-coated wells in the absence of decorin was negligible. However, collagen-coated wells incubated with decorin resulted in LDL binding to decorin-collagen complexes at a level that was considered 10-fold higher than binding to collagen alone.

Localization of early lesion development in atherosclerosis strongly correlates with additional factors including low wall shear stress (WSS), oscillatory shear stress, and flow separation all of which are exhibited at major branch points within the aortic tree (Taylor et al., 1998; Neufeld et al., 2010; Albert et al., 2014). High endothelial cell (EC) turnover, proliferation and death have been described in these regions as well (Lin et al., 1990; Suo

et al., 2007; Jongstra-Bilen et al., 2010) resulting in increased production of inflammatory cytokines and adhesion molecules further perturbing the endothelium. Taken together, these hemodynamic disturbances and EC changes contribute to a leaky endothelium allowing for increased macromolecular transport of modified lipids through the vessel wall.

Herein, I propose to qualitatively and quantitatively describe the complex interactions that occur within the ECM of the developing vascular bed commencing at birth with regard to elastin, collagen, lipid and PGs in SR-BI KO/ApoER61<sup>h/h</sup> transgenic mice fed normal chow (NC). This base will provide valuable information in explaining the complex vascular remodeling of the ECM in early lesion development that occurs in the same model when fed a high-fat, high-cholesterol (HFHC) diet. Furthermore, it will contribute to the determination of the appropriate therapeutic intervention to prevent fatty streak development and potentially ameliorate advanced disease progression. multiphoton analysis of the vascular bed may allow for a more targeted approach in the prevention of early lipid retention in the vessel wall.

#### Animal models of atherosclerosis

The use of animal models of atherosclerosis has provided relevant information regarding factors contributing to disease initiation, progression and regression that has been extrapolated to human disease. Well-established animal models of atherosclerosis have been described in mice, rabbits, rats, dogs, pigs and nonhuman primates with guinea pig, hamster, and cat models being used less frequently (Vilahur et al. review, 2011). Lesion development in these models can occur either spontaneously or through dietary, mechanical, chemical or immunological interventions (Drew, 2000). Small versus large

animal models are typically more extensively utilized due to the low cost, ready availability and small size limiting the amount of novel pharmacological agent required for therapeutic intervention.

There are numerous transgenic, gene-targeted and genetically manipulated mouse models of atherosclerosis that often differ markedly in response to proposed experimental designs (Daugherty, 2002) warranting critical importance in choosing the most appropriate model. However, they are all based on perturbations of lipoprotein metabolism. Wild-type (WT) mice are fairly resistant to developing disease as they exhibit high levels of antiatherogenic high-density lipoprotein (HDL) and low levels of proatherogenic very low-density lipoprotein (VLDL) (Zadelaar et al., 2007). Presently, the more commonly utilized models include the apolipoprotein E knockout (ApoE<sup>-/-</sup>), the low-density lipoprotein receptor knockout (LDLR<sup>-/-</sup>) (deLuna, 2008, Zadelaar et al., 2007), and models that have alterations in scavenger receptor (SR) genes (Moore and Freeman, 2006).

ApoE is synthesized in the liver, brain and several other peripheral tissues and cells including macrophages. This protein has many roles that are considered atheroprotective including inhibition of smooth muscle cell (SMC) and EC proliferation, mediation of hepatic uptake of plasma remnant lipoproteins (LPs), stimulation of cholesterol efflux from lipid-laden macrophages (foam cells) in atherosclerotic lesions and regulation of associated immune and inflammatory responses (Greenow et al., 2005). ApoE<sup>-/-</sup> mice fed NC are hypercholesterolemic (Nakashima et al., 1994, Reddick et al., 1994) with a plasma total cholesterol (PTC) level of approximately 500 mg/dl (normal mouse reference range is 80-100 mg/dl). These mice typically live past 1 year of age despite spontaneous atherosclerotic lesion development between 3 and 4 months

of age (Rosenfeld et al., 2000, Plump et al., 1992, Zhang et al., 1992). Lesion development can be greatly accelerated when fed an atherogenic, HFHC diet increasing PTC to levels greater than 2000 mg/dl (Nakashima et al., 1994).

The LDLR is considered the primary pathway for the uptake and intracellular degradation of circulating cholesterol (Lagor and Millar, 2010) and it binds to LPs that contain apoE and apoB in LDL (Krul et al., 1985). LDLR gene expression is regulated by intracellular sterol content, and is limited mainly to the liver. Inherited defects in the LDLR pathway can result in familial hypercholesterolemia (FH), characterized by increased serum LDL and increased risk of coronary heart disease (CHD) (Vance and Vance, 2002). LDLR deficient mice are used as a model of FH. This model typically requires an atherogenic diet to promote atherosclerosis (Ishibashi et al., 1994), which elevates the baseline PTC in mice fed NC from approximately 300 mg/dl up to 1500 mg/dl (Potteaux et al., 2007). The development of the apoE<sup>-/-</sup> and LDLR<sup>-/-</sup> models has provided important insight on two of the most significant events exhibited in human atherosclerosis; spontaneous plaque rupture and intra-lesional hemorrhage (Bennett, 2002). Even though mouse models have proven to be valuable in understanding the pathophysiology of atherosclerosis, they are sometimes limited by temporal constraints and the ability of the model to produce lesions similar to those described in humans.

The mouse model utilized in my dissertation work is the recently defined double transgenic model of atherosclerosis, the scavenger receptor class B, type I (SR-BI) deficient, hypomorphic apolipoprotein ER61 mouse (SR-BI KO/ApoER61<sup>h/h</sup>) (Zhang et al., 2005). SR-BI is expressed in many tissues and cells including hepatocytes, macrophages and steroidogenic tissue. It regulates cholesterol homeostasis in both

hepatocytes and macrophages. This receptor is important in reverse cholesterol transport, a multi-step process involving HDL mediated transport of cholesterol from peripheral tissues to the liver where it is secreted into the bile and excreted through the intestinal tract (Rigotti et al., 1997). SR-BI<sup>-/-</sup> mice exhibit markedly decreased biliary cholesterol excretion and are hypercholesterolemic even when fed a low-fat diet, but do not develop apparent spontaneous atherosclerosis (Trigatti et al., 1999).

Hypomorphic apoE mice express decreased levels of apoE mRNA, at approximately 2-5% of normal apoE levels in plasma exhibiting a nearly normal lipoprotein profile when fed NC, but are highly susceptible to diet-induced hypercholesterolemia (Raffai and Weisgraber, 2002). Furthermore, hypomorphic apoER61 mice express a mutant form of murine apoE, Thr61→Ar61, that has structural and lipoprotein binding characteristics similar to those of the human apoE4 isoform (Raffai et al., 2001). Combined deficiencies of SR-BI, apoE and/or hypomorphic apoE result in the previously described lipoprotein perturbations (increased VLDL), large and irregularly shaped HDL particles, and dramatically accelerated, sometimes diet-induced, atherosclerosis with clinical signs exhibited as early as 4 weeks of age (Trigatti et al., 1999, Braun et al., 2003).

The SR-BI KO/ApoER61<sup>h/h</sup> mouse is a model of diet-induced occlusive coronary atherosclerosis and CHD demonstrating many features of human CHD similar to those induced in SR-BI/apoE double KO (dKO) mice including occlusive coronary atherosclerosis, myocardial infarction, cardiac dysfunction, and premature death (Zhang et al., 2005, Trigatti et al., 2004, Braun et al., 2003). However, the true power of SR-BI KO/ApoER61<sup>h/h</sup>, as previously stated, lies in the idea that despite low levels of plasma

atherosclerosis and CHD demonstrating many features of human CHD similar to those induced in SR-BI/apoE double KO (dKO) mice including occlusive coronary atherosclerosis, myocardial infarction, cardiac dysfunction, and premature death (Zhang et al., 2005, Trigatti et al., 2004, Braun et al., 2003). Whereas the SR- BI/apoE dKO mice fed NC alone will exhibit severe disease between 4 to 8 weeks of age (Braun et al., 2003). Transitioning SR-BI KO/ApoER61<sup>h/h</sup> mice to an atherogenic diet, regardless of their age, has been shown to result in death within approximately 1 month (Zhang et al., 2005). Having the ability to control the onset, duration, and severity of disease classifies this powerful model as a useful tool for investigating the initiation, progression and (therapeutic) regression of atherosclerosis.

#### Hypothesis and specific aims

The overall hypothesis is that subendothelial retention and accumulation of atherogenic apoB-containing LDL within the arterial wall contributes to the initiation of atherosclerosis resulting in disruption of the vessel wall extracellular matrix, elevated production of LDL-binding proteoglycans (PG), and potentiation of occlusive vascular disease. In support of this hypothesis, the goals of the current work were three fold. First, to develop a mechanistic approach in preparing the thoracic aorta of SR-BI KO/ApoER61<sup>h/h</sup> mice, a detailed comparison of microdissection and imaging techniques was undertaken defining a novel *in situ* model which best captures aortic architecture as described in live animals. This was an integral step in undertaking the main body of this dissertation. Second, to provide a base for evaluating early atherosclerotic lesion initiation and progression, longitudinal analysis of the macromolecular microstructure of the developing thoracic aorta, with regard to elastin, collagen, lipid and proteoglycan

distribution was examined utilizing multiphoton and light microscopy and transmission electron microscopy (TEM) in SR-BI KO/ApoER61<sup>h/h</sup> mice fed a NC diet. And third, to qualitatively and quantitatively analyze the complex interactions of the thoracic aortic ECM, with emphasis on the thoracic ICAO, in the early stages of atherosclerotic lesion development and continued disease progression in SR-BI KO/ApoER61<sup>h/h</sup> mice fed a HFHC diet utilizing multiphoton microscopy.

#### Development of the *in situ* mouse thoracic aorta preparation

In an effort to determine the best aortic dissection and to move forward with the body of this dissertation, several different techniques in variably aged, C57BL/6T mice and SR-BI KO/ApoER61<sup>h/h</sup> mice were completed for *ex vivo* and *in situ* imaging.

*Aortic dissections for multiphoton microscopy:* For *ex vivo* preparations, mouse aortas were isolated, adventitial collagen was sharply dissected, and the vessels were removed from the animals by transecting at the level of the aortic root, ileac bifurcation and to within 1 mm of all arteries originating from the aorta. Aortas were incised longitudinally or left patent, mounted on a glass slide with phosphate buffered saline (PBS), covered with a glass cover slip and secured on all edges with surgical tape. Figure 1.1 shows aortic examples from 5 day-old mice that were incised longitudinally depicting bilateral intercostal ostia.

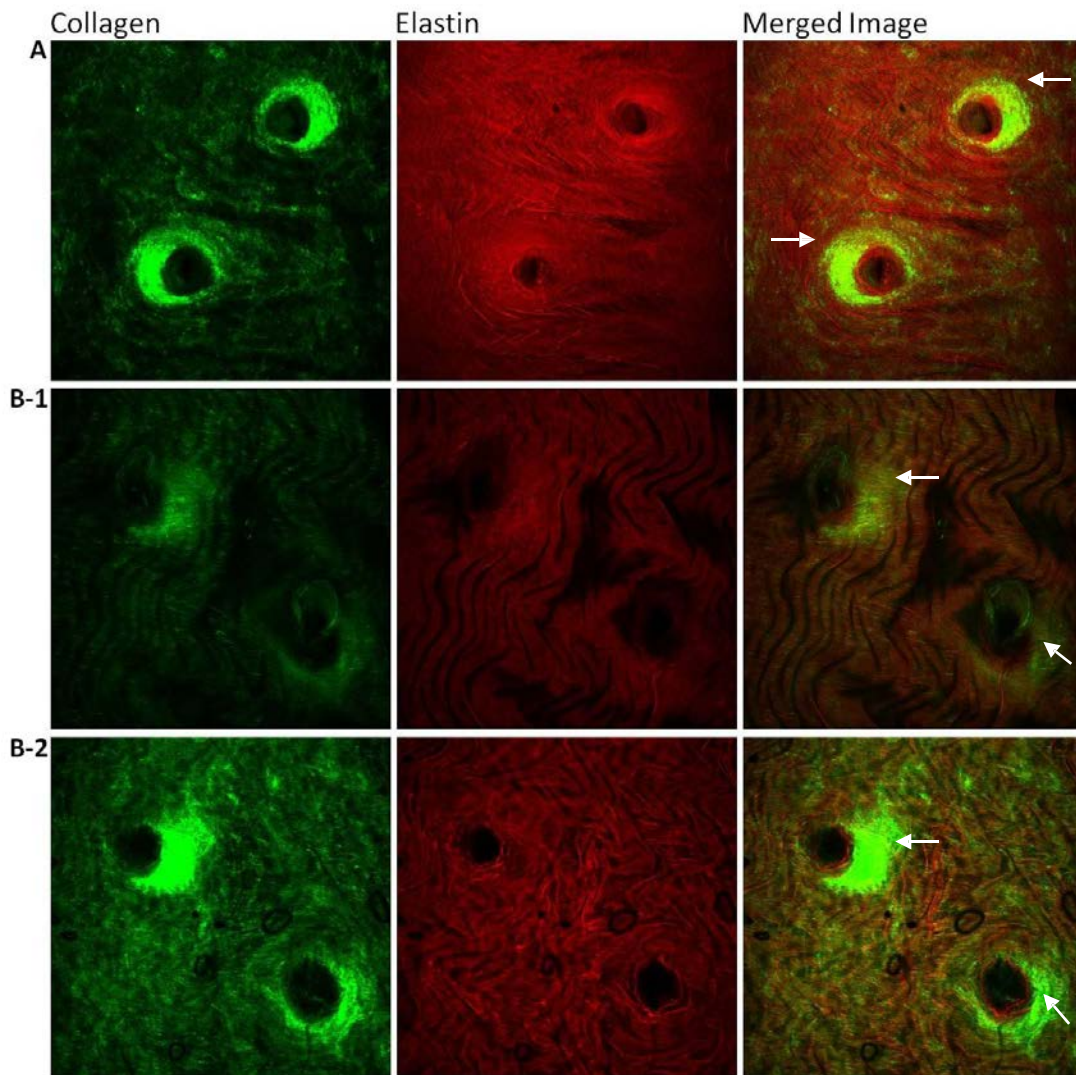


**Figure 1.1:** Multiphoton *ex vivo* images (*en face*) acquired from the thoracic aorta with bilateral intercostal ostia from 2, 5 day-old C57BL/6T mice fed NC. Images depict 1 $\mu$ m slices captured from variably thick *z*-series within the tunica media. Colocalized SHG (collagen)/TPEF (elastin) signals are acquired by 2 separate detection channels of the microscope where SHG and TPEF are represented in green and red respectively. (A) White arrows represent collagen enhancement artifact produced by incomplete transection of the intercostal arteries. (B-1) Similar artifact depicted towards the luminal surface, and adventitial surface (B-2). (Images obtained with a Leica, 20x0.7 NA immersion objective lens).

The laser is directed at the luminal surface first. The main issue with this approach concerns how closely the intercostal arteries are transected from their origin. Depending on how the aortas are mounted on the slides, remnant intercostal arteries can be forced to the side or even through the ostia resulting in what appears to be falsely accumulating, peri-ostial collagen. This could potentially be troublesome especially when quantitating collagen during vascular development and atherosclerotic disease in determining if this effect is real versus artifact. Furthermore, as shown in Figures 1B-1 and 1B-2, images taken from the same mouse at different depths in the vessel wall, any remaining intercostal branches and associated adventitial collagen creates a strong SHG signal. This signal is best appreciated towards the adventitial surface (1B-2) but is also evident towards the luminal surface (1B-1) again making it appear as though there is a real accumulation of peri-ostial collagen. Precise intercostal transection greatly reduces these artifacts.

Figure 1.2 compares *ex vivo* and *in situ* aortas from 5 day-old mice

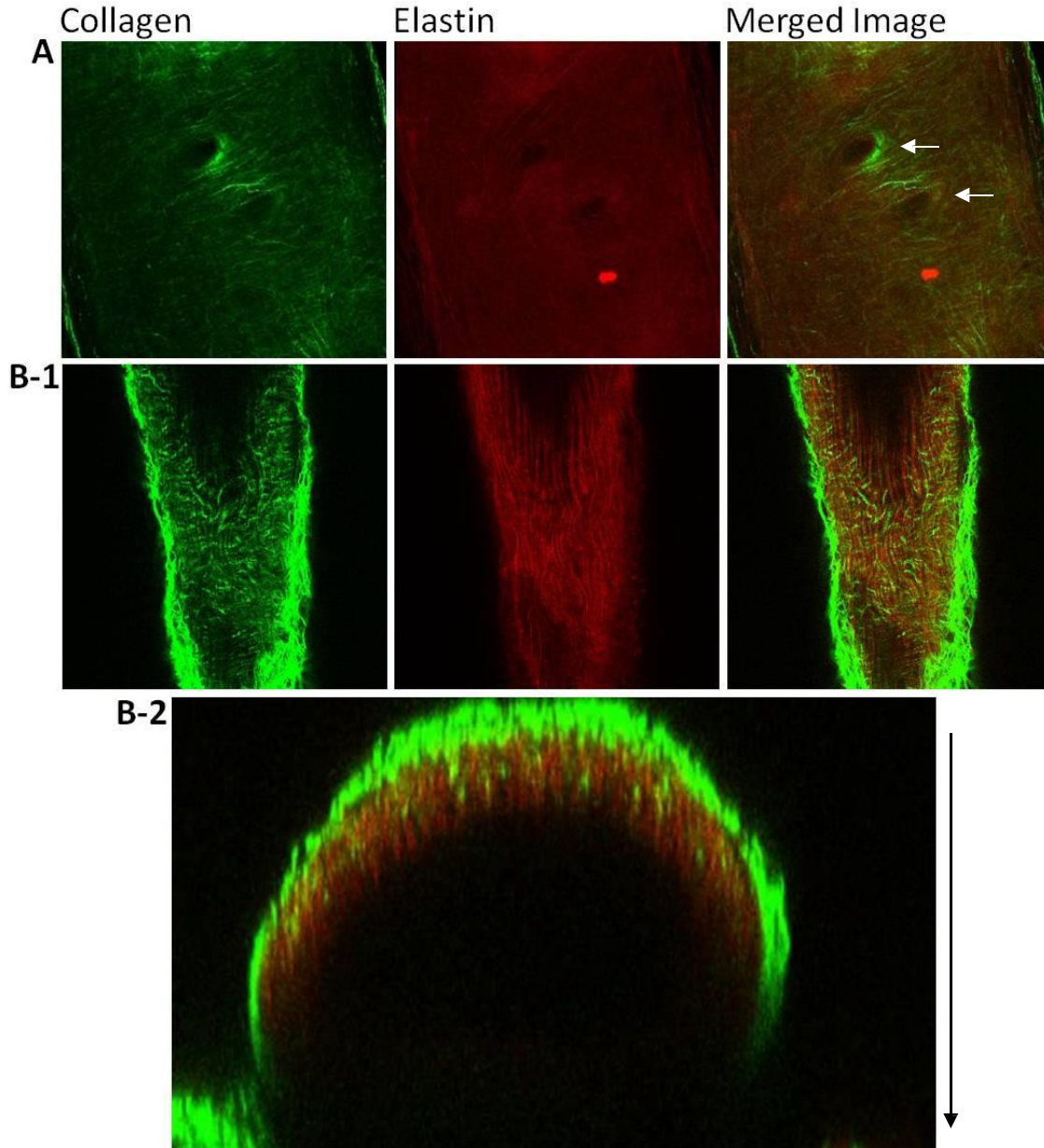


**Figure 1.2:** *Ex vivo* (A) and *in situ* (B-1, B-2) multiphoton images acquired from the thoracic aorta of 5 day-old C57BL/6T (A) and SR-BI<sup>-/-</sup>/ApoE R61<sup>h/h</sup> (B) mice fed NC. (A) White arrows represent bilateral intercostal ostia. (B-2) Full-thickness cross section of the proximal thoracic aorta. Black arrow indicates the direction of laser penetration from the ventral to dorsal aortic surface. Note how the dorsally located intercostal ostia are not captured microscopically. (Images in A and B obtained with Leica, 20x0.7 NA and 20x1.0 NA immersion objective lenses respectively).

In 1.2A, the aorta was excised and mounted on a glass slide without longitudinal incision (patent) and in 1.2B, the aorta was sharply dissected and remains within the mouse attached to the heart, intercostal arteries, bilateral kidneys and ileac arteries (see Fig. 2.1, Ch 2, for *in situ* preparation). Neonatal mouse aortas, as compared to adults, are exceedingly thin and grossly transparent making longitudinal incision difficult to complete without potentially scraping the luminal surface and tearing the vessel wall, hence the patent *ex vivo* approach. With both preparations, the laser is directed at the adventitial surface first causing minor loss in resolution and signal to noise. However, with the *ex vivo* aorta (Fig. 1.2A), the intercostal ostia can be visualized by mounting the vessel on the glass slide so the laser is directed at the dorsal surface first. Intercostal ostia cannot be consistently or clearly imaged in the *in situ* aortas regardless of increased tissue penetration depth afforded by multiphoton microscopy, as the laser is directed at the ventral surface first. The cross section of the entire proximal thoracic aorta (TA) in Figure 1.2B-1 shows that even in neonates, the dorsal surface is not accessible. However, when compared to the *ex vivo* aortas, the overall vascular architecture of the *in situ* aortas is more closely comparable to that in living animals with fewer perturbations in the dissection and mounting process.

In an effort to gain access to the dorsal aortic surface in the *in situ* preparations, a rectangular window was cut into the ventral aortic surface. Although this allowed visualization of the intercostal arteries, it also resulted in mild distortion of the actual shape of the ostia from round to oval by releasing inherent tension provided in vascular patency. Figure 1.3 compares an *ex vivo* TA (1.3B) with an *in situ* TA (1.3A), in which a window has been cut (1.3B), from 2, 2 month-old mice, using the same imaging parameters.

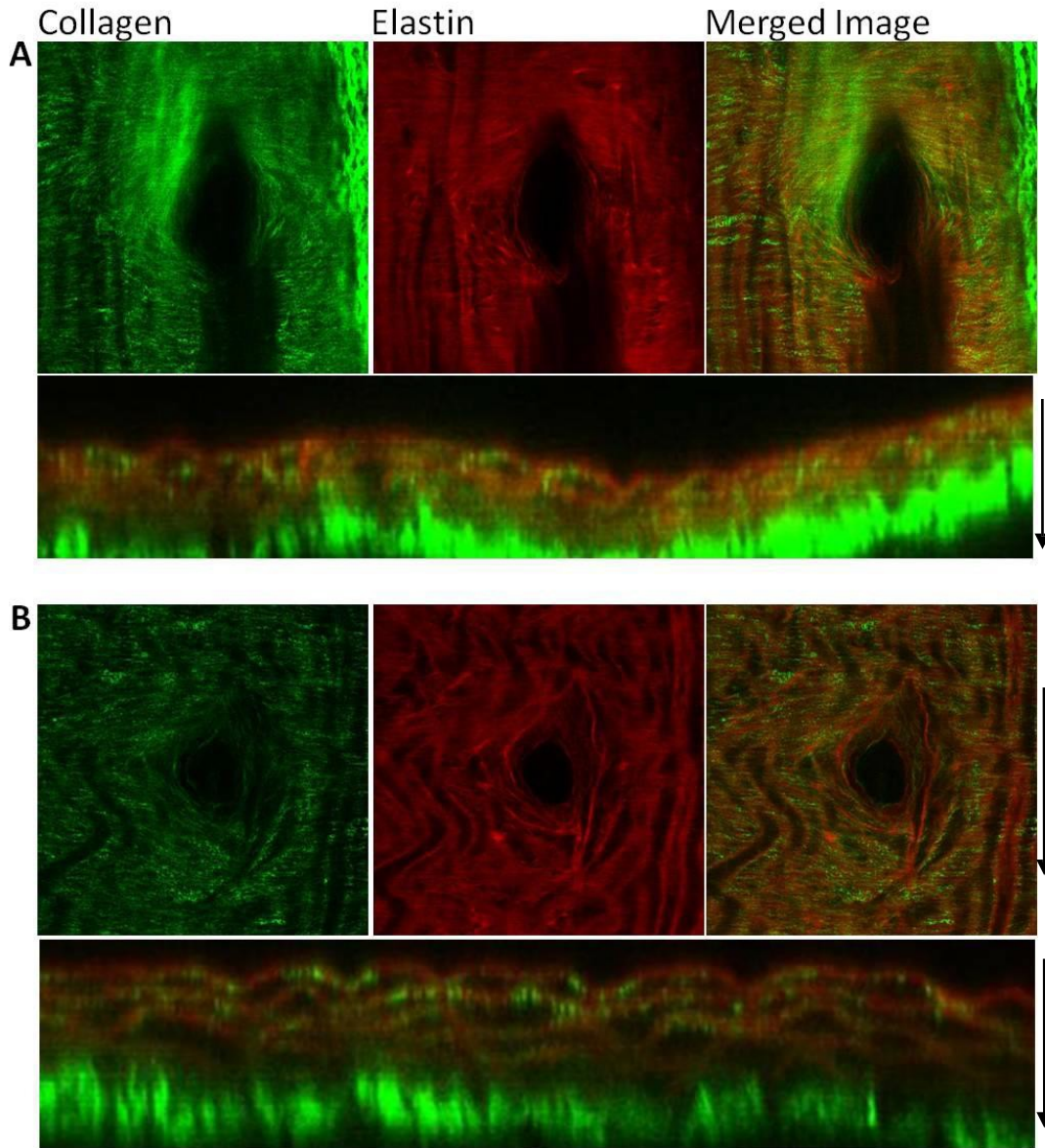


**Figure 1.3:** *In situ* (A) and *ex vivo* (B) multiphoton images acquired from a proximal intercostal ostia of 2, 2 month-old SR-BI<sup>-/-</sup>/ApoE R61<sup>h/h</sup> mice fed NC. Black arrows indicate the direction of laser penetration from the luminal to adventitial surface (A) Note the oval shaped, ostial distortion created by cutting a window through the ventral aortic surface to image the dorsal aortic surface with associated intercostal ostia. (B) Note the increased undulating effect the *ex vivo* aortic preparation has on the vessel wall. (Images obtained with a Leica, 20x1.0 NA immersion objective lens).

The ostial shape change is depicted. This figure also compares the effect that both preparations have on vascular wall contractility. *Ex vivo* aortas are more undulating and contracted down (Fig. 1.3B cross section) while *in situ* aortas have increased associated pressure and strain (Fig. 1.3A) that again may be more comparable to living animals.

The described perturbations were carefully considered in determining the best aortic preparations for each step of this research. For the longitudinal study, it was determined that a patent, *in situ* thoracic aortic preparation would be used as a ventral window was not consistently successful in capturing aortic intercostal ostia.. Alternatively, the ventral window approach was utilized in the atherosclerosis study as a cohort of SR-BI KO/ApoER61<sup>h/h</sup> mice aged 2-3 months old allowed for far superior visualization of the intercostal ostia.

## References

- Albert S, Balaban RS, Neufeld EB, Rossman JS. Influence of the renal artery ostium flow diverter on hemodynamics. *J. Biomechs.* 2014;47:1594-1602.
- Bennett MR. Breaking the plaque. Evidence for plaque rupture in animal models of atherosclerosis. *Arterioscler. Thromb. Vasc. Biol.* 2002;22:713-714
- Boren J, Olin KL, Lee I, Chait A, Wight TN, Innerarity TL. Identification of the principal proteoglycan binding site in LDL. A single point mutation in apoB100 severely affects proteoglycan interaction without affecting LDL receptor binding. *J. Clin. Invest.* 1998;101:2658-2664.
- Braun A, Zhang S, Miettinen HE, Ebrahim S, Hom TM, Vasile E, Post MJ, Yoerger DM, Picard MH, Krieger JL, Andrews NC, Simons M, Krieger M. Probucol prevents early coronary heart disease and death in the high-density lipoprotein receptor SR-BI/apolipoprotein E double knockout mouse. *Proc. Natl. Acad. Sci. USA.* 2003;100(12):7283-7288.
- Camejo G. The interaction of lipids and lipoproteins with the intracellular matrix of arterial tissue: it's possible role in atherogenesis. *Adv. Lipid Res.* 1982;19:1-53.
- Daugherty A. Mouse models of atherosclerosis. *Am. Med. Sci.* 2002;323(1):3-10.
- deLuna A. Mouse models in atherosclerosis. *Drug Discov. Today.* 2008;5(3):157-163.
- Drew AF. Animal models of diet-induced atherosclerosis. *Method. Mol. Med.* 200;52:1-6.
- Flood C, Gustafsson M, Pitas RE, Arnaboldi L, Walzem RL, Boren J. Molecular mechanism for changes in proteoglycan binding on compositional changes of the core and the surface of low-density lipoprotein-containing human apolipoprotein b100. *Arterioscler. Thromb. Vasc. Biol.* 2004;24:564-570.
- Greenow K, Pearce N, Ramji DP. The key role of apolipoprotein E in atherosclerosis. *J. Mol. Med.* 2005;83:329-342.
- Heagerty AM, Aalkjaer X, Bund SJ, Korsgaard N, Mulvany MJ. Small artery structure in hypertension. Dual process of remodeling and growth. *Hypertension.* 1993;21:391-397.
- Ishibashi S, Herz J, Maeda N, Goldstein JL, Brown MS. The two-receptor model of lipoprotein clearance: tests of the hypothesis in "knockout" mice lacking the low density lipoprotein receptor, apolipoprotein E, or both proteins. *Proc. Natl. Acad. Sci. USA.* 1994;91(10):4431-4435.
- Jongstra-Bilen J, Haidari M, Zhu SN, Chen M, Guha D, Cybulsky MI. Low-grade chronic inflammation in regions of the normal mouse arterial intima predisposed to atherosclerosis. *J. Exp. Med.* 2006;203(9):2073-83.
- Krul ES, Tikkanen MJ, Cole TG, Davie JM, Schonfeld G. Roles of apolipoproteins B and E in the cellular binding of very low density lipoproteins. *J. Clin. Invest.* 1985;75(2):361-369.

- Lagor WR, Millar JS. Overview of the LDL receptor: relevance to cholesterol metabolism and future approaches for the treatment of coronary heart disease. *J. Receptor, Ligand and Channel Research*. 2010;3:1-14.
- Lehmann ED, Gosling RG, Sonksen PH. Arterial wall compliance in diabetes. *Diabet. Med.* 1997;102:227-231.
- Lin S-J, Jan K-m, Chien S. Role of dying endothelial cells in transendothelial macromolecular transport. *Arteriosclerosis*. 1990;10:703-709.
- McVeigh GE, Morgan DJ, Finkelstein SM, Lemay LA Cohn JN. Vascular abnormalities associated with long-term cigarette smoking identified by arterial waveform analysis. *Am. J. Med.* 1997;102:227-231.
- Merrilees MJ, Beaumont B, Scott LJ. Comparison of deposits of versican, biglycan and decorin in saphenous vein and internal thoracic, radial and coronary arteries: correlation to patency. *Coron. Artery Dis.* 2001;12(1):7-16.
- Mitchell RN, Schoen FJ. Blood vessels. *In: Robbins and Cotran Pathologic Basis of Disease*, eds. Kumar, Abbas, Fausto, Aster, 8<sup>th</sup> edition. 2010:496-506. Elsevier Saunders, Philadelphia, PA, 2010.
- Moore KJ, Freeman MW. Scavenger receptors in atherosclerosis: beyond lipid uptake. *Arterioscler. Thromb. Vasc. Biol.* 2006;26:1702-1711.
- Nakashima Y, Fujii H, Sumiyoshi S, Wight TN, Sueishi K. Early human atherosclerosis: accumulation of lipid and proteoglycans in intimal thickenings followed by macrophage infiltration. *Arterioscler. Thromb. Vasc. Biol.* 2007;27(5):1159-1165.
- Nakashima Y, Plump AS, Raines EW, Breslow JL, Ross R. ApoE-deficient mice develop lesions of all phases of atherosclerosis throughout the arterial tree. *Arterioscler. Thromb.* 1994;14:133-140.
- Neufeld EB, Yu ZX, Springer D, Yu Q, Balaban RS. The renal artery ostium flow diverter: structure and potential role in atherosclerosis. *Atherosclerosis*. 2010;211:153-158.
- O'Brien KD, Olin KL, Alpers CE, Chiu W, Ferguson M, Hudkins K, Wight TN, Chait A. Comparison of apolipoprotein and proteoglycan deposits in human coronary atherosclerotic plaques: colocalization of biglycan with apolipoproteins. *Circulation*. 1998;98:519-527.
- Pentikainen MO, Oorni K, Lassila R, Kovanen PT. The proteoglycan decorin links low density lipoproteins with collagen type I. *J. Biol Chem.* 1997;272(12):7633-7638.
- Plump AS, Smith JD, Hayek T, Aalto-Setälä K, Walsh A, Verstuyft JG, Rubin EM, Breslow JL. Severe hypercholesterolemia and atherosclerosis in apolipoprotein E-deficient mice created by homologous recombination in ES cells. *Cell*. 1992;71:343-353.
- Potteaux S, Ait-Oufella H, Mallat Z. Mouse models of atherosclerosis. *Drug Discov. Today*. 2007;4(4):165-170.

- Raffai R, Dong L, Farese R, Weisgraber K. Introduction of human apolipoprotein E4 “domain interaction” into mouse apolipoprotein E. *Proc. Natl. Acad. Sci. USA*. 2001;98:11587-11591.
- Raffai RL, Weisgraber KH. Hypomorphic apolipoprotein E mice. *J. Biol. Chem*. 2002;277(13):11064-11068.
- Reddick RL, Zhang SH, Maeda N. Atherosclerosis in mice lacking apoE. Evaluation of lesional development and progression. *Arterioscler. Thromb. Vasc. Biol*. 1994;14:141-147.
- Rigotti A, Trigatti B, Penman M, Rayburn H, Herz J, Krieger M. A targeted mutation in the murine gene encoding the high density lipoprotein (HDL) receptor scavenger receptor class B type I reveals its key role in HDL metabolism. *Proc. Natl. Acad. Sci*. 1997;94:12610-12615.
- Roger VL et al. Executive summary: heart disease and stroke statistics-2011 update. A report from the American heart association. *Circulation*. 2011;123:459-463.
- Rosenfeld ME, Butler S, Ord VA, Lipton BA, Dyer CA, Curtiss LK, Polinski W, Witztum JL. Abundant expression of apolipoprotein E by macrophages in human and rabbit atherosclerotic lesions. *Arterioscler. Thromb*. 1993;13:1382-1389.
- Rosenfeld ME, Polinsky P, Virmani R, Kauser K, Rubanyi G, Schwartz SM. Advanced atherosclerotic lesions in the innominate artery of the apoE knockout mouse. *Arterioscler. Thromb. Vasc. Biol*. 2000;20:2587-2592
- Suo J, Ferrara DE, Sorescu D, Guldberg RE, Taylor WR, Giddens DP. Hemodynamic shear stress in mouse aortas: Implications for atherogenesis. *Arterioscler. Thromb. Vasc. Biol*. 2007;27:346-351.
- Tabas I, Williams KJ, Boren J. Subendothelial lipoprotein retention as the initiating process in atherosclerosis. Update and therapeutic implications. *Circulation*. 2007;116:1832-1844.
- Taylor CA, Hughes TJ, Zarins CK. Finite element modeling of three-dimensional pulsatile flow in the abdominal aorta: relevance to atherosclerosis. *Ann. Biomed. Eng*. 1998;26:975-987.
- Thubrikar M, Robicsek F. Pressure-induced arterial wall stress and atherosclerosis. *Ann. Thorac. Surg*. 1995;59:1593-1694.
- Trigatti B, Covey S, Rizvi A. Scavenger receptor class B type I in high-density lipoprotein metabolism, atherosclerosis and heart disease: lessons from gene-targeted mice. *Biochem. Soc. T*. 2004;32:116-120.
- Trigatti B, Rayburn H, Vinals M, Braun A, Miettinen H, Penman M, Hertz M, Schrenzel M, Amigo L, Rigotti A, Krieger M. Influence of the high density lipoprotein receptor SR-BI on reproductive and cardiovascular pathophysiology. *Proc. Natl. Acad. Sci*. 1999;96:9322-9327.

Vance DE, Vance JE. Assembly and secretion of lipoproteins. *In: Vance D, Vance J, (eds) Biochemistry of lipids, lipoproteins and membranes. Elsevier, Amsterdam.*

Vilahur G, Padra T, Badimon L. Atherosclerosis and thrombosis: insights from large animal models. *J. Biomed. Biotechnol.* 2011;2011:907575. Epub 2011 Jan 2.

Wight TN. Versican: a versatile extracellular matrix proteoglycan in cell biology. *Curr. Opin. Cell Biol.* 2002;14:617-623.

Williams KJ. Arterial wall chondroitin sulfate proteoglycans: diverse molecules with distinct roles in lipoprotein retention and atherogenesis. *Curr. Opin. Lipidol.* 2001;12:477-487.

Williams KJ, Tabas I. The response-to-retention hypothesis of early atherogenesis. *Arterioscler. Thromb. Vasc. Biol.* 1995;15(5):551-561.

Zadelaar S, Kleemann R, Verschuren L, de Vries-Van der Weij J, van der Hoorn J, Princen HM, Kooistra T. Mouse models for atherosclerosis and pharmaceutical modifiers. *Arterioscler. Thromb. Vasc. Biol.* 2007;27:1706-1721.

Zhang S, Picard M, Vasile E, Zhu Y, Raffai R, Weisgraber K, Krieger M. Diet-induced occlusive coronary atherosclerosis, myocardial infarction, cardiac dysfunction, and premature death in scavenger receptor class B Type I-deficient, hypomorphic apolipoprotein ER61 mice. *Circulation* 2005;111:3457-3464.

Zhang SH, Reddick RL, Piedrahita JA, Maeda N. Spontaneous hypercholesterolemia and arterial lesions in mice lacking apolipoprotein E. *Science.* 1992;258:468-471.

## Chapter 2

Study of the Development of the Mouse Thoracic Aorta Three-Dimensional Macromolecular  
Structure Using Two-photon Microscopy



## Study of the Development of the Mouse Thoracic Aorta Three-Dimensional Macromolecular Structure using Two-Photon Microscopy

Leah M. Zadrozny, Edward B. Neufeld, Bertrand M. Lucotte, Patricia S. Connelly, Zu-Xi Yu, Lam Dao, Li-Yueh Hsu, and Robert S. Balaban

Laboratory of Cardiac Energetics (LMZ, EBN, BML, LD, LYH, RSB); Electron Microscopy Core Facility (PSC); and Pathology Core (ZXY), NIH Heart, Lung and Blood Institute, National Institutes of Health, Bethesda, Maryland, USA

### Summary

Using the intrinsic optical properties of collagen and elastin, two-photon microscopy was applied to evaluate the three-dimensional (3D) macromolecular structural development of the mouse thoracic aorta from birth to 60 days old. Baseline development was established in the Scavenger Receptor Class B Type I-Deficient, Hypomorphic Apolipoprotein ER61 (SR-BI KO/ApoE61<sup>hh</sup>) mouse in preparation for modeling atherosclerosis. Precise dissection enabled direct observation of the artery wall in situ. En-face, optical sectioning of the aorta provided a novel assessment of the macromolecular structural development. During aortic development, the undulating lamellar elastin layers compressed consistent with the increases in mean aortic pressure with age. In parallel, a net increase in overall wall thickness ( $p < 0.05$ , in day 60 compared with day 1 mice) occurred with age whereas the ratio of the tunica adventitia and media to full aortic thickness remained nearly constant across age groups (~1:2.6, respectively). Histochemical analyses by brightfield microscopy and ultrastructure validated structural proteins and lipid deposition findings derived from two-photon microscopy. Development was associated with decreased decorin but not biglycan proteoglycan expression. This non-destructive 3D in situ approach revealed the aortic wall microstructure development. Coupling this approach with the intrinsic optical properties of the macromolecules may provide unique vascular wall 3D structure in many pathological conditions, including aortic atherosclerosis, dissections and aneurysms. (J Histochem Cytochem 63:8–21, 2015)

### Keywords

collagen, elastin, two-photon microscopy, aorta, decorin, biglycan, atherosclerosis

### Introduction

The development of the vascular anatomy at a subcellular level is important for understanding the relationship of genetic diseases affecting the macromolecular elements to the role of the macromolecules in common disease processes, such as atherosclerosis. Much of the information collected on the development of vascular macromolecular structures has involved traditional imaging modalities including histopathology and electron microscopy (EM). More recently, nonlinear optical microscopy (NLOM) has

been utilized. NLOM describes a group of imaging modalities that are sensitive to specific molecules and structures in biological systems, which, when coupled together, can

Received for publication May 22, 2014; accepted September 30, 2014.

#### Corresponding Author:

Leah M. Zadrozny, DVM, Molecular Pathology Fellow, Laboratory of Cardiac Energetics, National Heart, Lung, and Blood Institute, National Institutes of Health, 10 Center Drive, Building 10, B1D219, Bethesda, MD 20892-1424, USA.  
 E-mail: zadroznylm@nhlbi.nih.gov

provide important information regarding conditions such as cardiovascular disease as well as cancer development, lipid metabolism, embryogenesis and skin biology (Zipfel et al. 2003; Supatto et al. 2005; Yue et al. 2011). Examples include two-photon excitation fluorescence (TPEF), second-harmonic generation (SHG) and Coherent anti-Stokes Raman scattering (CARS). Multiphoton excitation in biological tissues typically relies on near infra-red light to excite the chromophores and provides inherent 3D spatial resolution with focused excitation. Because linear absorption and scattering in tissues at these wavelengths are generally smaller than those at visible wavelengths, greater imaging depth can be achieved with multiphoton excitation than with linear confocal microscopy (Yue et al. 2011). The penetration depth and 3D resolution capabilities in multiphoton excitation bypass the need for physical sectioning and subsequent data registration required in histopathology and other imaging modalities.

Recently, TPEF has emerged as a powerful method for label-free imaging of living tissues and cells as well as fresh and formalin-fixed postmortem samples. TPEF was first demonstrated in 1990 (Denk et al. 1990), and provides reduced photodamage and fluorophore photobleaching. In TPEF, the target molecules absorb two excitation photons emitted from a pulsed laser to achieve an electron-excited state, which then emit a single fluorescence photon of greater energy than the incident photons (de Grauw et al. 1999). TPEF microscopy has been applied to biological imaging by utilizing intrinsic fluorescence or extrinsic labeling of molecular structures within numerous systems including musculoskeletal, urinary as well as neurological and cardiovascular. With regard to vascular imaging, elastin fibers are readily visualized due the presence of endogenous chromophores found, for example, within certain amino acid chains rich in tryptophan and tyrosine, which imparts inherent autofluorescence (Richards-Kortum and Sevick-Muraca 1996). Low-density lipoprotein (LDL) binding, proteoglycan (PG) labeling, and subendothelial lipid deposition can also be effectively imaged using TPEF in combination with the appropriate fluorophores and fluorescent lipid dyes, including Nile Red (NR) (Yu et al. 2007; Kwon et al. 2008). It is important to note though, as previously described by Kwon et al. (2008), that the fluorescence emission spectra of elastin is quite broad and shifts with varying excitation frequency, suggesting that elastin has multiple chromophores contributing to fluorescence emission (Kwon et al. 2008). This must be taken into consideration when choosing fluorescent probes to minimize any potential overlap in emission spectra.

SHG, another example of NLOM, is a nonlinear scattering process allowing for the visualization of unstained, endogenous noncentrosymmetric proteins such as fibrillar collagen (Strupler et al. 2007). Similar to TPEF, SHG provides intrinsic three-dimensionality as well as increased tissue penetration depth.

The present study offers a new methodology combining previously described multiphoton microscopy with a novel, *in situ* dissection of the ventral (anterior) surface of the mouse thoracic aorta (VTA). This approach was used to complete a longitudinal analysis of the developing thoracic aorta in mice aged 1–60 days old (do). Additional benefits of this preparation included not having to: 1) mount blood vessels into a perfusion chamber, as required for some vascular experiments; 2) mount small vascular segments onto glass slides that are cover slipped and sealed for further multiphoton imaging, and; 3) perturb the vascular bed during *in situ* dissection. Although transmural physiological pressure is minimal in this preparation, the longitudinal stretch maintained mimics that *in vivo*, and compares to that obtained while mounted within a perfusion chamber. Longitudinal stretch is also not completely lost, as is the case when smaller vessel segments are dissected and mounted between a glass slide and cover slip. As a comparison, histopathology and EM were completed in parallel.

Although any strain of mouse could have been used for this preparation, we reasoned that a more useful control would be a strain that could be induced to form atherosclerosis. We chose the recently described SR-BI KO/ApoE61<sup>hh</sup> mouse model of atherosclerosis (Zhang et al. 2005), maintained under normal dietary conditions thereby limiting the induction of vasculopathy as a control condition. This was done so that future studies evaluating the macromolecular events associated with atherosclerosis in this model could be compared directly to these data using the approach documented herein.

## Materials & Methods

### Animals

SR-BI KO/ApoE61<sup>hh</sup> mice obtained from Dr. Alan Remaley at the National Heart Lung and Blood Institute (NHLBI) in Bethesda, MD, were bred, as previously described (Zhang et al. 2005). Gestating and neonatal mice (<3 weeks old) were fed a breeder diet (20% protein, 9% fat, 5% fiber, LabDiet, mouse breeder diet 5021) and weaning mice (>3 weeks old) were fed a normal chow (NC) diet (18% protein, 4% fat, 5% fiber, Zeigler Feed, NIH-31 open formula). All experiments on animals were performed according to the research protocol (H-0257) approved by the Animal Care and Use Committee of the NHLBI at the National Institutes of Health.

### Mouse Thoracic Aorta Preparation for Multiphoton Microscopy

VTAs were dissected within male and female mice fed breeder chow aged 1, 10 and 20do, and NC aged 30 and 60do ( $n=5$  per age group). Mice  $\leq 20$ do were euthanized

with a lethal dose of sodium pentobarbital (150 mg/kg) injected intraperitoneally and otherwise prepared for dissection according to our approved animal study. Mice >20d were placed in an anesthesia box for induction and then ventilated by a nose cone with a mixture of 2.5% isoflurane in oxygen and euthanized via a double thoracotomy. The caudal vena cava was transected and blood was removed from the heart and thoracic aorta by perfusion of the left ventricle with <6 ml cold, 1× phosphate-buffer solution (PBS) followed by slow perfusion with NR (100 µg/ml in 200 µL sterile saline, Life Technologies; Invitrogen; Grand Island, NY) for lipid staining. While secured on an ice cold aluminum block, mice were prepared to expose the heart, bilateral kidneys and the entire length of the thoracic aorta intact by sharp dissection. The abdominal organs were removed and the mesenteric vessels were transected at the level of the abdominal aorta. VTAs were prepared by removing the perivascular adipose tissue. Intercostal arteriolar branches were left intact. The entire length of the thoracic aorta, while still attached to the heart, kidneys and vertebral column, remained patent. The limbs were disarticulated and removed along with the skin and tail, and the ribs and soft tissue were trimmed bilaterally to within 5 mm of the vertebral column (Fig. 1). These preparations were pinned in place with insect specimen mounting pins (Fine Science Tools; Foster City, CA), on either side of the vertebral column onto 20% agar gel platforms. Additional pins were appropriately placed between the 3<sup>rd</sup> and 5<sup>th</sup>-, the 8<sup>th</sup> and 9<sup>th</sup>-, and the 11<sup>th</sup> and 12<sup>th</sup> intercostal branches to consistently position the proximal, mid- and distal VTAs across all aortic preparations for imaging upon completion of a thorough scan of the entire VTA. Imaging of the dorsal (posterior) surface of the thoracic aorta, with intact intercostal ostia, was beyond the depth penetration capability of the Leica SP5 laser (MaiTai HP, Spectra-Physics/Newport; Mountain View, CA). Prior to imaging, aortas were submerged in optical coupling gel (NHLBI-NIH), with a refractive index similar to that of water, or saline. Mid- and distal VTA images along with movies of the proximal VTA may be found in Fig. 2 and the Supplemental Materials section, respectively.

### *Multiphoton Laser Scanning Microscopy*

In situ, two-photon images of the VTA were acquired from the luminal surface out to the aortic tunica adventitia. A Ti:sapphire laser (MaiTai DS, Spectra-Physics/Newport) was tuned to 820 nm for excitation. For the majority of the experiments, a water dipping 25×, 1.1 NA objective lens (Nikon; Tokyo, Japan) was used for both saline submerged and optical gel-coupled aortic preparations. Three photomultiplier tubes (PMTs) were used to collect the emitted photons in non-descanned mode and provided three spectral channels to separate collagen, elastin and the lipophilic,

exogenous probe, NR, as previously described (Kwon et al. 2008). Briefly, collagen SHG was detected at 395–410 nm (PMT I), elastin fluorescence at 435–495 nm (PMT II), and NR (lipid) fluorescence at 570–640 nm (PMT IV). Three-dimensional images from each PMT at 512×512 pixels, with a frame rate of 700 Hz, a 1.7 optical zoom and a step section of 1 µm were collected as a stack of images beginning at the luminal surface and ending at the tunica adventitia. Images were analyzed using ImageJ (NIH; Bethesda, MD) and applying independent component analysis (ICA) for signal to noise enhancement (Dao et al. 2014). Aortic wall thickness measurements were taken on the ventral (anterior) surface from the two-photon images at three standard positions: 3-, 6- and 9-o'clock. To determine the relationship between residual strain and IEL undulation, the distance between undulating peaks, or spatial frequency, was measured ( $n=15$  measurements/mouse).

### *Independent Component Analysis*

Our laboratory recently demonstrated the use of ICA (Dao et al. 2014) as a method to improve the signal-to-noise ratio but also the spatial discrimination in multi-probe fluorescence imaging experiments. In this application, we used ICA to primarily improve the spatial discrimination between the collagen, elastin and NR (lipid) signals. ICA requires that there be no spatial overlap between signals; i.e., only one signal originates from each pixel. In a preliminary study, we established that the spatial overlap between collagen SHG, elastin and NR fluorescence is minimal due to the high spatial resolution. Using this assumption, ICA permitted the determination of the best statistical solution of the images where the signal overlap between all three signals was minimized. This essentially removed the "cross-talk" between spectral channels. This is significant because the cross-talk from elastin to the other channels cannot be completely suppressed with conventional filters alone due to its broad emission spectrum (Kwon et al. 2008).

After the ICA analysis, a background threshold was determined to be the mean of the NR signal plus the standard deviation of this signal to improve the overall image contrast. The NR signal was used as a reference for the background, as it was the weakest signal collected. With the NR signal thresholded to zero, we used a background region of the image and created the threshold at the mean of the background signal plus the standard deviation of the background signal.

Given that this is a relatively new approach, we have provided raw data without ICA processing (Supplemental Fig. 1) along with the ICA processed data (Fig. 3) for comparison. We did not observe any image distortions or inappropriate signal distributions generated by the ICA image processing approach.

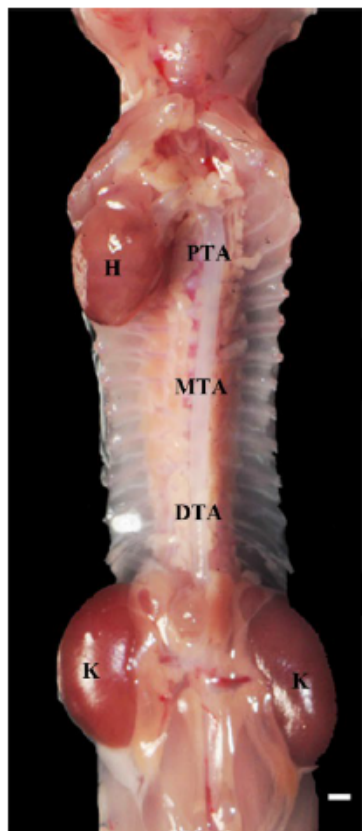


**Figure 1.** In situ dissection of the mouse thoracic aorta in dorsal recumbency. The heart (H), kidneys (K), and three regions of interest—the proximal (PTA), mid (MTA) and distal (DTA) thoracic aorta—are labeled. Multiphoton images are all depicted with the head and tail ends of the mice at the top and bottom of each image, respectively. Full-thickness z-stacks were obtained from the luminal to the adventitial surfaces of the ventral thoracic aorta. Scale, 1 mm.

### Histopathology

An additional group of age-matched mice ( $n=5$  per age group) was processed for histopathology and transmission EM. Thoracic aortas were perfusion-fixed with 4% paraformaldehyde, and transected at the levels of the aortic root, mid- and distal thoracic regions. Proximal to mid-thoracic segments were placed into 10% buffered formalin and embedded in paraffin. Serial cross sections were cut at the level of the proximal descending thoracic aorta and stained with hematoxylin and eosin (H&E), Movat's pentachrome ((collagen, elastin and glycosaminoglycans) Polysciences,

Inc.; Warrington, PA), and Picrosirius Red ((collagen) Polysciences, Inc.) for morphological evaluations. Immunohistochemistry (IHC) was performed with an indirect peroxidase method. Paraffin sections were de-waxed, rehydrated and pretreated with Chondroitinase-ABC, (Seikagaku Biobusiness, 1U/ml) for 30 min at 37C. Primary antibodies against Decorin (1:200, R&D Systems; Minneapolis, MN) and Biglycan (1:75, Abcam; Cambridge, MA) were incubated overnight at 4C. Following PBS washing, sections were incubated with biotinylated secondary antibodies (ABC Elite kits, Vector Laboratories; Burlingame, CA), then with peroxidase-conjugated ABC reagent, according to the manufacturer's directions. The reactions were visualized using 3, 3'-diaminobenzidine (DAB) substrate (Vector Laboratories) for 5 min. Nuclei were then counterstained with hematoxylin. Negative controls were performed each time with omitted primary antibodies and all gave negative results. Histology images were taken using a Leica NB 4000 digital camera. Mid- to distal thoracic aortic segments were processed for EM as described below.

### Electron Microscopy

Distal thoracic aortas were fixed with 2.5% glutaraldehyde, 4% paraformaldehyde, 0.12 M sodium cacodylate, post-fixed in 1% osmium tetroxide, block-stained in 1% uranyl acetate, dehydrated in graded ethanol solutions, and embedded in EMbed-812 (Electron Microscopy Sciences; Hatfield PA). Ultra-thin sections from the distal aortas were stained with uranyl acetate and lead citrate then examined on a JEM 1400 electron microscope (JEOL USA; Peabody MA) equipped with an AMT XR-111 digital camera (Advanced Microscopy Techniques Corporation; Woburn, MA). Semi-thin sections (0.5  $\mu\text{m}$ ) were taken from the blocks prepared for EM and stained with toluidine blue for lipid identification by light microscopy.

### Statistical Analysis

All data are presented as mean  $\pm$  SEM. Proximal VTA wall thickness, including the tunics media and adventitia, was assessed and compared between age groups by two-tailed Student's *t*-test. The significance level was set at  $p<0.05$ .

## Results

### Multiphoton Analysis of the Proximal Thoracic Aorta

The 3D structural development of collagen and elastin was evaluated along the entire length of the VTA across all age groups, and z-stacks were obtained for post-image

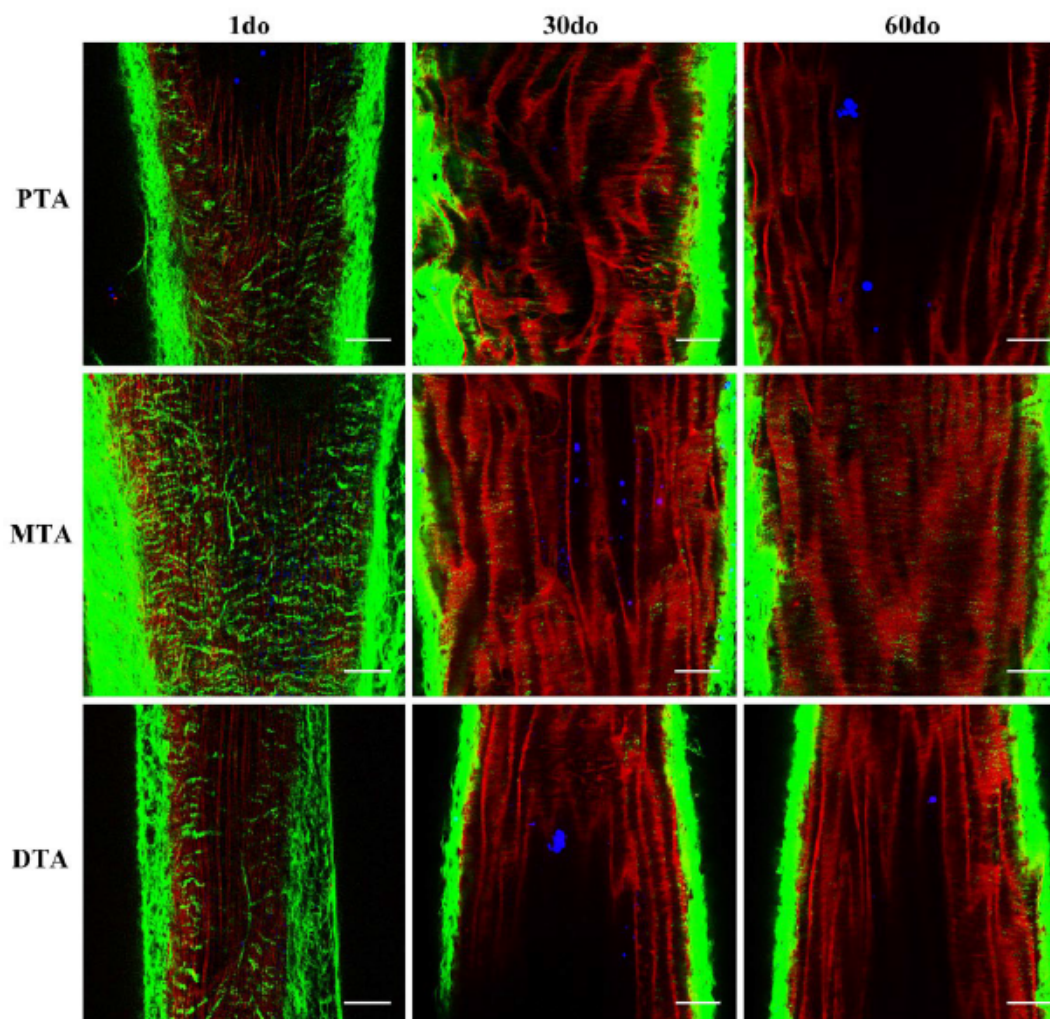


**Figure 2.** Multiphoton images from the proximal, mid and distal thoracic aorta (PTA, MTA and DTA) of 1 day old (do), 30do and 60do SR-BI<sup>+/+</sup>/ApoE61<sup>+/+</sup> mice. Images depict 1- $\mu$ m-thick optical slices captured from full-thickness z-stacks within the tunica media. Sections are representative of the thoracic aortic regions of interest, as shown in the *in situ* mouse preparation in Figure 1, with the head and tail ends of the mice at the top and bottom of each image, respectively. Collagen (green), elastin (red) and lipid (blue) signals are merged after post-image processing by Independent Component Analysis (ICA). Scale, 50  $\mu$ m.

processing from the proximal, mid- and distal VTA. Given the similarities observed within the vascular bed (Fig. 2), coupled with the fact that a predominance of atherosclerotic lesions occur at this site and within the aortic arch (Tangirala et al. 1995; McGillicuddy et al. 2001; Haidari et al. 2010) in mouse models induced to develop atherosclerosis, sections from the proximal VTA remained the primary focus.

The collagen and elastin microstructure formed a variably confluent, wavy meshwork of elastin throughout the

tunica intima and tunica media around which variably dense, fibrillar strands of collagen were circumferentially arranged (best appreciated in cross sections; Fig. 3, Fig3video1.avi, Fig4video2.avi, Figure 4, and Supplemental movies I-X). The density of this matrix and overall abundance of elastin and collagen was interpreted to increase with age; however, the changes noted from 20–60 do mice were minimal. These findings are consistent with previous gene expression analyses, in which the expression of genes

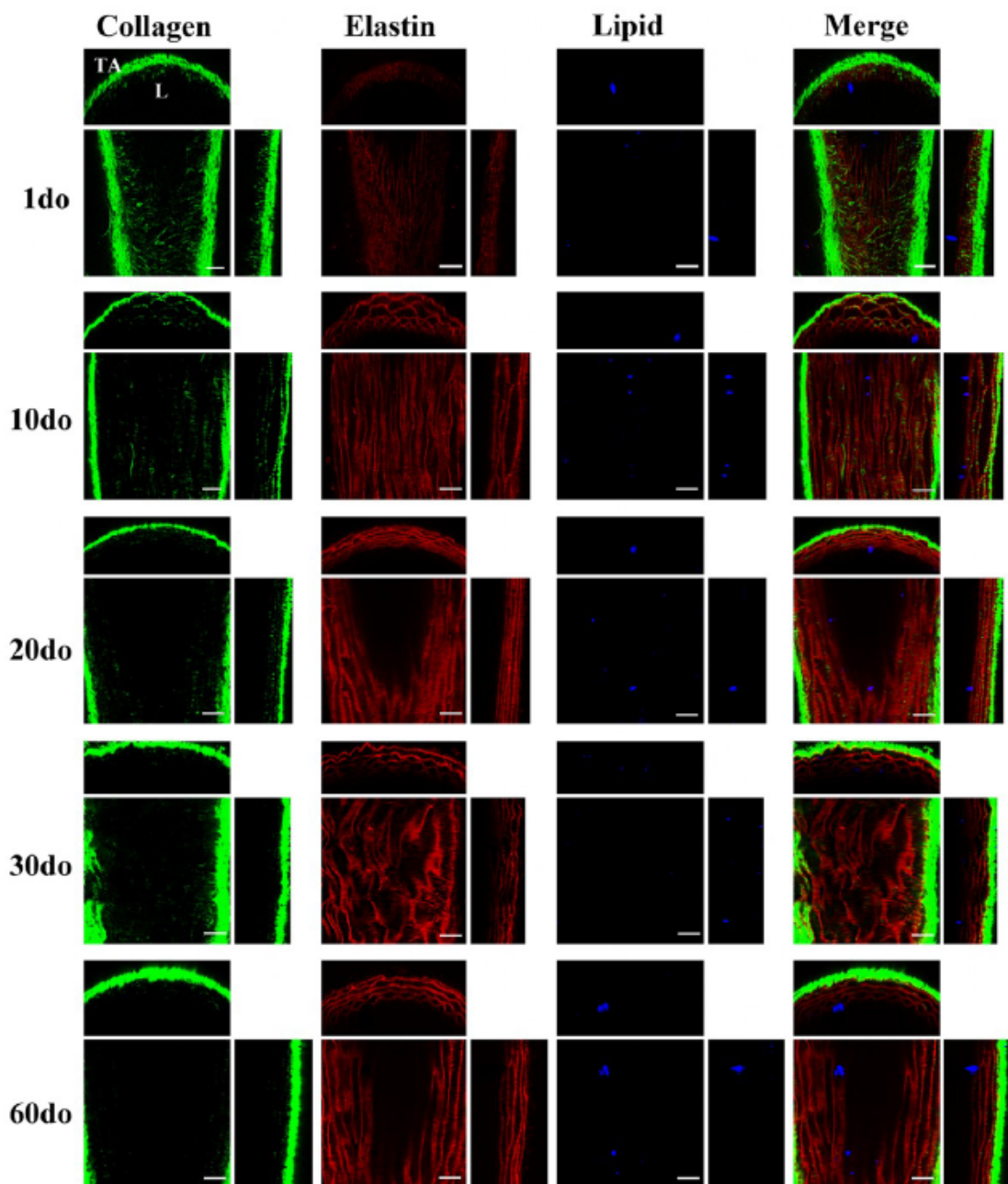


**Figure 3.** Multiphoton, in situ images acquired from the proximal ventral (anterior) thoracic aortas (VTAs) of representative  $SR-BI^{-/-}$   $ApoE61^{hh}$  mice aged 1–60 days old (do). Images depict 1- $\mu$ m-thick optical slices captured from full-thickness z-stacks within the tunica media of the proximal VTA. For each individual orthogonal panel, the center, top and right sections depict en-face ( $xy$ ), cross/transverse ( $xz$ ) and sagittal ( $yz$ ) sections, respectively. Collagen second harmonic generation (SHG) is green, elastin auto-fluorescence is red and Nile Red (NR) lipid droplet fluorescence is blue. Independent component analysis (ICA) was applied to all z-stacks for post-image processing to eliminate signal overlap and background noise. For raw images, and full thickness movies, please refer to the Supplemental Materials section. L, lumen; TA, tunica adventitia. Scale, 50  $\mu$ m.

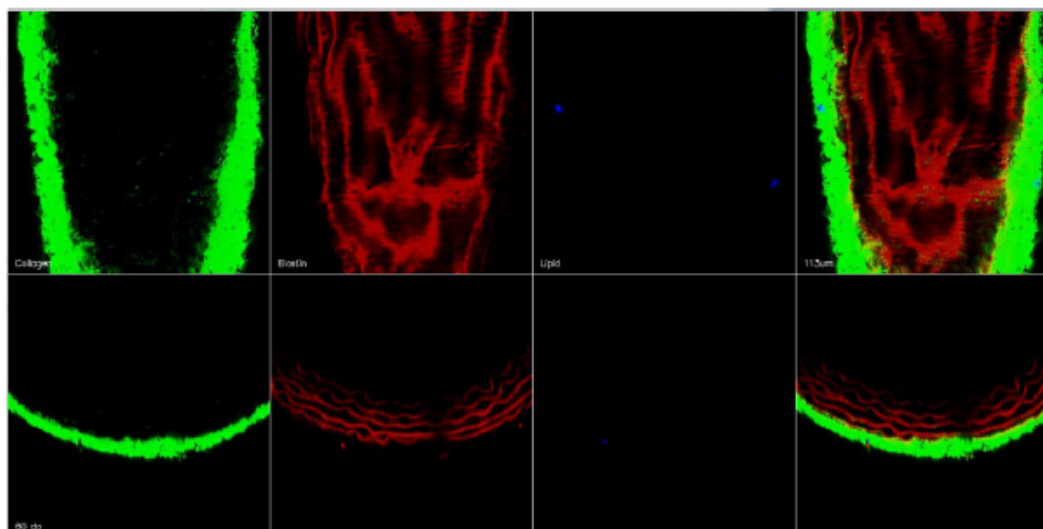


**Fig3 video1.** AVI video clips were produced from a full-thickness z-stack (ranging from ~150–200- $\mu\text{m}$ -thick tissue image acquisitions) obtained within the ventral (anterior) surface of the proximal thoracic aorta of a representative SR-BI<sup>-/-</sup>/ApoE61<sup>h/h</sup> mouse aged 60 days old (do). En-face projections coupled with cross sections are provided. Collagen second harmonic generation (SHG) is green, elastin auto-fluorescence is red and Nile Red (NR) lipid droplet fluorescence is blue. Image acquisition was optimized during all experiments to fill the digitizer. ICA was applied during post-image processing and the elastin fluorescence signal was optimized across all age groups for comparison purposes. Additional movies are provided in the Supplemental Materials.

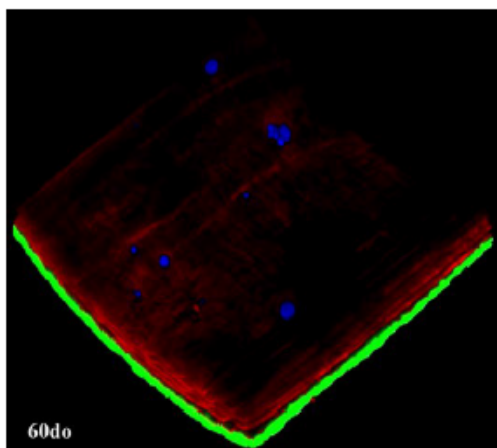


**Fig4 video2.** An AVI video clip produced from a maximum projection, three-dimensional (3D) rendering from a z-stack of the proximal ventral (anterior) thoracic aorta (VTA) of a representative SR-BI<sup>-/-</sup>/ApoE61<sup>h/h</sup> mouse aged 60 days old (do) is provided. For color scheme and post-image processing information, see Fig3video1. Additional 3D renderings are provided in the Supplemental Materials.

encoding proteins for collagen and elastin peaked at approximately 15 days postnatally, followed by a gradual decrease

in expression 2–3 months thereafter (Kelleher et al. 2004; Wagenseil et al. 2009). Additionally, a markedly enhanced SHG signal was recorded when transitioning from the tunica media into the tunica adventitia where the collagen fibrils are more abundant and irregularly arranged, and this increased with age.

Lipid droplets were individualized or arranged as small clusters, ranging from 1–30  $\mu\text{m}$  in diameter (Figs. 3–4, and Supplemental Movies I–X), and were visualized along the entirety of the VTA, primarily on the luminal surface within the vascular endothelium or directly beneath the internal elastic lamina (IEL). In previous experiments in our laboratory, di-8-ANEPPS (Invitrogen), a fluorescent probe that binds the vascular endothelium and phospholipid bilayer membranes, was administered through an intra-cardiac injection, as described for NR in the Materials & Methods. To help confirm lipid droplet location in the present study, en-face and cross-sectional movies have been included in the Supplemental Materials (Supplemental AVI movies XIII–XIV). Lipid droplets (black hollow spheres outlined in blue) are appreciated resting on the stained vascular endothelium (blue), indicating that the lipid droplets within this z-stack are likely captured on the vascular luminal surface directly on the endothelium and within the endothelial cell cytoplasm.

The average thoracic aortic wall thickness is summarized in Table 1. As expected, the average full thickness (FT) significantly increased with age ( $p < 0.05$ ) for mice

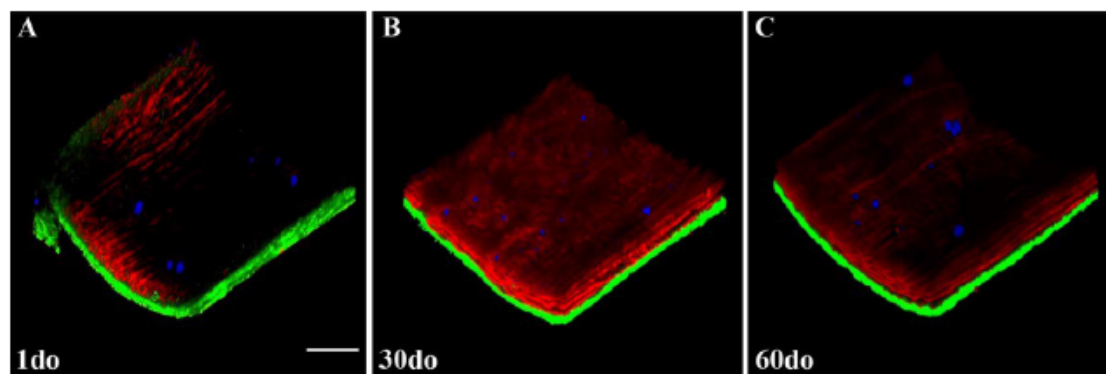


**Figure 4.** Three-dimensional, multiphoton, maximum projection renderings (approximate size  $512 \times 512 \times 150\text{--}200 \mu\text{m}$ ) from z-stacks of the proximal ventral (anterior) thoracic aortas (VTAs) of SR-BI<sup>-/-</sup>/ApoeR61<sup>h/h</sup> mice aged 1, 30 and 60 days old (do). Collagen second harmonic generation (SHG) is green, elastin auto-fluorescence is red and Nile Red (NR) lipid droplet fluorescence is blue. Independent component analysis (ICA) was applied to all z-stacks for post-image processing. For a more detailed view, please refer to the movies in the Supplemental Materials. Scale bar, 50  $\mu\text{m}$ .

**Table 1.** Average Proximal Thoracic Aortic Wall Thickness in SR-BI KO/ApoeR61<sup>h/h</sup> Transgenic Mice Fed Normal Chow.

Ventral (Anterior) Proximal Thoracic Aorta	1do	10do	20do	30do	60do
<b>Full thickness (<math>\mu\text{m}</math>)</b>	$50.73 \pm 2.66$	$58.71 \pm 1.31$	$58.52 \pm 2.10$	$67.51 \pm 1.76$	$72.67 \pm 2.80$
<b>Tunica adventitia thickness (<math>\mu\text{m}</math>)</b>	$15.74 \pm 0.57$	$14.49 \pm 0.44$	$16.57 \pm 0.39$	$18.76 \pm 0.32$	$21.96 \pm 0.74$
<b>Tunica media thickness (<math>\mu\text{m}</math>)</b>	$34.99 \pm 2.87$	$44.22 \pm 0.88$	$41.95 \pm 2.23$	$48.78 \pm 1.72$	$50.71 \pm 2.70$
<b>AT/FT (%)</b>	31	24	28	28	30
<b>MT/FT (%)</b>	69	76	72	72	70

Values are mean  $\pm$  SEM. Three to 5 animals per group with 3 wall thickness measurements per animal. AT, adventitial thickness; MT, medial thickness; FT, full thickness; do, days old.

aged 20do, 30do and 60do when compared with 1do mice (Fig. 5A). The ratios of the wall thickness of the tunics adventitia and media to full aortic thickness exhibited the greatest significance when comparing 1do mice with 10do mice ( $p=0.032$ ), whereas minimal significance was noted when comparing 1do mice with 30do mice ( $p=0.048$ ) and 10do mice with 20do mice ( $p=0.047$ ) (Fig. 5B). This indicates that, although the average VTA FT significantly increased with age, the individual layers increased proportionally in comparison to FT across the age groups.

The average distance between undulating peaks in the IEL is summarized in Table 2. The distance between peaks linearly increased from  $10.61 \pm 0.35 \mu\text{m}$  in 1do mice to  $29.51 \pm 0.90 \mu\text{m}$  in 20do mice and then began to plateau at  $31.03 \pm 0.35 \mu\text{m}$  and  $32.27 \pm 0.46 \mu\text{m}$  in 30 and 60do mice, respectively.

### Histopathology Study

Histologically, proximal VTAs varied the most from 1do up to 20do (Fig. 6). The IEL, medial elastic laminae (MEL)

and external elastic lamina (EEL) in 1do and 10do mice were undulated (Movat's pentachrome) and lined by plump endothelial cells (H&E). Lamellae began to flatten out and endothelial cells became more attenuated by 10do. Sections of the thoracic aorta fixed in Optical Cutting Temperature medium (Tissue-Tek® OCT, Miles; Elkhart, IN) frozen on dry ice and submitted to the NHLBI pathology core laboratory for lipid analysis using Oil-Red-O failed revealed lipid accumulation throughout all age groups (Oil-Red-O histology not shown).

Collagen deposition determined by picrosirius red stain showed the fibrillar structure of medial and adventitial collagen deposition with increased signal and accumulation in the adventitia of older mice (Fig. 6B, 6E, 6H, 6K and 6N). Movat's pentachrome collagen staining was most apparent within the tunica adventitia and muted throughout the inter-lamellar smooth muscle layers (Fig. 6C, 6F, 6I, 6L and 6O). These findings further support both the increased sensitivity and variation in collagen SHG signal observed with two-photon microscopy in the vessel wall. Movat's pentachrome stain revealed little proteoglycan deposition (green/blue)

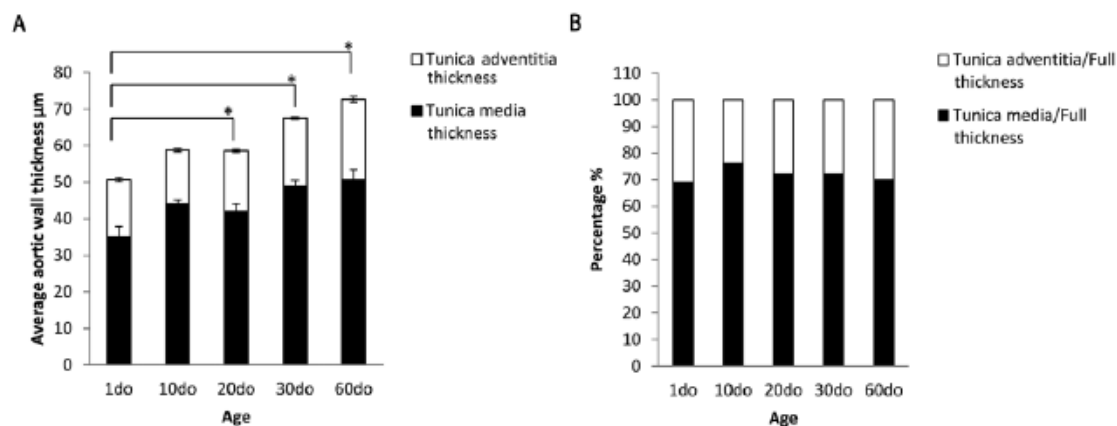


**Figure 5.** Bar graphs showing the average thoracic aortic wall thickness. (A) Average ventral (anterior) thoracic aortic (VTA) full thickness (FT) (total bar height) significantly increased with age ( $^*p < 0.05$  for mice aged 20 days old (do), 30do and 60do when compared to 1do mice) with no significant change in 10do mice as compared with 20do mice. Values are mean  $\pm$  SEM. (B) Ratios of the wall thickness of the tunica adventitia and tunica media to full VTA thickness. The greatest significance is exhibited when 1do mice are compared to 10do mice ( $p = 0.032$ ), and minimal significance when 1do mice are compared to 30do mice ( $p = 0.048$ ) and 10do mice are compared to 20do mice ( $p = 0.047$ ). This indicates that the thickness of the individual tunics within the thoracic aorta increases proportionally with age.

**Table 2.** Average Distance between Undulating Peaks in the Internal Elastic Lamina (IEL) in SR-BI KO/ApoeR61<sup>hh</sup> Transgenic Mice Fed Normal Chow.

Ventral (Anterior) Proximal Thoracic Aorta	1do	10do	20do	30do	60do
Average distance between IEL peaks ( $\mu\text{m}$ )	10.61 $\pm$ 0.35	22.93 $\pm$ 0.46	29.51 $\pm$ 0.90	31.03 $\pm$ 0.35	32.27 $\pm$ 0.46

Values are mean  $\pm$  SEM. Four to five animals per group with 15 internal elastic lamina (IEL) measurements per animal.

transmurally through the proximal thoracic aorta (Fig. 6C, 6F, 6I, 6L and 6O).

Immunoreactivity for decorin and biglycan, small leucine-rich repeat (SLRP) dermatan sulfate proteoglycans, yielded similar findings regarding subendothelial and adventitial deposition (Supplemental Fig. 2). The strongest immunoreactivity occurred in both the tunica adventitial collagen and subendothelium, while weaker positive reactivity occurred within the interlamellar layers of the media throughout all age groups. However, immunoreactivity of decorin within the tunica media appeared to decrease with age while remaining similar across age groups for biglycan. Intercostal ostia that were captured in cross sections exhibited strong positive immunoreactivity within the subendothelium and tunica media for both proteoglycans (Supplemental Fig. 2C and 2G–J).

### Electron Microscopy Study

Sections from the distal thoracic aorta were evaluated. Distinct, circumferential layers of vascular smooth muscle

cells were well defined at 1do and interposed between incompletely developed elastic laminae that exhibited occasional gaps along the length of individual lamina (Fig. 7). By 10do, five, nearly continuous elastic laminae were consistently discerned throughout the entirety of the thoracic aorta (images not shown). Variably sized, intracellular lipid droplets (up to 2  $\mu\text{m}$  in diameter) were observed within endothelial cells (Fig. 7C, 7E, 7G–7I) and within smooth muscle cells (Fig. 7B, 7C, 7H–7I) directly beneath the IEL across all age groups. Lipid droplets were also present within the subendothelium of an intercostal ostial ridge of a 30do mouse captured in Figure 7F. Endothelial cell phagocytosis of lipid can be appreciated in multiple sections of all age groups (Fig. 7A). A focally extensive accumulation of variably sized, intimal lipid droplets admixed with calcified and mineralized debris was indicative of early atherosclerotic lesion formation in a 60do mouse (Fig. 7J). This was not considered a surprising finding though as morbidity did occasionally occur within our mouse colony due to cardiovascular disease in aged (less than 1yo) SR-BI KO/ApoeR61<sup>hh</sup> mice fed the NC diet. Despite finding evidence

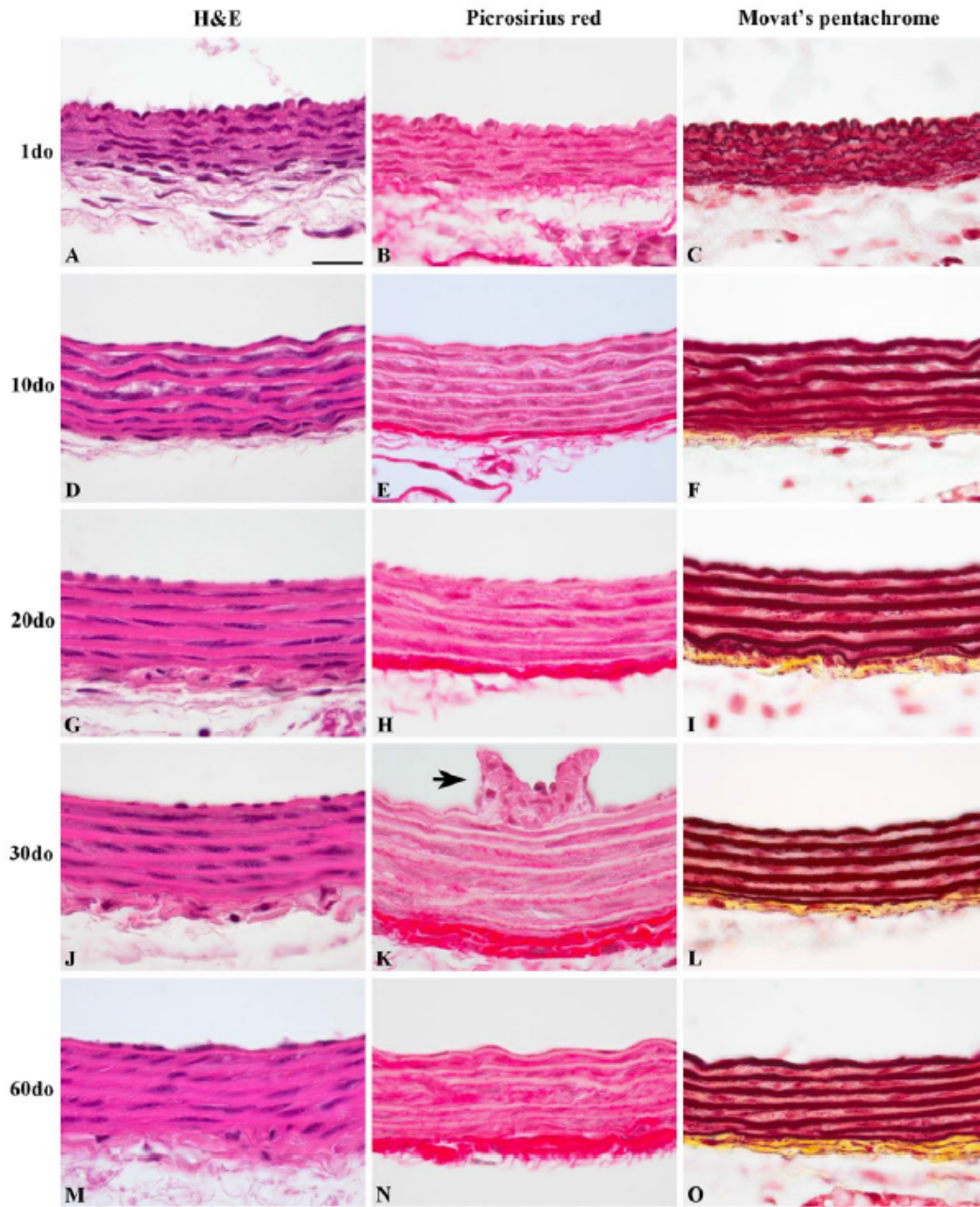


**Figure 6.** Histological features of representative proximal thoracic aortas (PTAs) from SR-BI<sup>-/-</sup>/ApoE R61<sup>hh</sup> mice aged 1–60 days old (do). PTAs were stained with picosirius red (B, E, H, K, and N) for collagen (red fibrils), and Movat's pentachrome (C, F, I, L and O) for collagen (yellow), elastin (black/red), and glycosaminoglycans (green/blue), for which minimal staining is appreciated. Note the frequent undulation present at 1do (A–C), which dissipates by 10do and is absent in mice aged 20do and older. An intercostal ostium (K, black arrow) with collagenous ridges protruding into the luminal surface can be appreciated within the TA. All images are oriented with luminal surfaces at the top and external adventitial surfaces at the bottom of the photomicrographs. Scale, 20  $\mu$ m.

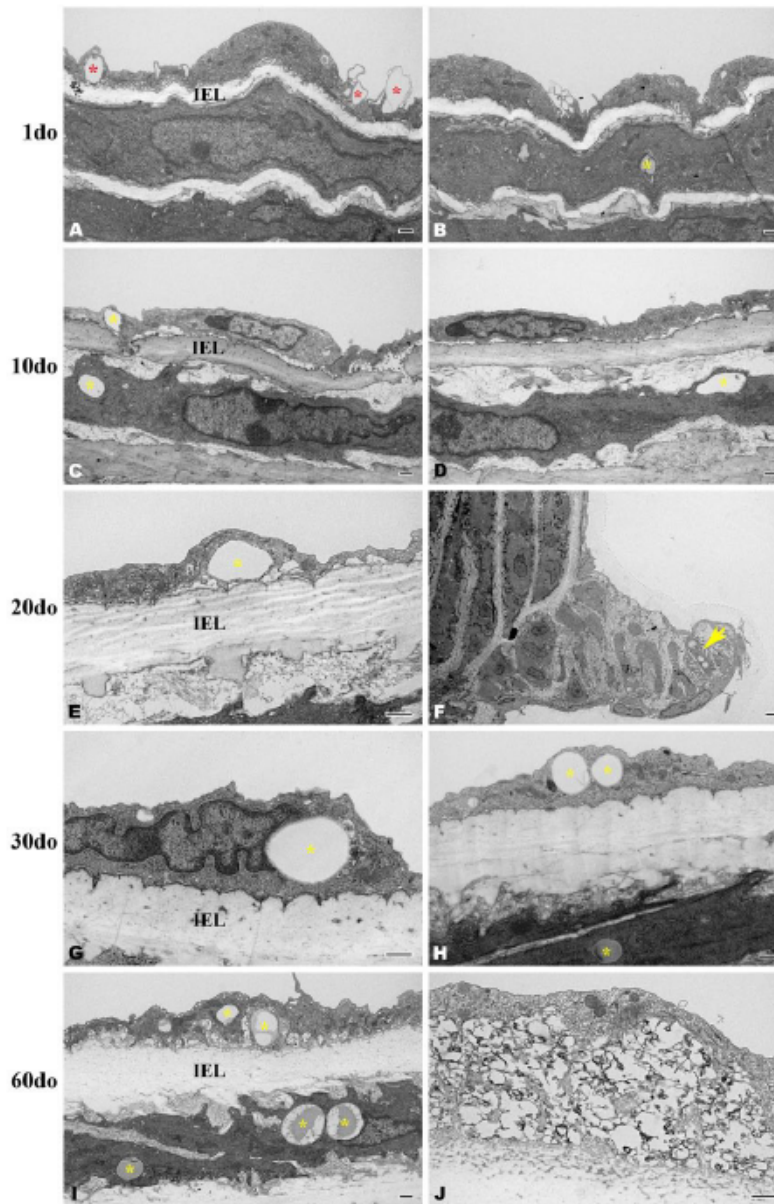


**Figure 7.** Transverse, osmicated electron micrographs showing the deposition of lipid within the distal thoracic aortic wall of SR-BI<sup>-/-</sup> ApoE61<sup>hh</sup> mice aged 1-60 days old (do). Variably sized, intracellular lipid can be observed within endothelial cells (C, E, G-I) and within smooth muscle cells (B, C, H-I) directly beneath the internal elastic lamina (IEL) across all age groups, (yellow asterisks). At 1do, lipid is being engulfed by endothelial cells (A, red asterisks). Within an intercostal ostial ridge, lipid droplets are pictured accumulating within a smooth muscle cell (F, yellow arrow). At 60do, an accumulation of intraendothelial, clustered and variably sized lipid droplets admixed with calcified/mineralized debris (black amorphous material) is indicative of early atherosclerotic lesion formation (J). Scale, 500 nm (A-E and G-J) and 2  $\mu$ m (F).

morphologically consistent with early lipid accumulation by ultrastructure, semi-thin sections stained with Toluidine blue for lipid identification were negative throughout all age groups (histology not shown).

## Discussion

Multiphoton imaging has been widely utilized as a powerful tool in studying the macromolecular microstructure of the extracellular matrix in vascular beds. The use of in situ multiphoton microscopy has many benefits including the elimination of tissue fixation as well as extensive exogenous labeling, and it intrinsically permits generation of isotropic 3D images with image registration. Multiphoton microscopy also permits analysis of the tissue in a near physiological setting, minimizing, but not eliminating, residual strain responses, and the fundamental image is performed with en-face planes providing a unique sectioning presentation. Previous studies have shown that the use of multiphoton microscopy contributes to the reduction of artifacts that can sometimes occur with other imaging modalities (So and Kim 1998; So 2002), including reduced photobleaching and phototoxicity.

Here, we have provided a novel, reproducible, in situ dissection of the mouse VTA that, when coupled with this imaging modality, provides valuable insight in healthy arterial morphology indicative of biochemical extracellular matrix status that can further be applied to diseased arteries. Utilization of this preparation decreases potential distortions by minimizing both dissection and mounting artifacts while closely mimicking several key physiological properties. There have been many different approaches used in preparing vessels for ex vivo microscopy reported in the literature. Some have included mounting variably sized vessel segments into a perfusion chamber (Megens et al. 2007a; Megens et al. 2007b), fresh and/or formalin-fixed tissue preparations mounted between a glass slide and a coverslip (Kwon et al. 2008; Lee et al. 2009; Kim et al. 2010; Lim et al. 2010; Lim et al. 2011; Suhaimi et al. 2012), as well as agar gel-infused vascular casts that are segmented into thinly sliced molds and mounted on a glass slide (van Zandvoort et al. 2004; Megens et al. 2007a; Megens et al. 2008; Le et al. 2010). In vivo approaches have also been described but these are with the addition of mechanical techniques to help minimize motion artifact. Mouse carotid arteries have been imaged in vivo while mounted on an external apparatus for stabilization during anesthesia (Yu et al. 2007). Both mouse carotid arteries and rat renal arteries have also been imaged using TPEF microscopy triggered on cardiac and respiratory signals (Megens et al. 2010) to reduce motion artifact. Although all preparations provide useful information, fewer perturbations to the vascular bed during dissection, together with maintenance of physiological-like longitudinal stretch and

positioning that mimics that observed in vivo, all enhance the in situ relationships of vascular wall matrices. The advantages of this preparation were demonstrated in a cohort of mice aged 1–60do. Findings revealed vessel wall changes associated with a gradual increase in post-natal blood pressure, as previously described (Huang et al. 2005; Le et al. 2012). The undulation within the vessel wall in mice aged 1do and, to a lesser extent, 20do observed using multiphoton microscopy, EM and histopathology, was essentially diminished by 30do, correlating with a rise in blood pressure from approximately 30–70 mmHg from post-natal days 2–35 (Le et al. 2012). These data suggest that, even in the absence of arterial pressure, as imaged in this study, that the remodeling or packing of the individual elastic lamellar units with age was persistent and that the elastic lamellar interconnections with the more rigid collagen fiber bundles increased in mice >30do resulting in tighter packing and less residual strain.

To confirm both the sensitivity and specificity of this preparation for in situ imaging in this longitudinal study, EM and histopathology of the thoracic aortic vascular extracellular matrix were used to validate in situ findings. Both EM and histopathology yielded similar results to multiphoton microscopy regarding the vascular elastic lamellae. Five to six coaxially arranged elastic lamellar layers can be appreciated, with the innermost and outermost layers corresponding to the IEL and EEL, respectively, consistent with results found within the literature (Wolinsky and Glagov 1967; Lee et al. 2005). Collagen fibrils throughout the entire thickness of the vessel wall are best appreciated with multiphoton microscopy, and readily discerned with EM; however, application of picrosirius red for histopathology appeared to be a less sensitive method for the identification of individual collagen fibrils within the tunica media, especially in younger animals. Similarly, Movat's pentachrome showed limited positive collagen staining within the tunica media, but readily elucidated individual elastic lamellar layers. Lipid deposition within the subendothelium and the tunica media was confirmed with EM, but histopathology failed to reveal any lipid deposition at all using well-established techniques, namely, Oil-Red-O and semi-thin frozen sections. Collectively, our data suggests that the multiphoton methodology provided an accurate distribution and structure of the macromolecules in this tissue without fixation or exogenous stains.

An additional benefit from histopathology appreciated in this study was the ability to complete IHC for decorin and biglycan, two members of the SLRP PG family. Both PGs are associated with normal vascular development and vasculopathies, including atherosclerosis, in transgenic mouse models (Williams 2001; Adhikari et al. 2011; Marzoll et al. 2011; Neufeld et al. 2014). The abundance of both PGs observed in this study within the aortic tunica adventitia and, to a lesser extent, the subendothelium and tunica

media, is consistent with previous work completed in murine models (McLean et al. 2005; Adhikari et al. 2011). Furthermore, in IHC sections in which the intercostal ostia were captured (Supplemental Fig. 2C and 2G–2J), strong positive immunoreactivity for both PGs was present within the subendothelium. Given that atherosclerotic lesions in mice often occur at the intercostal ostial bifurcations along the thoracic aorta (McGillicuddy et al. 2001), it is likely that the increased ostial PG deposition observed here in SR-BI KO/ApoE61<sup>hh</sup> mice fed NC will contribute to early lesion development in future atherogenic studies.

Despite the utility of EM and histopathology described here, both imaging modalities have certain limitations in a study such as this. In general, histopathology yields a single, typically 5- $\mu$ m-thick, two-dimensional (2D) slice from tissue embedded in a paraffin block that can take several days to process. Unless numerous serial sections are produced at deeper steps of the submitted sample, the probability of capturing lipid in a similar study would logically be greatly reduced; in this case, throughout all mice aged 1–60d, we did not detect lipid using limited tissue sections stained with Oil-Red-O. EM, an additional 2D imaging modality, yields higher resolution images with greater resolving power than histopathological sections but also requires time-consuming preparation and production of results from approximately 1 mm $\times$ 1 mm submitted tissue samples. Similar to limited sampling in histopathology, EM may reduce the likelihood of lipid identification compared to the methods employed in this study. With the in situ aortic preparation developed here, there is no limitation of scanning a small, embedded section. For example, even though the proximal VTA was the defined region of interest, the entire surface of the VTA could be scanned and easily registered into a 3D image without having to resample the original tissue at a later time, as was accomplished in our preliminary studies (Fig. 2).

In summary, this study characterized the developmental changes observed within the ventral (anterior) surface of the proximal thoracic aorta in SR-BI KO/ApoE61<sup>hh</sup> mice maintained under normal dietary conditions utilizing an in situ preparation for multiphoton microscopy. The physical and structural properties were described and further confirmed, albeit with less sensitivity and specificity, using histopathology and EM. Given the physiological similarities with our model to that observed in vivo, we propose that our approach will provide valuable insight into both healthy and diseased arteries in certain pathological conditions, including aortic atherosclerosis, dissections and aneurysms. Future studies involve the investigation, and potential therapeutic intervention, of early atherosclerotic lesion development in SR-BI KO/ApoE61<sup>hh</sup> mice within the proximal thoracic aorta utilizing the present knowledge gained as a reference that defines normal growth within the aortic vascular bed.

## Acknowledgments

We thank Alan T. Remaley for providing the original transgenic mouse model breeding pairs, Boris L. Vaismen for providing knowledge regarding the maintenance of SR-BI KO/ApoE61<sup>hh</sup> transgenic mice, and Dahae H. Bae for help preparing sections for electron microscopy. This research was completed in partial fulfillment of dissertation work towards a PhD in Comparative Biomedical Sciences at North Carolina State University College of Veterinary Medicine and the NHLBI, through the NIH Graduate Partnership Program.

## Supplementary Material

Supplementary material for this article is available on the *Journal of Histochemistry & Cytochemistry* Web site at <http://jhc.sagepub.com/supplemental>.

## Declaration of Conflicting Interests

The authors declared no potential conflicts of interest with respect to the research, authorship, and/or publication of this article.

## Funding

The authors disclosed receipt of the following financial support for the research, authorship, and/or publication of this article: This research was gratefully supported by the intramural research funds of the NIH and the NHLBI as well as the NIH Comparative Biomedical Scientist Training Program.

## References

- Adhikari N, Carlson M, Lerman B, Hall JL (2011). Changes in expression of proteoglycan core proteins and heparan sulfate enzymes in the developing and adult murine aorta. *J Cardiovasc Trans Res* 4:313–320.
- Dao L, Lucotte B, Glancy B, Chang L-C, Hsu L-Y, Balaban RS (2014). Use of independent component analysis to improve signal-to-noise ratio in multi-probe fluorescence microscopy. *J Microsc* 256(2):133–144.
- de Grauw CJ, Vroom JM, van der Voort HT, Gerritsen HC (1999). Imaging properties in two-photon excitation microscopy and effects of refractive-index mismatch in thick specimens. *Appl Opt* 38:5995–6003.
- Denk W, Strickler JH, Webb WW (1990). Two-photon laser scanning fluorescence microscopy. *Science* 248:73–76.
- Haidari M, Ali M, Gangehei L, Chen M, Zhang W, Cybulsky MI. (2010). Increased oxidative stress in atherosclerosis-prone regions of the mouse aorta. *Life Sci* 87: 100–110.
- Huang Y, Guo X, Kassab GS (2005). Axial nonuniformity of geometric and mechanical properties of mouse aorta is increased during postnatal growth. *Am J Physiol-Heart C* 290:H657–H664.
- Kelleher CM, McLean SE, Mecham RP (2004). Vascular extracellular matrix and aortic development. *Curr Top Dev Biol* 62:153–188.
- Kim S-H, Lee E-S, Lee JY, Lee ES, Lee B-S, Park JE, Moon DW (2010). Multiplex coherent anti-stokes raman spectroscopy imaged intact atheromatous lesions and concomitantly

- identifies distinct chemical profiles of atherosclerotic lipids. *Circ Res* 106:1332-1341.
- Kwon GP, Schroeder JL, Amar MJ, Remaley AT, Balaban RS (2008). Contribution of macromolecular structure to the retention of low-density lipoprotein at arterial branch points. *Circulation* 117:2919-2927.
- Le TT, Duren HM, Slipchenko MN, Hu C-D, Cheng J-X (2010). Label-free quantitative analysis of lipid metabolism in *livin* *Caenorhabditis elegans*. *J Lipid Res* 51:572-677.
- Le VP, Kovacs A, Wagenseil JE (2012). Measuring left ventricular pressure in late embryonic and neonatal mice. *J Vis Exp* 60:1-7.
- Lee JY, Kim S-H, Moon DW, Lee ES (2009). Three-color multiplex CARS for fast imaging and microspectroscopy in the entire CH stretching vibrational region. *Opt Express* 17:22281-22295.
- Lee K, Forudi F, Saidel GM, Penn MS (2005). Alterations in internal elastic lamina permeability as a function of age and anatomical site precede lesion development in apolipoprotein E-null mice. *Circ Res* 97:450-456.
- Lim RS, Kratzer A, Barry NP, Miyazaki-Anzai S, Miyazaki M, Mantulin WW, Levi M, Potma EO, Tromberg BJ (2010). Multimodal CARS microscopy determination of the impact of diet on macrophage infiltration and lipid accumulation on plaque formation in apoE-deficient mice. *J Lipid Res* 51:1729-1737.
- Lim RS, Suhaimi JL, Miyazaki-Anzai S, Miyazaki M, Leci M, Potma EO, Tromberg BJ (2011). Identification of cholesterol crystals in plaques of atherosclerotic mice using hyperspectral CARS imaging. *J Lipid Res* 52:2177-2186.
- Marzoll A, Melchior-Becker A, Cipollone F, Fischer JW (2011). Small leucine-rich proteoglycans in atherosclerotic lesions: novel targets of chronic statin treatment? *J Cell Mol Med* 15:232-243.
- McLean AE, Mecham BH, Kelleher CM, Mariani TJ, Mecham RP (2005). Extracellular matrix gene expression in the developing mouse aorta. *Adv Dev Biol* 15:81-128.
- McGillicuddy CJ, Carrier MJ, Weinberg PD (2001). Distribution of lipid deposits around aortic branches of mice lacking LDL receptors and apolipoprotein E. *Arterioscler Thromb Vasc Biol* 21:1220-1225.
- Megens RTA, oude Egbrink MGA, Cleutjens JPM, Kuijpers MJE, Schiffers PHM, Merx M, Slaaf DW, van Zandvoort MAMJ (2007a). Imaging collagen in intact viable healthy and atherosclerotic arteries using fluorescently labeled CNA35 and two-photon laser scanning microscopy. *Mol Imaging* 6:247-260.
- Megens RTA, oude Egbrink MGA, Merx M, Slaaf DW, van Zandvoort MAMJ (2008). Two-photon microscopy on vital carotid arteries: imaging the relationship between collagen and inflammatory cells in atherosclerotic plaques. *J Biomed Opt* 13:044022-1 - 044022-10.
- Megens RTA, oude Egbrink MGA, Engels W, Leenders PJA, Brunenberg EJJ, Reesink KD, Janssen BJA, Romney BMTH (2010). In vivo high-resolution structural imaging of large arteries in small rodents using two-photon laser scanning microscopy. *J Biomed Opt* 15:011108.
- Megens RTA, Reitsma S, Schiffers PHM, Hilgers RHP, DeMey JGR, Slaaf DW, oude Egbrink MGA, van Zandvoort MAMJ (2007b). Two-photon microscopy of vital murine elastic and muscular arteries. *J Vasc Res* 44:87-98.
- Neufeld EB, Zadrozny LM, Phillips D, Aponte A, Yu Z-X, Balaban RS (2014). Decorin and biglycan retain ldl in disease-prone valvular and aortic subendothelial intimal matrix. *Atherosclerosis* 233:113-121.
- Richards-Kortum R, Sevick-Muraca E (1996). Quantitative optical spectroscopy for tissue diagnosis. *Ann Rev Phys Chem* 47:555-606.
- So PTC (2002). Two-photon fluorescence light microscopy. eLS. Macmillan Publishers Ltd, Nature Publishing Group. www.els.net.
- So PTC, Kim H (1998). Two-photon deep tissue ex vivo imaging of mouse dermal and subcutaneous structures. *Opt Express* 3:339-350.
- Strupler M, Pena AM, Herness M (2007). Second harmonic imaging and scoring of collagen in fibrotic tissues. *Opt Express* 15:4054-4065.
- Suhaimi JL, Chung C-Y, Lilledahl MB, Lim RS, Leci M, Tromberg BJ, Potma EO (2012). Characterization of cholesterol crystals in atherosclerotic plaques using stimulated raman scattering and second-harmonic generation microscopy. *Biophys J* 102:1988-1995.
- Supatto W, Debarre D, Moulia B, Brouzes E, Martin JL, Farge E, Beaurepaire E (2005). In vivo modulation of morphogenetic movements in *Drosophila* embryos with femtosecond laser pulses. *Proc Natl Acad Sci U S A* 102:1047-1052.
- Tangirala RK, Rubin EM, Palinski W (1995). Quantitation of atherosclerosis in murine models: correlation between lesions in the aortic origin and in the entire aorta, and differences in the extent of lesions between sexes in LDL receptor-deficient and apolipoprotein E-deficient mice. *J Lipid Res* 36:2320-2328.
- Van Zandvoort M, Engels W, Douma K, Beckers L, oude Egbrink M, Daemon M, Slaaf DW (2004). Two-photon microscopy for imaging of the (atherosclerotic) vascular wall: A proof of concept study. *J Vasc Res* 41:54-63.
- Wagenseil JE, Mecham RP (2009). Vascular extracellular matrix and arterial mechanics. *Physiol Rev* 89:957-989.
- Williams KJ (2001). Arterial wall chondroitin sulfate proteoglycans: diverse molecules with distinct roles in lipoprotein retention and atherogenesis. *Curr Opin Lipidol* 12:477-487.
- Wolinsky H, Glagov S (1967). A lamellar unit of aortic medial structure and function in mammals. *Circ Res* 20:99-111.
- Yu W, Braz JC, Dutton AM, Prusakov P, Reikhter M (2007). In vivo imaging of atherosclerotic plaques in apolipoprotein E deficient mice using nonlinear microscopy. *J Biomed Opt* 12:054008.
- Yue S, Slipchenko MN, Cheng J (2011). Multimodal nonlinear optical microscopy. *Laser Photonics Rev* 5:496-512.
- Zhang S, Picard M, Vasile E, Zhu Y, Raffai R, Weisgraber K, Krieger M (2005). Diet-induced occlusive coronary atherosclerosis, myocardial infarction, cardiac dysfunction, and premature death in scavenger receptor class B Type I-deficient, hypomorphic apolipoprotein ER61 mice. *Circulation* 111:3457-3464.
- Zipfel WR, Williams RM, Christie R, Nikitin AY, Hyman BT, Webb WW (2003). Live tissue intrinsic emission microscopy using multiphoton-excited native fluorescence and second harmonic generation. *Proc Natl Acad Sci U S A* 100:7075-7080.

**Journal of Histochemistry & Cytochemistry**

JHC Express  
Accepted September 30, 2014  
This article can be cited as DOI: 10.1389/0022155414559590

**Supplemental Material Legends**

Supplemental Image 1. Depicted is the same image panel represented in Figure 3 prior to post image analysis by ICA used for comparison. Note the background signal present in the lipid channel is greater before ICA processing resulting in less signal to noise in unprocessed images. L = lumen; TA = tunica adventitia. Scale bar, 50  $\mu$ m.

Supplemental Image 2. Distribution of proteoglycans decorin (A, C, E, G, and I) and biglycan (B, D, F, H, and J) within the extracellular matrix of proximal thoracic aortas (PTAs) from SR-BI<sup>-/-</sup>/ApoE/R $\delta$ 1<sup>hh</sup> mice aged 1-60do. Notice the prominent positive immunoreactivity (brown chromogen) in the tunica adventitia (TA) and subendothelium (E) for both decorin and biglycan across all age groups. Decorin staining within the tunica media (TM) appears to decrease with age while remaining similar for biglycan. Intercostal anterior ostia (black arrows, C and G-J) exhibit strong immunoreactivity for both decorin and biglycan within the subendothelium. All images are oriented with luminal surfaces at the top and external adventitial surfaces at the bottom of the photomicrographs. Scale bar = 20  $\mu$ m, A-J.

Supplemental avi movies I-X. Avi video clips were produced from a full-thickness z-stack (ranging from ~150-200 $\mu$ m-thick tissue image acquisitions) obtained within the ventral (anterior) surface of the proximal thoracic aorta of representative SR-BI<sup>-/-</sup>/ApoE/R $\delta$ 1<sup>hh</sup> mice aged 1 (movies I-II), 10 (movies III-IV), 20 (movies V-VI), 30 (movies VII-VIII) and 60 (movies IX-X) days old. En-face projections coupled with cross sections followed by a maximum projection, three-dimensional rendering for each age group are provided. Collagen second harmonic generation (SHG) is green, elastin auto-fluorescence is red and Nile red (NR) lipid droplet fluorescence is blue. Image acquisition was optimized during all experiments to fill the digitizer. ICA was

**Journal of Histochemistry & Cytochemistry**

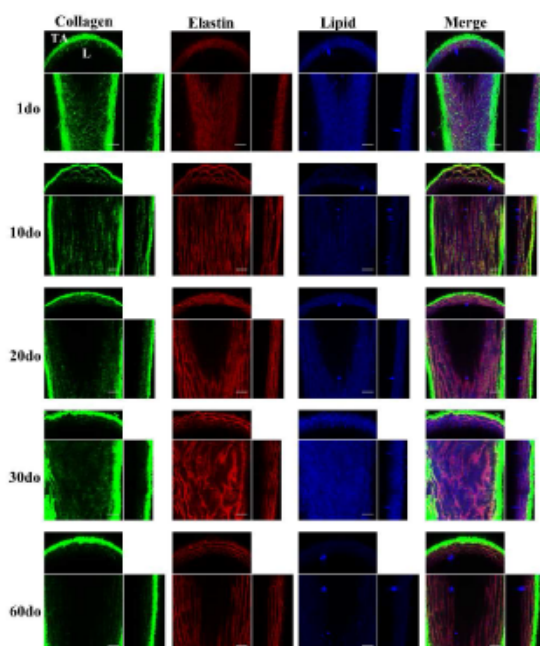
JHC Express  
Accepted September 30, 2014  
This article can be cited as DOI: 10.1389/0022155414559590

applied during post image processing and the elastin fluorescence signal was optimized across all age groups for comparison purposes.

Supplemental avi movies XI-XII. Avi video clips produced from a full-thickness *z*-stack obtained within the ventral (anterior) surface of the proximal thoracic aorta of a 3-month old SR-*BI<sup>-/-</sup>/ApoE<sup>R01</sup><sup>hh</sup>* mouse. Collagen second harmonic generation (SHG) is green, elastin auto-fluorescence and Syto® 24 fluorescent nucleic acid stain are both red, and Nile red (NR) lipid droplet fluorescence is blue. Note that the wide emission spectra of Syto® 24 (~475-600 nm) when excited with an 820 nm wavelength essentially masks any lipid labelled with NR. En-face projections (movie XI) and a merged cross section (movie XII) are supplied. ICA was applied during post image processing. These movies provide confirmation of complete penetration of the vessel wall by a fluorescent nuclear dye in this in-situ mouse thoracic aorta preparation.

Supplemental avi movies XIII-XIV. Avi video clips produced from a full-thickness *z*-stack obtained within the ventral (anterior) surface of the proximal thoracic aorta of a 3-month old SR-*BI<sup>-/-</sup>/ApoE<sup>R01</sup><sup>hh</sup>* mouse. Collagen second harmonic generation (SHG) is green, elastin auto-fluorescence is red, and the vascular endothelium (di-8-ANEPPS) and phospholipid bilayers (di-8-ANEPPS) are blue. En-face projections (movie XIII) and a merged cross section (movie XIV) are supplied. ICA was applied during post image processing. Unlike lipid stained as solid spheres as observed with NR, lipid stained with di-8-ANEPPS appears as black hollow spheres with phospholipid bilayers outlined in blue. Lipid is appreciated resting on the stained vascular endothelium (blue) indicating that the lipid droplets within this *z*-stack are likely captured on the vascular luminal surface directly on the endothelium and within the endothelial cell cytoplasm.

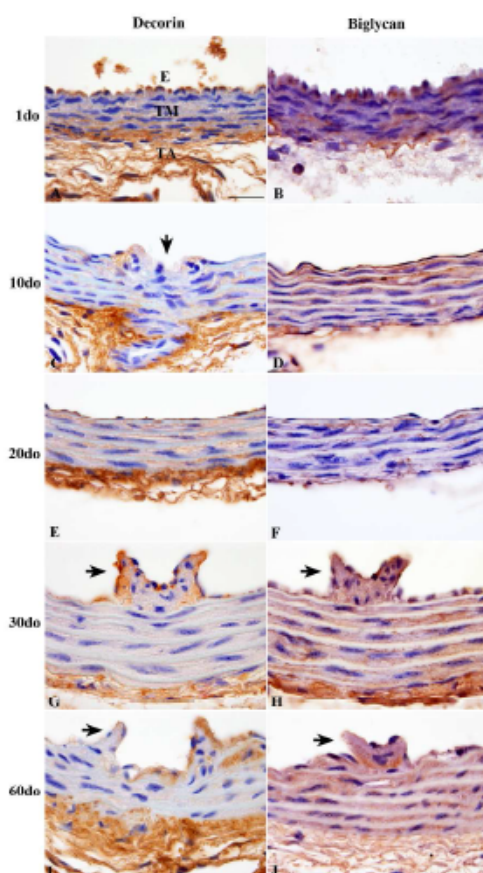
JHC Express  
Accepted September 30, 2014  
This article can be cited as DOI: 10.1389/0022155414559590



Supplemental image 1. Depicted is the same image panel represented in Figure 3 prior to post image analysis by ICA used for comparison. Note the background signal present in the lipid channel is greater before ICA processing resulting in less signal to noise in unprocessed images. L = lumen; TA = tunica adventitia. Scale bar, 50 $\mu$ m.  
279x361mm (300 x 300 DPI)

## Journal of Histochemistry &amp; Cytochemistry

JHC Express  
 Accepted September 30, 2014  
 This article can be cited as DOI: 10.1369/0022155414559590



Supplemental Image 2. Distribution of proteoglycans decorin (A, C, E, G, and I) and biglycan (B, D, F, H, and J) within the extracellular matrix of proximal thoracic aortas (PTAs) from SR-BI<sup>-/-</sup>/ApoeR61h/h mice aged 1-60do. Notice the prominent positive immunoreactivity (brown chromogen) in the tunica adventitia (TA) and subendothelium (E) for both decorin and biglycan across all age groups. Decorin staining within the tunica media (TM) appears to decrease with age while remaining similar for biglycan. Intercostal anterior ostia (black arrows, C and G-J) exhibit strong immunoreactivity for both decorin and biglycan within the subendothelium. All images are oriented with luminal surfaces at the top and external adventitial surfaces at the bottom of the photomicrographs. Scale bar = 20  $\mu$ m, A-J.

215x279mm (300 x 300 DPI)

## Chapter 3

Early Three-dimensional Atherosclerotic Lesion Development in Scavenger Receptor Class  
B Type I-Deficient, Hypomorphic Apolipoprotein ER61 Mice and the Association with  
Endothelial and Smooth Muscle Cell Damage

Abstract:

*Background:* All phases of atherosclerosis have been shown to develop throughout the arterial tree in ApoE-deficient mice, from fatty streaks, to advanced fibrous plaques. In the present study, we investigated early lesion development within the descending thoracic aorta in the recently described, SR-BI KO/ApoER61<sup>h/h</sup> mouse model of diet-inducible atherosclerosis.

*Methods and Results:* To evaluate early lesion development in SR-BI KO/ApoER61<sup>h/h</sup> mice, 2-3 month old mice were placed on a HFHC diet for 21 days. Animals were euthanized daily from 0-5 days and then at 14 and 21 days. Prior to euthanasia, Sytox Blue, a nucleic acid stain that penetrates cells with compromised plasma membranes, was injected into the jugular vein. *In situ* imaging of the descending TA and ICAO was performed using TPEF, SFG and CARS microscopy. Briefly, Sytox Blue positive SMCs were consistently located transmurally within the proximal descending aorta, multifocally and circumferentially throughout the intercostal ostial ridges, and interestingly, several pairs of intercostal ostia exhibited a cluster of mural to transmural Sytox Blue positive SMCs downstream between bilateral pairs of intercostal ostia. Lipid droplets, foam cells and early ICAO plaques often colocalized with Sytox Blue positive cells in all regions but

often spared the vascular bed between bilateral intercostal ostia. Sytox Blue positive ECs were present within the intercostal ostial ridges colocalized with lipid.

Conclusions: These findings suggest that endothelial and smooth muscle cell damage within these marginal zones downstream to the ICAO may contribute to retention of LDL as propagation of early lesion development prior to fatty streak formation.

Introduction:

Coronary artery disease (CAD) resulting from atherosclerosis is a leading cause of death worldwide (Weber et al., 2011). The pathogenesis is multifactorial for which a persistent increase in systemically circulating LDL levels (Jamkhande et al., 2013) is considered to be one of the most important causes for disease initiation and progression. Immune and inflammatory mediators (Cullen et al., 2005. Ribbins et al., 2006) along with hemodynamic shear stress (Peiffer et al., 2013, Suo et al., 2006) endothelial cell damage and focal proliferations of SMCs (Velican et al., 1989) also represent key mechanisms of disease. Furthermore, repeated endothelial injury coupled with enhanced lipid infiltration are considered critical events regarding the development of atherosclerosis (Lin, 1996).

It is widely believed that the fatty streak, which can be found in infants and small children (Thubrikar et al., 2007), is considered the earliest visibly detectable lesion of atherosclerosis (Fuster et al., 1996). These fatty streaks typically occur in the regions of branches and bifurcations. Many are considered to be the same as intimal cushions, composed almost exclusively of lipid-containing SMCs, most of which don't progress into advanced plaques, thus offering the opinion that fatty streaks are normal and not pathologic (Glacov et al., 1996). Progress has been made in understanding the current initiating hypotheses through utilization of transgenic mouse models of atherosclerosis;

specifically those in which the genes for apolipoproteins and/or their enzymes, transfer proteins, as well as receptors that contribute to LP metabolism have been inactivated or manipulated in some manner (Zhang et al., 2005). The SR-BI KO/ApoER61<sup>h/h</sup> diet inducible mouse model of atherosclerosis used in the present study exhibits total cholesterol levels that significantly exceed the normal reference values of 80-100 mg/dL (Zhang et al., 2005) when fed a NC diet. This mouse model lacks SR-BI, which is responsible for reverse cholesterol transport out of the vessel wall into the liver where it is transported into the gall bladder and excreted from the body via the intestinal tract. Despite significant hypercholesterolemia, these mice can survive on a NC diet into adulthood as the low expression level of apolipoprotein ER61 is considered to be both atheroprotective and cardioprotective (Raffi et al., 2002. Raffi et al., 2001). However, when fed a HFHC diet, these mice rapidly develop atherosclerosis and coronary heart disease independent of sex and age (Zhang et al., 2005) over the course of 1 month.

Several different imaging modalities have been used in evaluating atherosclerotic processes including magnetic resonance imaging (MRI), light microscopy, transmission and scanning electron microscopy. NLOM has emerged as a powerful tool for label-free tissue imaging (Mostaco-Guidolin et al., 2011. Zipfel et al., 2003) allowing for deeper tissue penetration and the 3D visualization of key tissue components and biochemical composition at a submicron resolution (Lim et al., 2010). Moreover, when implementing a multimodal platform, selective imaging of collagen, elastin and lipids is achieved by SHG or SFG, TPEF, and CARS respectively. Furthermore, CARS signals arising from CH<sub>2</sub>-rich membranes also allows for visualization of endothelial cells and smooth muscle cells within the vessel wall (Wang et al., 2008). Vibrational imaging of elastin and collagen fibrils is also accomplished with CARS as these macromolecules are rich in CH<sub>2</sub>

bonds.

We have previously established a novel *in situ* preparation of the mouse TA to demonstrate the developing ventral (anterior) surface of the vascular bed using TPEF, SHG, and the exogenous lipophilic fluorescent probe NR. Although any strain of mouse could have been used, we reasoned that using the SR-BI KO/ApoER61<sup>h/h</sup> diet inducible mouse model of atherosclerosis (Zadrozny et al., 2015) maintained under normal dietary conditions would be appropriate in preparations for future studies in atherosclerosis. Using the same mouse strain maintained on a HFHC diet, the current study offers additional insight; specifically into the intercostal arterial ostial involvement in the development of early atherosclerosis through modification of the original *in situ* aortic preparation coupled with a multimodal nonlinear optical microscopy platform.

The same approach used to expose the ventral (anterior) surface of the mouse thoracic aorta (VTA) was applied with the addition of longitudinal transection of the VTA to expose the dorsal (posterior) surface of the TA and the ICAO. The purpose of this study was to evaluate how early lesions develop within and surrounding mouse thoracic ICAO in relationship to the 3D macromolecular structure of the vascular bed. Additionally, the association of damaged cells, including both ECs and SMCs in regions of high endothelial cell turnover was tracked over time. These regions, including major aortic branch points, are characterized by hemodynamic conditions that induce altered WSS (Suo et al., 2007) and oscillatory flow (Foteinos et al., 2008). We sought to evaluate the resultant changes in the vascular bed within these initiating sites including endothelial and smooth muscle cell integrity, lipid deposition and potential perturbations of the macromolecular matrix. Cellular changes were assessed using Sytox Blue nucleic acid stain, a high-affinity molecular probe that easily penetrates cells with compromised

plasma membranes yet will not cross the membranes of live cells. Elastin and collagen were imaged by TPEF and SFG respectively and lipid deposition by CARS.

## Materials and Methods

### *Animals:*

SR-BI KO/ApoER61<sup>h/h</sup> mice obtained from Dr. Alan Remaley at the NHLBI in Bethesda, MD, were bred, as previously described (Zhang et al. 2005). C57Bl/6 control mice were obtained from Jackson Laboratory (Bar Harbor, ME, USA). C57Bl/6 mice and SR-BI KO/ApoER61<sup>h/h</sup> mice were fed a NC diet (18% protein, 4% fat, 5% fiber, Zeigler Feed, NIH-31 open formula) or a HFHC diet (21% milk fat, 21.2% fat, 1.25% cholesterol, TD 96121, Harlan-Teklad) as indicated. All experiments on animals were performed according to the research protocol (H-0257) approved by the Animal Care and Use Committee of the NHLBI at the NIH.

### *Mouse Thoracic Aorta Preparation for Multimodal Nonlinear Optical Microscopy:*

DTAs were dissected within male and female mice aged 2 to 3 months old. C57Bl/6 control mice (n=3) and SR-BI KO/ApoER61<sup>h/h</sup> control mice (n=3) were fed NC. SR-BI KO/ApoER61<sup>h/h</sup> experimental mice were fed a HFHC diet for 21 days and euthanized at daily intervals from days 0 to 5 (n=3/group), then at days 14 and 21(n=3/group). Mice were placed in an anesthesia box for induction and then ventilated by a nose cone with a mixture of 2.5% isoflurane in oxygen. Prior to euthanasia, all mice were given an intravascular injection into the jugular vein containing Sytox Blue (250 $\mu$ M in 100 $\mu$ L of sterile saline, Life Technologies; Invitrogen; Grand Island, NY) to systemically label permeabilized cells. Mice were euthanized 10 minutes thereafter via a double thoracotomy and VTAs were dissected *in situ* as previously described (Zadrozny et al., 2015) with an additional modification to expose the ICAO. VTAs were transected

longitudinally along the midline from the aortic root to the aortic hiatus and splayed open to display the luminal surface of the dorsal TA and the associated ICAO. *In situ* preparations were pinned in place with insect specimen mounting pins (Fine Science Tools; Foster City, CA) onto 20% agar gel platforms and submerged in saline for imaging.

*Multimodal Nonlinear Optical Microscopy:*

*In situ*, multiphoton images of the dorsal TA were acquired from the luminal surface out to the dorsal aortic tunica adventitia. A dual beam mode-locked ultrafast laser (Insight DeepSee, Spectra-Physics, Santa Clara, California) generated a wavelength tunable pump beam and a fixed wavelength Stokes beam at 1040 nm. The pump beam was tuned to 802 nm such that the corresponding Raman shift of  $2853\text{ cm}^{-1}$  between the two beams was located at the  $\text{CH}_2$  symmetric stretch vibration band (Evans et al., 2005; Le et al., 2007; Hellerer et al., 2007). The two beams were combined via a custom dichroic mirror with a cutoff wavelength at 1020 nm and directed to a confocal SP8 upright microscope (Leica Microsystems, Wetzlar, Germany). The delay between the two pulses was adjusted with a delay stage to maximize the CARS signal from lipid droplets at  $2853\text{ cm}^{-1}$ . The beams were focused by a 25x water immersion objective with a 1.0 numerical aperture (NA) (PL IRAPO 25x/1.0 motCorr, Leica Microsystems, Wetzlar, Germany). A critical feature of this objective for CARS imaging was its chromatic aberration correction between 700 nm and 1300 nm which allows parfocality between the pump and Stokes beams focal spots. The motorized collar for spherical aberration correction was adjusted to maximize the lipid CARS signal integrated over the entire 3D volume. The emitted light was detected by the same objective, separated from the excitation light by a primary dichroic mirror (FF735-Di01, Semrock, Rochester, New York), and directed to four non-descanned detectors. A second dichroic mirror

(FF526-Di01, Semrock, Rochester, New York) then splits the light between a pair of hybrid detectors (HyD) and a pair of PMTs (Leica microsystems, Wetzlar, Germany). The light directed to the two HyD was filtered by two infra-red (IR) blocking filters (FF01-7220/SP and FF01-790/SP, Semrock, Rochester, New York), split by a dichroic mirror (FF640-FDi01, Semrock, Rochester, New York) that separated the lipid CARS signal at 653 nm from the autofluorescence elastin signal and are detected after bandpass filtering (FF01-650/13 and FF01-578/105, Semrock, Rochester, New York). The light directed to the two PMTs is filtered by an IR blocking filter (FF01-680/SP, Semrock, Rochester, New York), split by a dichroic mirror (FF484-FDi01, Semrock, Rochester, New York) that separated the sum frequency generation (SFG) signal at 453 nm from the Sytox blue fluorescence signal, and is finally bandpass filtered (FF01-494/41 and FF01-448/20, Semrock, Rochester, New York) before detection. Note that there is cross-talk between the SFG, sytox blue and elastin channels.

The pump and Stokes beams have a pulse width of 110 fs and 280 femtoseconds (fs) respectively. The dispersion occurring in the optical path of the pump beam is pre-compensated in the Insight DeepSee and is therefore transform limited to 110 fs at the focal plane. The dispersion in the Stokes beam is not compensated for and its pulse width is therefore expected to be slightly broadened. The spectral resolution of the fs-CARS system is approximately  $140 \text{ cm}^{-1}$  and is an order of magnitude larger than the  $\text{CH}_2$  stretch Raman line width,  $10 \text{ cm}^{-1}$  (Cheng et al., 2004). As a result the resonant to non-resonant background ratio obtained with fs-CARS imaging of lipids is lower than that with ps pulses (Cheng et al., 2004). We measured this ratio to be 3.6 in a mouse aorta with fs-CARS and found it to be sufficient for a straightforward identification of lipid droplets in

the arterial wall. However, the use of fs pulses greatly benefits the two-photon emission fluorescence (TPEF) and second harmonic signals, which increase linearly with shorter pulse widths, and allows recording the TPEF, second harmonic and CARS signals simultaneously. For CARS the use of fs pulses also leads to an increased signal amplitude which partly offsets the drop in resonant to non-resonant background ratio.

Three-dimensional images from each PMT and HyD channels at 512x512 or 2048x2048 pixels with a frame rate of 600-700 Hz, an optical zoom range of 0.75-2.25 and a step section of 1  $\mu\text{m}$  were collected as a stack of images beginning at the luminal surface and ending at the dorsal tunica adventitia. Collagen SFG was detected at 438-458 nm (PMT 1), Sytox Blue fluorescence at 474-514 nm (PMT 2), elastin fluorescence at 525-630 nm (HyD 1), and CARS lipid signal at 843-656 nm (HyD 2). Images were analyzed using ImageJ (NIH; Bethesda, MD). CARS arterial wall imaging: (Wang et al., 2008; Wang et al., 2009)

Results:

The 3D macromolecular structure of the vascular bed in SR-BI KO/ApoER61<sup>h/h</sup> mice fed a HFHC diet for 21 days was evaluated along the entirety of the dorsal surface of the descending thoracic aorta with a focus on the ICAO and the space between pairs of intercostal arteries. Full thickness z-stacks commencing at the luminal surface and ending at the dorsal adventitial surface were obtained from at least 3 ICAO for each mouse for post-image processing and 3D rendering. Either individual or bilateral pairs of ICAO were captured dependent upon their proximity within an individual field of view. All multiphoton images are depicted with the head and tail ends of the mice at the top and bottom of each image respectively.

The bright red CARS lipid signal should be discerned from the dim red background

generated from epi-detection and the additional CH<sub>2</sub> bonds resonating within elastin, endothelial, and smooth muscle cells (Wang et al., 2008). This phenomenon is best appreciated in cross sections both above the luminal surface and within *en face* sections within the tunicas intima and media (see white asterisks in Figs. 1A and 1B describing this issue).

Collagen was visualized using SFG via epi-detection through a CARS signal that was forward generated and backscattered. Fibrillar adventitial collagen was prominent while minimal signal was appreciated murally throughout all experimental and control groups (Figs. 3.1-3.8).

Elastin formed dense, wavy lamellar sheets with variably sized fenestra and folds throughout the length of the dorsal TA, a loss of signal circumferentially (Fig. 3.1-3.8) on the raised ostial ridges, and increased disorganization at the base of the ridges (Fig 3.3-3.8). The latter occurred in experimental mice fed a HFHC diet exhibiting moderate to marked ostial lipid deposition. Lipid, both extracellular in droplet form and intracellular (foam cells) within SMCs, macrophages and ECs based on cellular morphology was appreciated multifocally throughout the entirety of the dorsal TA. Foam cells were already apparent in mice prior to feeding a HFHC diet (images not shown) and were characterized by central to compressed nuclei that did not emit a signal appearing black in color with a myriad of bright red, pinpoint, intracytoplasmic lipid droplets best shown in Fig. 3.3A and Fig. 3.7A (white arrows). Lipid droplets and foam cells initially accumulated on the endothelium above an intact IEL surrounding ICAO and between pairs of ICAO. There was noticeable increased abundance of lipid depositing circumferentially on the endothelium surrounding ICAO in mice fed a HFHC diet from days 1-5 (Figs 3.3-3.5),

which advanced to intraostial lipid accumulation in mice fed a HFHC diet for 14 (Fig. 3.6) and 21 days (Figs. 3.7-3.8). Loss of the normal ostial ridge architecture occurred as the mice progressed to 14 and 21 days (Fig. 3.8) on a HFHC diet where the actual ridges became less discernable from early lesion development. Extravasation of lipid through the tunica media was observed in 2 month old, SR-BI KO/ApoER61<sup>h/h</sup> control mice fed NC (Fig. 3.2) and in experimental mice throughout the entire study with increased frequency immediately surrounding ICAO. Minimal accumulation or extravasation was appreciated within the vessel wall of C57BL/6T control mice fed NC.

Endothelial cell (plump, round to oval cellular morphology) and SMC (elongate spindleoid cellular morphology) death, as indicated by Sytox Blue positively stained cells, revealed a fairly consistent pattern across all SR-BI KO/ApoER61<sup>h/h</sup> mice in this study. Variably sized clusters of transmurally permeabilized SMCs were often found downstream (Fig 3.3., HFHC diet for 1 day; Fig. 3.5 HFHC diet for 5 days; Fig. 3.6., HFHC diet for 14 days) and between pairs of ICAO (Fig. 3.2., day 0, NC fed control mouse) that were typically not associated with lipid deposition or foam cell accumulation. Co-localization of lipid and permeabilized SMCs was not appreciated until SR-BI KO/ApoER61<sup>h/h</sup> mice had been maintained on a HFHC diet for 21 days (Fig. 3.7). Less often, variably sized patches of permeabilized SMCs were found immediately upstream of the ICAO (Fig. 3.2, day 0 NC fed control mouse; Fig. 3.7, day 21 HFHC). Positive ECs along with fragmented nuclear debris were often found colocalized with lipid circumferentially on the intercostal ostial ridges in all SR-BI KO/ApoER61<sup>h/h</sup> experimental mice (Figs. 3.2-3.8). In C57BL/6T control mice fed NC (Fig. 3.1), positive ECs multifocally decorated intercostal ostial ridges and occasionally were found individually scattered throughout the vascular

bed. However, similar to the patches of positive SMCs found transmurally downstream and between ostia in SR-BI KO/ApoER61<sup>h/h</sup> experimental mice fed HFHC up to 14 days, colocalization with lipid was not observed. Occasional foam cells were permeabilized by Sytox Blue exhibiting positively stained nuclei surrounded by intracytoplasmic lipid droplets (image not shown) in experimental mice fed a HFHC diet.

#### Discussion:

Multimodal Nonlinear optical microscopy, including CARS, TPEF, SHG and SFG has been widely used in analyzing the vascular bed to describe the macromolecular events that occur in atherosclerotic lesion development and progression (Wang et al., 2008; Lim et al., 2010; Cicchi et al., 2014). However, *in situ* vascular preparations of the TA and major branch points, specifically at the ostial openings, have not been well described with this imaging platform. We have previously developed a novel, reproducible, *in situ* vascular preparation to study the development of the patent mouse TA in the SR-BI KO/ApoER61<sup>h/h</sup> diet-inducible model of atherosclerosis (Zhang et al., 2005; Zadrozny et al., 2015). This study evaluated the macromolecular events that occurred within the ventral (anterior) surface of the TA in SR-BI KO/ApoER61<sup>h/h</sup> mice aged 1-60 days old (do) in preparation for future studies to evaluate lipid deposition and early atherosclerosis. We sought to use this transgenic mouse model in contrast to other models as it the only model that has been thoroughly characterized to recapitulate hallmarks of human cardiovascular disease including occlusive coronary artery disease with plaque rupture, myocardial infarction, cardiac dysfunction and premature death (Caligiuri et al., 1999; Moriwaki et al., 2004; Cozen et al. 2004).

Here, we have expanded upon this vascular dissection of the TA to develop a window into the dorsal (posterior) surface by transecting the aorta longitudinally to reveal the ICAO. This allowed for *en face, in situ* evaluation of the descending TA and associated ICAO as the depth of penetration in a patent TA is limited to the wall thickness of the ventral surface alone (Zadrozny et al., 2015). Minimal perturbations made with this 3D *in situ* approach allowed for imaging that greatly maximized the field of view of the ICAO and surrounding vascular bed. This is in contrast to preparing *ex vivo*, fresh and/or formalin-fixed vascular dissections to evaluate ostial morphology that are mounted between a glass slide and a coverslip (Ferrara et al., 2005; Kwon et al., 2008; Lee et al., 2009; Kim et al., 2010; Lime et al., 2010; Lim et al., 2011; Suhalim et al., 2012). It's also important to note that traditional imaging modalities such as histopathology and EM would not have yielded the same results as they are both 2 dimensional (2D) slices of tissue 2-5  $\mu\text{m}$  thick fixed sections. Without extreme efforts, reconstructions of full-thickness aortic z-stacks with these modalities aren't feasible.

The exogenous, IV injection with Sytox Blue to evaluate cell death and potentially cell turnover for both endothelial and smooth muscle cells (based on their cell morphology) resulted in an interesting and consistent pattern. Given that we were able to image such a large field of view for 3D reconstruction we were able to consistently visualize positive ECs that were found within and surrounding intersostal ostial ridges as well as positive SMCs located downstream and transmurally between bilateral pairs of ICAO. Less often, variably sized patches of positive SMCs were also found immediately upstream of the ICAO, but there was no correlation with diet as this was appreciated in both NC and HFHC fed SR-BI KO/ApoER61<sup>h/h</sup> mice. To the best

of our knowledge, these findings have not been reported using the imaging and vascular dissection approach described herein. Further investigation of positive stained ECs and SMCs elucidated additional insight in that positive cells found on the intercostal ostial ridges of C57BL/6T control mice fed NC were present in the absence of lipid deposition (Fig. 3.1). Similarly, the patches of positive SMCs identified transmurally downstream did not colocalize with lipid until SR-BI KO/ApoER61<sup>h/h</sup> mice were fed HFHC for 21 days. This suggests that these regions may develop prior to foam cell deposition and fatty streak formation, the earliest visibly detectable lesions of atherosclerosis (Thubrikar, 2007).

Given the multifactorial pathogenesis of atherosclerosis, there is likely a combination of initiating events to help describe these findings. It is in our opinion these events are primarily associated with endothelial cell turnover, proliferation and death, as well as altered hemodynamic wall shear stress (WSS) described as follows.

Leaky cellular endothelial junctions occurring in dying cells have been postulated as a pathway for macromolecular transport across the endothelium (Welbaum et al., 1985; Lin et al., 1990). Rapid EC turnover in atherosclerotic-prone areas to replace dead cells also results in disruption of cellular junctional complexes within the endothelium (Lin et al., 1988; Lin et al., 1989). Furthermore, risk factors associated with atherosclerosis and CHD, including hyperlipidemia as described in SR-BI KO/ApoER61<sup>h/h</sup> mice fed normal chow (Zhang et al., 2005), have been shown to increase arterial EC turnover and transendothelial macromolecular transport (Lin et al., 1996). Hemodynamic shear stress has often been implicated in early lesion development and progression. Specifically, regions exhibiting low WSS, oscillatory stress, and flow

separation (Nguyen and Haque, 1990; Ku, 1997; Taylor et al., 1998; Wootton and Ku, 1999; Neufeld et al., 2010) at arterial branch points are strongly correlated with lesion development. Within these regions of low WSS, it has previously been shown that the aortic intima exhibits increased levels of leukocyte inflammatory mediators, vascular cell adhesion molecule-1 (VCAM-1) and intercellular adhesion molecule-1 (ICAM-1) (Suo et al., 2007). Inflammatory cytokines and modified lipids that are released from oxidized lipoproteins found beneath the endothelium, and within plaques, drastically changes endothelial and smooth muscle cell phenotype resulting in cell activation and increased mitosis (Robbins and Cotran, Jongstra-Bilen et al., 2010). In short, SMC and EC damage in the absence of foam cell and lipid deposition may precede fatty streak development largely contributing to early lesion development in atherosclerosis in regions of low wall shear stress and oscillatory flow.

The current findings in this study warrant future investigations into gene expression and endothelial integrity. This modified *in-situ* vascular dissection can be used to determine if there is a potential up- or down regulation of inflammatory cytokines and adhesion molecules, and to further evaluate endothelial integrity within regions of Sytox Blue positive cells in both healthy and diseased mice over time. An additional study should include further evaluation of these permeabilized cells in an effort to determine novel biomarkers contributing to early atherosclerotic lesion development, perhaps even prior to the fatty streak, as a target for therapeutic intervention.

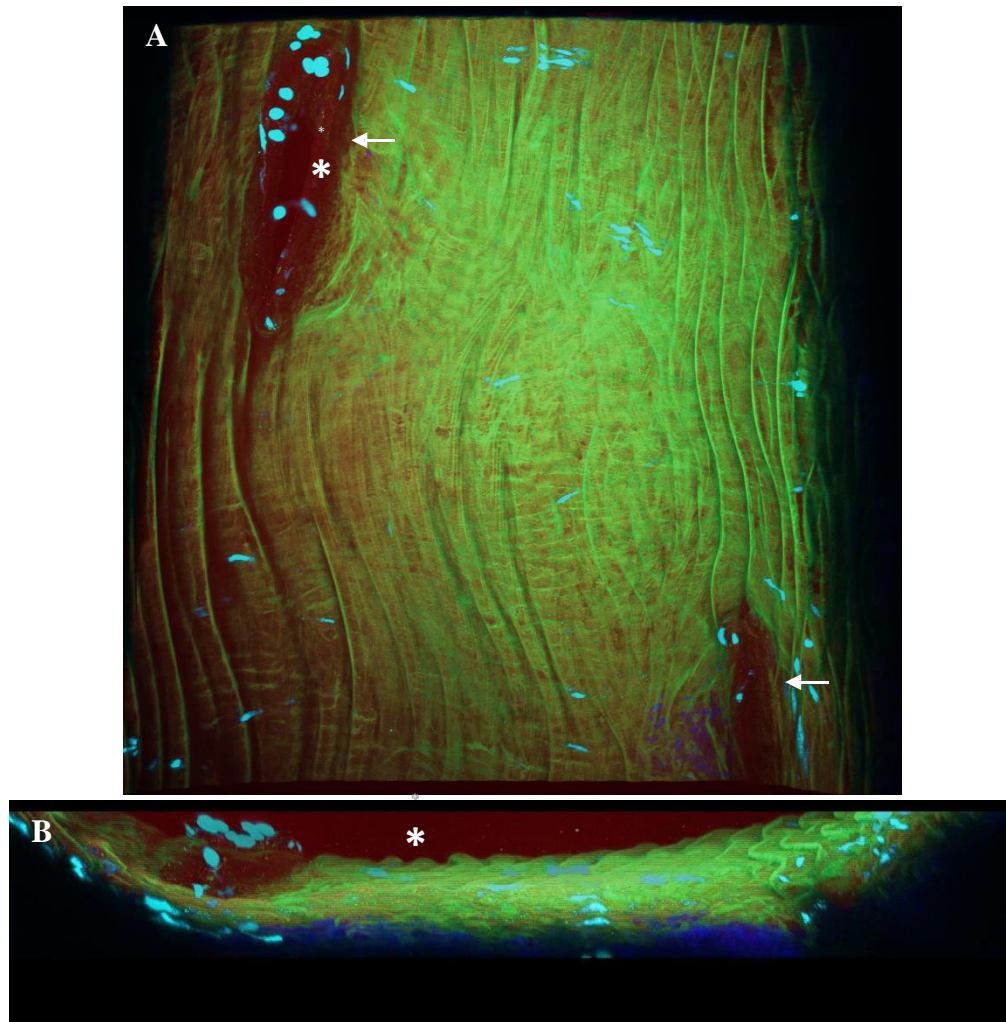


**Figure 3.1:** Multimodal nonlinear optical microscopy three-dimensional (3D) *in situ* images from the thoracic aorta with bilateral intercostal ostia from a 2 month old C57BL/6T control mouse fed NC. Elastin (green), collagen (blue), permeabilized (damaged) Sytox blue positive cells (cyan) and lipid (red) signals are merged after post-image processing. The dim red background signal exhibited above the luminal surface (white asterisk) and within the intercostal ostia (white asterisk) should be discerned from the bright red, punctate to clustered lipid droplets as observed in Figures 2-8. (A) *En face* image. Note the presence of damaged cells circumferentially surrounding the ostia (white arrows) in the absence of lipid deposition. (B) Representative cross section with minimal positive Sytox blue staining transmurally. (Images were obtained with a Leica 25x1.0 NA water immersion objective lens.

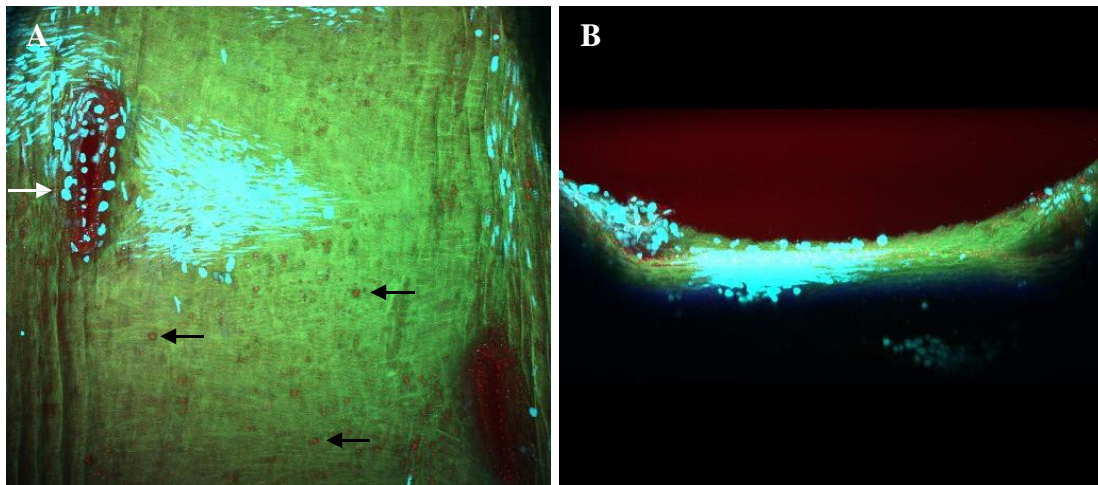


**Figure 3.2:** Multimodal nonlinear optical microscopy three-dimensional (3D) *in situ* images from the thoracic aorta with bilateral intercostal ostia from a 2 month old SR-BI KO/ApoER61<sup>h/h</sup> control mouse fed NC (day 0). Elastin (green), collagen (blue), permeabilized (damaged) Sytox blue positive cells (cyan) and lipid (red) signals are merged after post-image processing. (A) *En face* image. Note the extensive cluster of damaged spindeloid cells indicative of smooth muscle cell morphology downstream to the left intercostal ostium in the absence of lipid deposition. Similar to the C57BL/6T control mouse in Figure 1, Sytox blue positive cells surround the left intercostal ostium (plump endothelial cells, white arrow) but with the addition of lipid droplets on the ostial ridge. Moderate numbers of individualized lipid droplets are also appreciated multifocally on the luminal surface (A, black arrows) (B) Representative cross section showing transmurally damaged smooth muscle cells and endothelial cells between and within intercostal ostia respectively. (Images were obtained with a Leica 25x1.0 NA water immersion objective lens.

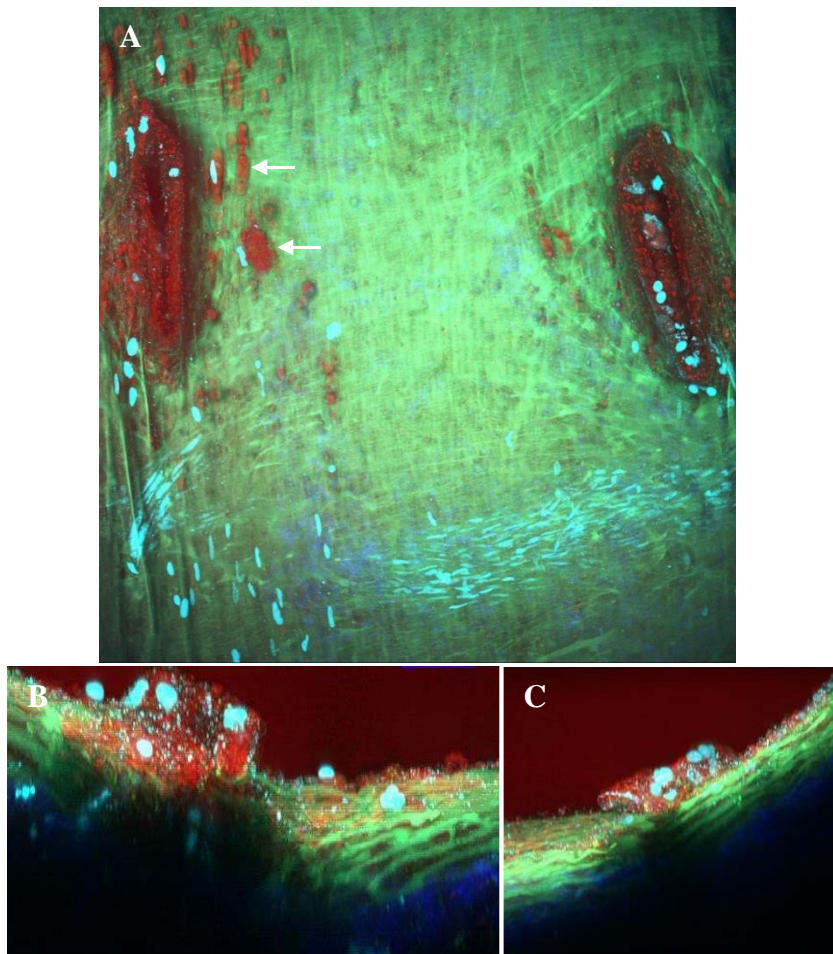


**Figure 3.3:** Multimodal nonlinear optical microscopy three-dimensional (3D) *in situ* images from the thoracic aorta with bilateral intercostal ostia from a 2 month old SR-BI KO/ApoER61<sup>h/h</sup> mouse fed HFHC for 1 day. Elastin (green), collagen (blue), permeabilized (damaged) Sytox blue positive cells (cyan) and lipid (red) signals are merged after post-image processing. (A) *En face* image. Bilateral intercostal ostia exhibit extensive, extra- and intracellular (foam cells, white arrow) circumferential lipid deposition colocalized with Sytox blue positive. Downstream, transmurally Sytox blue positive spindle cells (smooth muscle cells) are also present. (B and C) Representative cross sections of the left and right intercostal ostia respectively showing mural lipid deposition colocalized with Sytox blue positive cells. (Images were obtained with a Leica 25x1.0 NA water immersion objective lens.

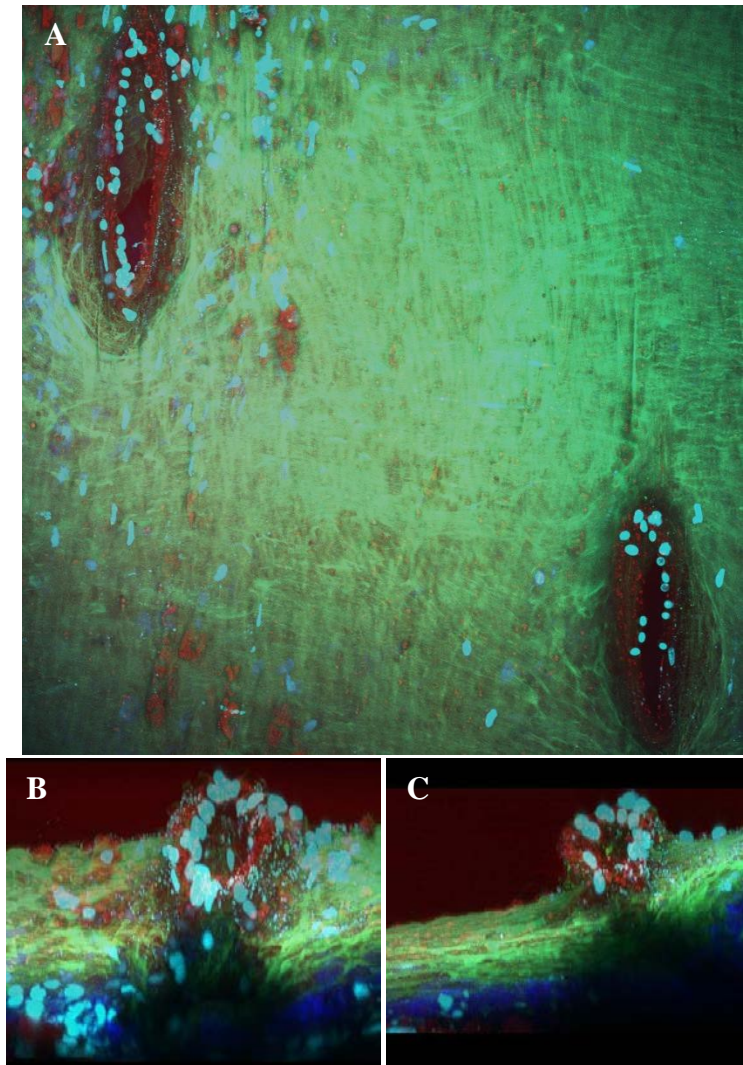


**Figure 3.4:** Multimodal nonlinear optical microscopy three-dimensional (3D) *in situ* images from the thoracic aorta with bilateral intercostal ostia from a 2 month old SR-BI KO/ApoER61<sup>h/h</sup> mouse fed HFHC for 3 days. Elastin (green), collagen (blue), permeabilized (damaged) Sytox blue positive cells (cyan) and lipid (red) signals are merged after post-image processing. (A) *En face* image appears similar to mice fed HFHC for 3 days (Figure 3) less the cluster of positive Sytox blue smooth muscle cells distal to and between this pair of intercostal ostia. (B and C) Representative cross sections of the left and right intercostal ostia respectively showing mural lipid deposition colocalized with Sytox blue positive cells. (Images were obtained with a Leica 25x1.0 NA water

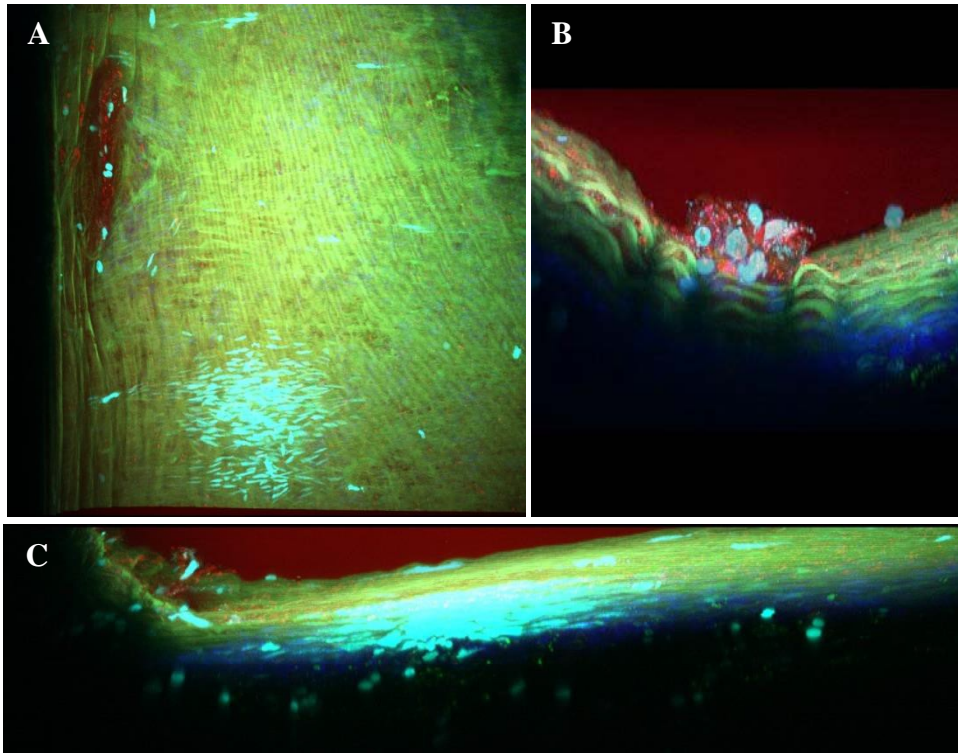


**Figure 3.5:** Multimodal nonlinear optical microscopy three-dimensional (3D) *in situ* images from the thoracic aorta with the left intercostal ostium from a 2 month old SR-BI KO/ApoER61<sup>h/h</sup> mouse fed HFHC for 5 days. Elastin (green), collagen (blue), permeabilized (damaged) Sytox blue positive cells (cyan) and lipid (red) signals are merged after post-image processing. (A) *En face* image, and (B and C) cross sections exhibiting lipid and damaged cells surrounding the left intercostal ostium with an extensive cluster of transmurally damaged smooth muscle cells (C) downstream of the ostium. (Images were obtained with a Leica 25x1.0 NA water immersion objective lens).

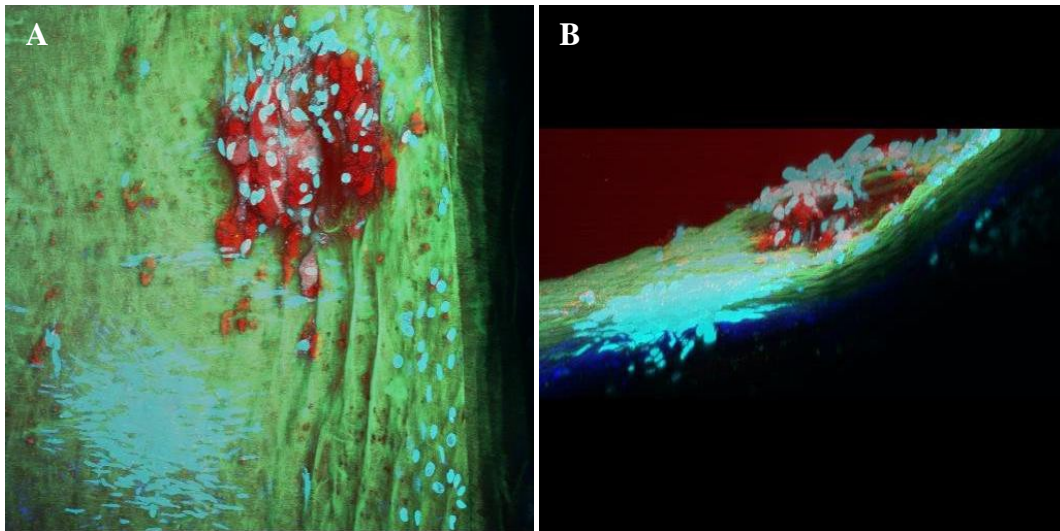


**Figure 3.6:** Multimodal nonlinear optical microscopy three-dimensional (3D) *in situ* images from the thoracic aorta with the right intercostal ostium from a 2.5 month old SR-BI KO/ApoER61<sup>h/h</sup> mouse fed HFHC for 14 days. Elastin (green), collagen (blue), permeabilized (damaged) Sytox blue positive cells (cyan) and lipid (red) signals are merged after post-image processing. (A) *En face* image with increased lipid and foam cell deposition within and surrounding the intercostal osritum with the similarly located downstream cluster of damaged smooth muscle cells and increased damaged endothelial cells surrounding the ostium. (B) Representative cross section with an extensive cluster of transmurally damaged smooth muscle cells (C) downstream of the ostium. (Images were obtained with a Leica 25x1.0 NA water immersion objective lens.

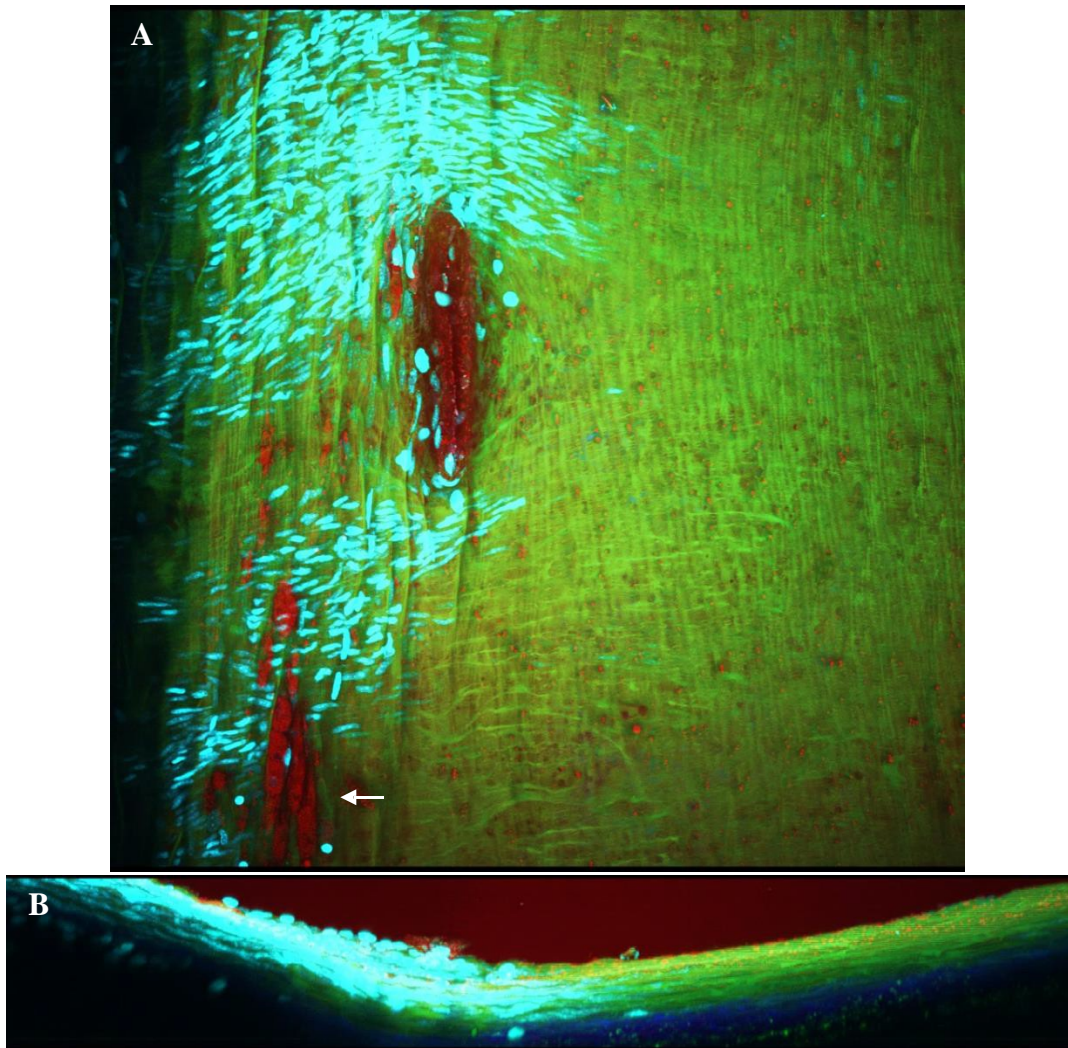


**Figure 3.7:** Multimodal nonlinear optical microscopy three-dimensional (3D) *in situ* images from the thoracic aorta with the left intercostal ostium from a 3 month old SR-BI KO/ApoER61<sup>h/h</sup> mouse fed HFHC for 21 days. Elastin (green), collagen (blue), permeabilized (damaged) Sytox blue positive cells (cyan) and lipid (red) signals are merged after post-image processing. (A) *En face* image with increased lipid and foam cell deposition on and surrounding the left intercostal osritum with the downstream cluster of damaged smooth muscle cells now colocalized with foam cell (white arrow) accumulation on the endothelium. (B) Representative cross section with an extensive cluster of transmurally damaged smooth muscle cells. (Images were obtained with a Leica

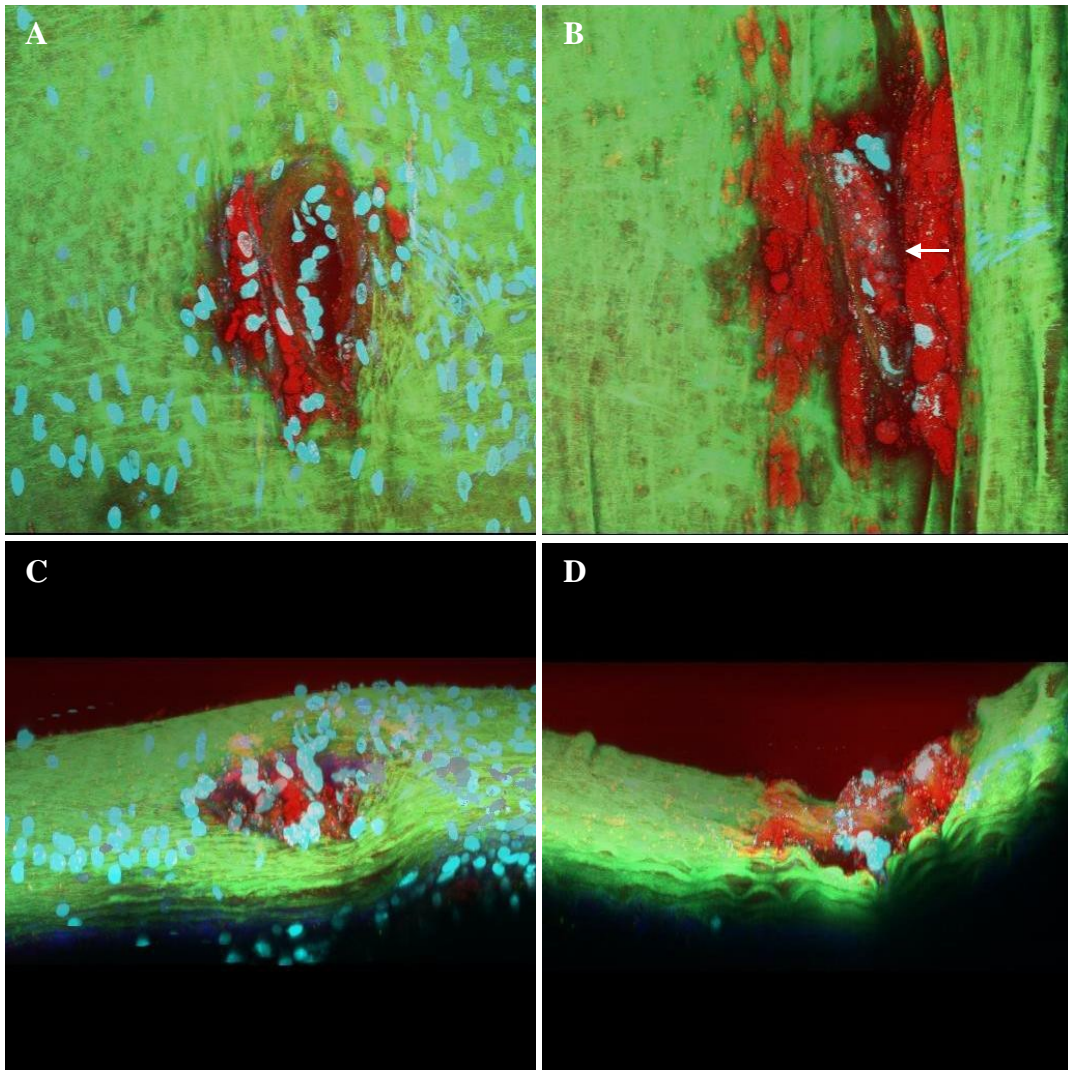


**Figure 3.8:** Additional high resolution, three-dimensional (3D) *in situ* images from the thoracic aorta with the left (A and C) and right (B and D) intercostal ostia from a 3 month old SR-BI KO/ApoER61<sup>h/h</sup> mouse fed HFHC for 21 days. Elastin (green), collagen (blue), permeabilized (damaged) Sytox blue positive cells (cyan) and lipid (red) signals are merged after post-image processing. (A) Note the lipid beginning to form a plaque that variably occludes the ostial opening (white arrow). (Images were obtained with a Leica 25x1.0 NA water immersion

## References

- Caligiuri G, Levy B, Pernow K, Thoren P, Hansson GK. Myocardial infarction mediated by endothelin receptor signaling in hypercholesterolemic mice. *Proc. Natl. Acad. Sci. U.S.A.* 1999;96:6920-6924.
- Cheng JX, Volkmer A, Book LD, Xie XS. An epi-detected coherent anti-stokes Raman scattering (E-CARS) microscope with high spectral resolution and high sensitivity. *J. Phys. Chem. B.* 2001;105(7):1277-1280.
- Cheng JX, Xie XS. Coherent anti-stokes Raman scattering microscopy: Instrumentation, theory, and applications. *J. Phys. Chem. B.* 2004;108(3):827-840.
- Cicchi R, Matthaus C, Meyer T, Latterman A, Dietzek B, Brehm BR, Popp J, Pavone FS. Non-linear imaging and characterization of atherosclerotic arterial tissue using combined two photon fluorescence, second-harmonic generation and CARS microscopy. *Proc. SPIE.* 2014; volume 8948.
- Cozen AE, Moriwaki H, Kremen M, DeYoung MB, Cichok HL, Slezicki KI, Young SG, Veniant M, Cichok DA. Macrophage-targeted overexpression of urokinase causes accelerated atherosclerosis, coronary artery occlusions, and premature death. *Circulation.* 2004;109:2129-2135.
- Evans CL, Potma EO, Puoris'haag M, Cote D, Lin CP, Xie YS. Chemical imaging of tissue in vivo with video-rate coherent anti-Stokes Raman scattering microscopy. *P. Natl. Acad. Sci. U.S.A.* 2005;102(46):16807-16812.
- Ferrara DE, Weiss D, Carnell PH, Vito RP, Vega D, Gao X, Nie S, Taylor WR. Quantitative 3D fluorescence technique for the analysis of en face preparations of arterial walls using quantum dot nanocrystals and two-photon excitation laser scanning microscopy. *Am. J. Physiol. Regul. Integr. Comp. Physiol.* 2006;290:R114-R123.
- Foteinos G, Hu Y, Xiao Q, Metzler B, Xu Q. Rapid endothelial turnover in atherosclerosis-prone areas coincides with stem cell repair in apolipoprotein e-deficient mice. *Circulation.* 2008;117:1856-1863.
- Fuster V, Ross R, Topol EJ. Atherosclerosis and Coronary Artery Disease. Volume 1. Lippincott-Raven Publishers, Philadelphia, 1996:447-449.
- Glacov S, Newman III WP, Schaffer SA: Pathobiology of the Human Atherosclerotic Plaque. Springer-Verlag, New York, 1990:7, 265.
- Hellerer T, Axang C, Brackmann C, Hillertz P, Pilon M, Enejder A. Monitoring of lipid storage in *Caenorhabditis elegans* using coherent anti-Stokes Raman scattering (CARS) microscopy. *Proc. Natl. Acad. Sci. U.S.A.* 2007;104(37):14658-14663.
- Jamkhande PG, Chandak PG, Dhawale SC, Barde SR, Tidke PS, Sakhare RS. Therapeutic approaches to drug targets in atherosclerosis. *Saudi. Pharmaceut. J.* 2014;22:179-190.

- Jongstra-Bilen J, Cybulsky MI. Regional predisposition to atherosclerosis-An interplay between local hemodynamics, endothelial cells and resident intimal dendritic cells. *Endothelial Dysfunction and Inflammation*. Springer. 2010.
- Kim SH, Lee ES, Lee JY, Lee ES, Lee BS, Park JE, Moon DW. Multiplex coherent anti-stokes Raman spectroscopy images intact atheromatous lesions and concomitantly identifies distance chemical profiles of atherosclerotic lipids. *Circ. Res.* 2010;106:1332-1341.
- Ku D. Blood flow in arteries. *Ann. Rev. Fluid Mech.* 1997;29:399-434.
- Kwon GP, Schroeder JL, Amar MJ, Balaban RS. Contribution of macromolecular structure to the retention of low-density lipoprotein at arterial branch points. *Circulation*. 2008;117:2919-2927.
- Le TT, Langhor IM, Locker MJ, Sturek M, Cheng JX. Label-free molecular imaging of atherosclerotic lesions using multimodal nonlinear optical microscopy. *J. Biomed. Opt.* 2007;12(5):054007.
- Lee JY, Kim SH, Moon DW, Lee ES. Three-color multiplex CARS for fast imaging and microspectroscopy in the entire CH<sub>n</sub> stretching vibrational region. *Opt. Express*. 2009;17(25): 22281-22295.
- Lim RS, Kratzer A, Barry NP, Miyazaki-Anzai S, Miyazaki M, Mantulin WM, Levi M, Potma EO, Tromberg BJ. Multimodal CARS microscopy determination of the impact of diet on macrophage infiltration and lipid accumulation on plaque formation in ApoE-deficient mice. *J. Lipid Res.* 2010;51:1729-1737.
- Lim RS, Suhaim JL, Miyazaki-Anzai S, Miyazaki M, Levi M, Potma EO, Tromberg BJ. Identification of cholesterol crystals in plaques of atherosclerotic mice using hyperspectral CARS imaging. *J. Lipid Res.* 2011;52:2177-2186.
- Lin SJ, Jan KM, Schuessler G, Weinbaum S, Chien S. Enhanced macromolecular permeability of aortic endothelial cells in association with mitosis. *Atherosclerosis*. 1988;73:223-232.
- Lin SJ, Jan KM, Weinbaum S, Chien S. Transendothelial transport of low density lipoprotein in association with cell mitosis in a rat aorta. *Arteriosclerosis*. 1989;9:230-236.
- Lin SJ, Jan KM, Chien S. Role of dying endothelial cells in transendothelial macromolecular transport. *Arteriosclerosis*. 1990;10:703-709.
- Lin SJ. Risk factors, endothelial cell turnover and lipid transport in atherogenesis. *Zhonghua Yi Xue Za Zhi (Taipei)*. 1996;58(5):309-316.
- Moriwaki H, Stempien-Otero A, Kremen M, Cozen AE, Dichek DA. Overexpression of urokinase by macrophages or deficiency of plasminogen activator inhibitor type 1 causes cardiac fibrosis in mice. *Circ. Res.* 2004;95:637-644.
- Mostaco-Guidolin LB, Sowa MG, Ridsdale A, Pegoraro AF, Smith MSD, Hewko MD, Kohlenberg EK, Schattka B, Shiomi M, Stalow A, Ko ACT. Differentiating atherosclerotic

- plaque burden in arterial tissues using femtosecond CARS-based multimodal nonlinear optical imaging. *Biomed. Opt. Express*. 2010;1(1):59-73.
- Neufeld EB, Yu ZX, Springer D, Yu Q, Balaban RS. The renal artery ostium flow diverter: structure and potential role in atherosclerosis. *Atherosclerosis*. 2010;211:153-158.
- Nguyen N, Haque A. Effect of hemodynamic factors on atherosclerosis in the abdominal aorta. *Atherosclerosis*. 1990;84:33-39.
- Peiffer V, Sherwin SJ, Weinberg PD. Does low and oscillatory wall shear stress correlate spatially with early atherosclerosis? A systematic review. *Cardiovasc. Res*. 2013;99:242-250.
- Raffai RL, Dong LM, Farese RV Jr, Weisgraber KH. Introduction of human apolipoprotein E4 "domain interaction" into mouse apolipoprotein E. *Proc Natl Acad Sci U.S.A.* 2001;98(20):11587-91.
- Raffai RL, Weisgraber KH. Hypomorphic apolipoprotein E mice. *J. Biol. Chem*. 2002;277(13):11064-11068.
- Robbins CS, Chudnovskiy A, Rauch PJ. Extramedullary hematopoiesis generates Ly-6c(high) monocytes that infiltrate atherosclerotic lesions. *Circulation*. 2012;125:364-374.
- Suhalim JL, Chung CY, Lilledahl MB, Lim RS, Levi M, Tromberg BJ, Potma EO. Characterization of cholesterol crystals in atherosclerotic plaques using stimulated Raman scattering and second-harmonic generation microscopy. *Bioophys. J*. 2012;102(8):1988-1995.
- Suo J, Ferrara, DE, Sorescu D, Guldberg RE, Taylor RW, Giddens DP. Hemodynamic shear stresses in mouse aortas: Implications for atherogenesis. *Arterioscler. Thromb. Vasc. Biol*. 2007;27:346-351.
- Taylor CA, Hughes TJ, Zarins CK. Finite element modeling of three-dimensional pulsatile flow in the abdominal aorta: relevance to atherosclerosis. *Ann. Biomed. Eng*. 1998;26:975-987.
- Thubrikar MJ. *Vascular mechanics and pathology*. 2007. Springer. New York
- Velican D, Velican C. Study of fibrous plaques occurring in the coronary arteries of children. *Atherosclerosis*. 1979;33:201-205.
- Wang HW, Le TT, Cheng JX. Label-free imaging of arterial cells and extracellular matrix using a multimodal CARS microscope. *Opt. Commun*. 2008;281(7):1813-1822.
- Wang HW, Langhor IM, Sturek M, Cheng JX. Imaging and quantitative analysis of atherosclerotic lesions by CARS-based multimodal nonlinear optical microscopy. *Arterioscler. Thromb. Vasc. Biol*. 2009;29:1342-1348.
- Weber C, Noels H. Atherosclerosis: current pathogenesis and therapeutic options. *Nat. Med*. 2011;17(11):1410-1422.

Wootton DM, Ku DN. Fluid mechanics of vascular systems, diseases, and thrombosis. *Ann. Rev. Biomed. Eng.* 1999;1:299-329.

Weinbaum S, Tzeghal G, Ganatos P, Pfeiffer R, Chien S. Effects of cell turnover and leaky junctions on arterial macromolecular transport. *Am. J. Physiol.* 1985;248:H945-H960.

Zadrozny LM, Neufeld EB, Lucotte BM, Connelly PS, Yu ZX, Dao L, Hsu LY, Balaban RS. Study of the development of the mouse thoracic aorta three-dimensional macromolecular structure using two-photon microscopy. *J. Histochem. Cytochem.* 2014;63(1):8-21.

Zipfel WR, Williams RM, Webb WW. Nonlinear magic: multiphoton microscopy in the biosciences. *Nat. Biotechnol.* 2003;21:1369-1377.

Zhang S, Picard M, Vasile E, Zhu Y, Raffai R, Weisgraber K, Krieger M. Diet-induced occlusive coronary atherosclerosis, myocardial infarction, cardiac dysfunction, and premature death in scavenger receptor class B Type I-deficient, hypomorphic apolipoprotein ER61 mice. *Circulation.* 2005;111:3457-3464.

## Chapter 4

### Discussions and Conclusions

Atherosclerosis is a complex, multifactorial disease of the cardiovascular system considered to be a primary cause of myocardial infarct, the main cause of death in Western society (Rodriguez et al., 2006; Yu et al., 2007). As such, it has been the topic of extensive research regarding disease initiation, progression and therapeutic intervention. There are extensive numbers of transgenic mouse models, some of which are designed towards specific experimental protocols and others that are more commonly used. The latter typically includes some type of genetic transformation in: 1) low-density lipoprotein receptor (LDLR) that mediates the endocytosis of cholesterol-rich LDL; 2) Apolipoprotein E (ApoE), a class of apolipoprotein found in the chylomicron and intermediate-density lipoproteins (IDLs) that is essential for the normal catabolism of triglyceride-rich lipoprotein constituents, and; 3) Scavenger receptors (SRs) including classes A, B, E, F and G, that mediate reverse cholesterol transport of modified lipoproteins out of the vessel wall (Moore and Freeman, 2006).

The model selected for this dissertation, SR-BI KO/ApoER61<sup>h/h</sup> diet inducible mouse model of atherosclerosis, was carefully chosen as it has been thoroughly characterized as a transgenic model that recapitulates important factors of human disease. These factors include occlusive coronary artery disease, myocardial infarction, cardiac dysfunction, and premature death (Zhang et al.; 2005; Trigatti et al., 2004, Braun et al., 2003). Moreover, this model remains clinically normal when fed NC, but exhibits accelerated clinical signs and advanced gross lesions over the course of 30 days when

switched to a HFHC diet (Zhang et al., 2005). Not only does this allow for better temporal control in experimental designs, but it is also a potentially better suited model for investigating therapeutic targets. A possible minor drawback, however, was discovered when using CARS microscopy, a highly specific nonlinear optical imaging modality versus the exogenous lipophilic probe to track lipid deposition. Although this model appears clinically normal on NC, marked hyperlipidemia intrinsically expressed in these mice, a known risk factor for atherosclerosis, did contribute to increased EC turnover, SMC and EC death resulting in early, albeit mild, vascular lesions prior to diet change.

Chapter 1 involved careful review of the literature regarding the current and past techniques used to dissect and prepare mouse vessels for NLOM. The most common *ex vivo* techniques included: 1) dissecting and mounting variably sized vessel segments onto a perfusion chamber (Megens et al., 2007a; Megans et al., 2007b); 2) fresh and/or formalin-fixed tissue dissected, cut and mounted between a slide and a glass coverslip (Kwon et al., 2008; Lee et al., 2009; Kim et al., 2010; Lim et al., 2010; Lim et al 2011; Suhlim et al., 2012), and; 3) agar gel-infused vascular casts segmented into thinly sliced molds and mounted onto a glass slide (van Zandvoort et al., 2004; Megens et al., 2007a; Megens et al., 2008; Le et al., 2010). *In vivo* techniques have included applying mouse carotid arteries to extenral handmade apparatuses for stabilization (Yu et al., 2007). Upon completion of this review, some of these techniques were reproduced in the lab, with the addition to novel techniques to develop a preparation of the mouse TA for *in-situ* imaging. We wanted to minimize both dissection and mounting artifacts thereby decreasing potential distortions while closely exhibiting several key physiological properties including longitudinal stretch.

Once developed, this novel *in situ* preparation was applied to the selected transgenic mouse model to first complete a longitudinal analysis of the development of the mouse TA 3D macromolecular structure. SR-BI KO/ApoER61<sup>h/h</sup> mice aged 1 -60 do fed NC were imaged using NLOM. To track lipid deposition, NR was administered immediately after euthanasia via left ventricular perfusion. To confirm to sensitivity and specificity of this preparation for *in situ* imaging, EM, histopathology and IHC were completed in parallel. In doing this, the intrinsic optical properties of the macromolecules in the 3D structure of the VTA were described. From this study, it was determined that the undulating lamellar elastin layers compressed consistent with the increases in mean aortic pressure with age. Three-dimensional reconstructions also showed that lipid droplets were found individualized are within small clusters and limited mainly to the endothelial surface or directly beneath the IEL within the first layer of SMCs in the tunica media.

Chapter 3 expanded upon both the initial findings from this longitudinal study and the *in situ* TA preparation. A cohort of 2-3 month old SR-BI KO/ApoER61<sup>h/h</sup> mice were fed HFHC for up to 21 days with age-matched C57BL/6T mice and SR-BI KO/ApoER61<sup>h/h</sup> mice used as day 0 controls having only been fed NC. The patent aortic preparation was longitudinally transected to reveal the ICAO for NLOM. Although we initially tried a similar preparation for the longitudinal study, through a small pilot study, it was determined that transecting the thoracic aorta was not consistently successful in capturing the ICAO in neonatal mice. The addition of CARS into the imaging platform allowed for greater sensitivity in imaging lipid thereby eliminating the need to use the exogenous lipophilic probe NR.

Administration of Sytox Blue nucleic acid stain intravascularly prior to euthanasia elucidated novel findings regarding SMC and EC death. Three-dimensional reconstructions of z-stacks taken from a rather large field of view showed transmural deposition of permeabilized, dying SMCs. This consistent pattern of compromised SMCs found downstream and/or in between pairs of ICAO was associated with several, but not all ICAO in all SR-BI KO/ApoER61<sup>h/h</sup> mice control and experimental mice. Interestingly, lipid droplet and foam cell deposition was absent within these patches until mice were fed HFHC for 21 days. Permeabilized ECs were consistently identified within the intercostal ostial ridges colocalized with lipid droplets in all SR-BI KO/ApoER61<sup>h/h</sup> control and experimental mice.

In C57BL/6T control mice fed NC, minimal permeabilized ECs or SMCs were appreciated on the luminal surface or within the tunicas media and adventitia. However, moderate numbers of Sytox Blue positive endothelial cells were identified within the ostial ridges that were nearly completely absent of any appreciable lipid. Very few, mainly individualized lipid droplets were appreciated on the luminal surface. The distribution of Sytox Blue positively stained cells in all mice used in this study is also consistently found within regions of low WSS where it has been previously shown that there are increased levels leukocyte inflammatory mediators VCAM-1 and ICAM-1 (Suo et al., 2007). Taken together, these data are suggestive that these regions of high EC and SMC turnover and death, in the absence of lipid deposition and inflammation may perhaps be precursory to the fatty streak. This experiment provided a modification to a novel, *in situ* mouse TA preparation coupled with multimodal nonlinear optical microscopy that will lend future insights into: 1) gene expression within these patches of permeabilized ECs and SMCs; 2)

potential discovery of biomarkers preceding the earliest of atherosclerotic lesions, and; 3) therapeutic intervention prior to lesion initiation.

In conclusion, the experiments presented here have not only identified novel ways to evaluate the 3D macromolecular microstructure of the vascular bed in healthy and diseased mice, they've provided insight into potential regions of atherosclerotic lesion initiation that have not been previously defined with the methods described herein. These regions should be the focus of future investigations to study the role of the transmurally dying SMCs and intercostal ostial ECs in the absence of lipid deposition where low wall shear stress and oscillatory flow are exhibited. They may perhaps be the focus in determining new biomarkers of early disease for the production of novel therapeutics.

## References

- Braun A, Zhang S, Miettinen HE, Ebrahim S, Hom TM, Vasile E, Post MJ, Yoerger DM, Picard MH, Krieger JL, Andrews NC, Simons M, Krieger M. Probucol prevents early coronary heart disease and death in the high-density lipoprotein receptor SR-BI/apolipoprotein E double knockout mouse. *Proc. Natl. Acad. Sci. U.S.A.* 2003;100(12):7283-7288.
- Kim SH, Lee ES, Lee JY, Lee ES, Lee BS, Park JE, Moon DW. Multiplex coherent anti-stokes Raman spectroscopy images intact atheromatous lesions and concomitantly identifies distinct chemical profiles of atherosclerotic lipids. *Circ. Res.* 2010;106:1332-1341.
- Kwon GP, Schroeder JL, Amar MJ, Balaban RS. Contribution of macromolecular structure to the retention of low-density lipoprotein at arterial branch points. *Circulation.* 2008;117:2919-2927.
- Le TT, Duren HM, Slipchenko MN, Hu CD, Cheng JX. Label-free quantitative analysis of lipid metabolism in living *Caenorhabditis elegans*. *J. Lipid Res.* 2010;51:672-677.
- Lee JY, Kim SH, Moon DW, Lee ES. Three-color multiplex CARS for fast imaging and microspectroscopy in the entire CH<sub>n</sub> stretching vibrational region. *Opt. Express.* 2009;17(25): 22281-22295.
- Lim RS, Kratzer A, Barry NP, Miyazaki-Anzai S, Miyazaki M, Mantulin WM, Levi M, Potma EO, Tromberg BJ. Multimodal CARS microscopy determination of the impact of diet on macrophage infiltration and lipid accumulation on plaque formation in ApoE-deficient mice. *J. Lipid Res.* 2010;51:1729-1737.
- Lim RS, Suhaimi JL, Miyazaki-Anzai S, Miyazaki M, Levi M, Potma EO, Tromberg BJ. Identification of cholesterol crystals in plaques of atherosclerotic mice using hyperspectral CARS imaging. *J. Lipid Res.* 2011;52:2177-2186.
- Megens RTA, oude Egbrink MGA, Cleutjens JPM, Kuijpers MJE, Schiffers PHM, Merkx M, Slaaf DW, van Zandvoort MAMJ. Imaging collagen in intact viable healthy and atherosclerotic arteries using fluorescently labeled CNA35 and two-photon laser scanning microscopy. *Mol. Imaging.* 2007a;6:247-260.
- Megens RTA, Reitsma S, Schiffers PHM, Hilgers RHP, DeMey JGR, Slaaf DW, oude Egbrink MGA, van Zandvoort MAMJ. Two-photon microscopy of vital murine elastic and muscular arteries. *J. Vasc. Res.* 2007b;44:87-98
- Megens RTA, oude Egbrink MGA, Merkx M, Slaaf DW, van Zandvoort MAMJ. Two-photon microscopy on vital carotid arteries: imaging the relationship between collagen and inflammatory cells in atherosclerotic plaques. *J. Biomed. Opt.* 2008;13:044022-1 – 044022-10.
- Moore KJ, Freeman MW. Scavenger receptors in atherosclerosis: beyond lipid uptake. *Arterioscler. Thromb. Vasc. Biol.* 2006;26:1702-1711.

- Rodriguez GA, Serruys PW, Garcia HM. Coronary artery remodeling is related to plaque composition. *Heart*. 2006;92:388-391.
- Suhaim JL, Chung CY, Lilledahl MB, Lim RS, Levi M, Tromberg BJ, Potma EO. Characterization of cholesterol crystals in atherosclerotic plaques using stimulated Raman scattering and second-harmonic generation microscopy. *Bioophys. J.* 2012;102(8):1988-1995.
- Suo J, Ferrara, DE, Sorescu D, Guldberg RE, Taylor RW, Giddens DP. Hemodynamic shear stresses in mouse aortas: Implications for atherogenesis. *Arterioscler. Thromb. Vasc. Biol.* 2007;27:346-351.
- Trigatti B, Covey S, Rizvi A. Scavenger receptor class B type I in high-density lipoprotein metabolism, atherosclerosis and heart disease: lessons from gene-targeted mice. *Biochem. Soc. T.* 2004;32:116-120.
- van Zandvoort M, Engels W, Douma K, Beckers L, oude Egbrink M, Daemon M, Slaff DW. Two-photon microscopy for imaging of the (atherosclerotic) vascular wall: A proof of concept study. *J. Vasc. Res.* 2004;41:54-63.
- Yu W, Braz JC, Dutton AM, Prusakov P, Rekhter M. In vivo imaging of atherosclerotic plaques in apolipoprotein E deficient mice using nonlinear microscopy. *J. Biomed. Opt.* 2007;12(5):054008.
- Zhang S, Picard M, Vasile E, Zhu Y, Raffai R, Weisgraber K, Krieger M. Diet-induced occlusive coronary atherosclerosis, myocardial infarction, cardiac dysfunction, and premature death in scavenger receptor class B Type I-deficient, hypomorphic apolipoprotein ER61 mice. *Circulation*. 2005;111:3457-3464.